REPORT DOCUMENTATION PAGE

Form Approved
OMB No. 0704-0188

1. AGENCY USE ONLY (Leave blank)	2. REPORT DATE	3. REPORT TYPE AND DATES COVERED
	September 1996	FINAL 1 DEC.93 – 30 NOV. 95

4. TITLE AND SUBTITLE

A HIGH THRUST DENSITY, C_{60} CLUSTER, ION THRUSTER

5. FUNDING NUMBERS

(C) F49620-94-C-0006

6. AUTHOR(S)

V. HRUBY, J. MONHEISER and J. KOLENCIK

7. PERFORMING ORGANIZATION NAME(S) AND ADDRESS(ES)

BUSEK CO. INC.
11 TECH CIRCLE
NATICK, MA   01760

8. PERFORMING ORGANIZATION REPORT NUMBER

036-3

9. SPONSORING/MONITORING AGENCY NAME(S) AND ADDRESS(ES)

AIR FORCE OFFICE OF SCIENTIFIC RESEARCH
110 DUNCAN AVENUE, SUITE B115
BOLLING AFB, D.C.   20332-0001

N/A

10. SPONSORING/MONITORING AGENCY REPORT NUMBER

F49620 - 94-C-0006

11. SUPPLEMENTARY NOTES

12a. DISTRIBUTION/AVAILABILITY STATEMENT

Approved for public release,
distribution unlimited

12b. DISTRIBUTION CODE

19961016 084

13. ABSTRACT (Maximum 200 words)

This report summarizes the results of a two year SBIR Phase II effort to develop a fullerene ion thruster system consisting of an integrated fullerene propellant delivery system and the thruster. The system has been designed, constructed and tested. Investigation of fullerene properties and behavior as related to in-space storage and vaporization was carried out concurrently in a separate apparatus constructed for that purpose.

The dc discharge method of fullerene vapor ionization was selected over electrodeless (e.g., RF) ionization alternatives. Argon fed hollow cathodes were used as the source of discharge electrons and for beam neutralization.

A 1000 eV ion beam currents of the order of 30 mA were measured which resulted in calculated thrust in excess of 3 mN and a disappointing propellant utilization in the range of 10 to 20%. While using Ar fed hollow cathode the carbon residue inside the discharge chamber was very small relative to that observed when using heated tungsten filament cathode. This is credited to absence of thermal fragmentation caused by the filament and to possible beneficial effects of argon.

Future work on the discharge chamber, the grid system and the effects of noble gas on fullerene plasma is likely to yield a viable electric propulsion device which could also be used for fast growth rate carbon film deposition.

14. SUBJECT TERMS

FULLERENES, ION THRUSTER, ELECTROSTATIC PROPULSION

15. NUMBER OF PAGES

110

16. PRICE CODE

17. SECURITY CLASSIFICATION OF REPORT	18. SECURITY CLASSIFICATION OF THIS PAGE	19. SECURITY CLASSIFICATION OF ABSTRACT	20. LIMITATION OF ABSTRACT
UNCLASSIFIED	UNCLASSIFIED	UNCLASSIFIED	UL

DISCLAIMER NOTICE
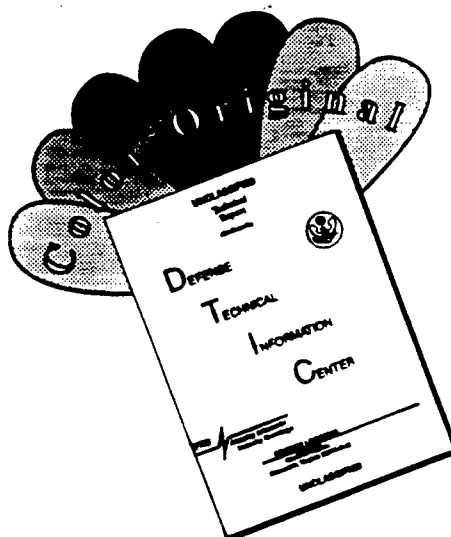
THIS DOCUMENT IS BEST QUALITY AVAILABLE. THE COPY FURNISHED TO DTIC CONTAINED A SIGNIFICANT NUMBER OF COLOR PAGES WHICH DO NOT REPRODUCE LEGIBLY ON BLACK AND WHITE MICROFICHE.

A HIGH THRUST DENSITY, C_{60} CLUSTER, ION THRUSTER

Prepared by

V. Hruby, J. Monheiser and J. Kolencik

BUSEK CO. INC.
11 Tech Circle
Natick, MA 01760-1023

September 1996

distribut... unlimited

FINAL TECHNICAL REPORT

Period of Performance: 1 December 1993 - 30 November 1995

Contract F49620-94-C-0006

Prepared for

Air Force Office of Scientific Research
Bolling AFB, DC 20332-0001

TABLE OF CONTENTS

BUSEK

TABLE OF CONTENTS (Con't)

BUSEK

LIST OF ILLUSTRATIONS

BUSEK

LIST OF ILLUSTRATIONS (Con't)

BUSEK

Table		Page

BUSEK

ACKNOWLEDGMENT

BUSEK

1.0 INTRODUCTION

This section is divided into two parts. In the first part we discuss the motivation for this effort and in the second part we briefly discuss fullerene ion thruster work being carried out by others.

1.1 Motivation for the Present Work

The motivation for the present work stems from the excellent prospects of the fullerene ion thruster (FIT) to become the preferred electrostatic propulsion device for a range of missions starting from low thrust attitude control, to orbit transfer and multimegawatt interplanetary flights. Simple analysis indicate that a fullerene C_{60} ion thruster could provide up to a factor of 30 increase in thrust density over the current atomic fuels of choice (Xe, Hg) as well as a simultaneous reduction of relative losses by a factor of 5.5. This thrust density increase would result in a reduction in required accelerator grid areas to a size that is economical and practical to construct even for megawatt sized thrusters.

Space-charge limitations of the ion acceleration process limit the thrust density of Xe or Hg fueled thrusters to the extent that these engines are presently practical for limited number of missions. Other fuels have been examined to increase thrust density to levels that would lead to an attractive thruster with wider applicability. Atomic clusters were found to have the most promise as a result of their large effective molecular weight. Heretofore, problems with cluster stability during acceleration have so far prevented their use in ion thrusters. However, a recently discovered form of carbon, termed fullerenes,[1] possess a wide variety of unusual properties. Their high molecular weight, extreme stability under impact plus low first ionization potential make it an excellent candidate for high thrust density ion thruster fuel. Below we briefly substantiate this assertion.

As mentioned above, an intergrid space charge limits the thrust density of ion thrusters. The Child-Langmuir space charge limited current equation is

$$j = \frac{4\sqrt{2}}{9}\varepsilon_o \left(\frac{e}{m_i}\right)^{1/2} \frac{V_a^{3/2}}{d^2} \qquad [1.1]$$

where V_a is the total accelerating potential, d is the grid spacing and m_i is the ion mass. As this equation shows, increasing m_i, at fixed V_a tends to reduce the current density. However, a more likely scenario is that the specific impulse (and hence the ion exit velocity (c), would be kept constant, since an optimum value of c exists for each given mission and power supply. In that case, the accelerating voltage would be proportional to m_i, since

$$V_a \approx \frac{m_i c^2}{2e}$$

and the current density (Eq. [1.1]) is seen to increase as m_i.

The grids act as a very selective filter, extracting ions in preference to neutrals from the partially ionized chamber gas. If we assume that only the ions are extracted, the mass flow rate per unit grid area is

BUSEK

$$\frac{m}{A} = j\frac{m_i}{e}$$

Multiplying times c gives the thrust density which combined with Eq. [1.1] yields

$$\frac{F}{A} = \frac{2}{9}\varepsilon_o\left(\frac{m_i}{e}\right)^2\frac{c^4}{d^2} \qquad [1.2]$$

This shows the principal advantages of using high mass ions: the thrust density can be made higher as m_i^2, thus mitigating one the principal disadvantages of ion thrusters.

Extension of the analysis carried out above lead to an expression relating thruster beam power per unit grid area to the thrust density of Eq. [1.2]. This expression is

$$\frac{P_i}{A} = \frac{1}{2}\left(\frac{F}{A}\right)c \qquad [1.3]$$

As an example, consider an interplanetary mission with a thruster beam power of 10 MW, $c \approx 50,000$ m/sec and grid spacing $d \approx 1$ mm. Equations [1.2] and [1.3] then say that for Xe, the grid area is 18.3 m^2 and for C_{60} it reduces to 0.61 m^2. The later is practical, the former is not. In fact, it may be advisable to reduce the thrust density for other reasons and still maintain practical size grid. Thus, C_{60} opens new doors for electrostatic propulsion.

Another advantage is the relative reduction of power losses. These losses arise from a variety of sources (ionization work, need to re-ionize ions that strike chamber walls before extraction, electron kinetic energy rendered to the anode, etc.). In general, the energy loss per ion tends to be independent of propellant used, since it is closely associated with the ionization energy, which varies relatively little (although it is to be noted that C_{60} has lower ionization energy than Hg and Xe). The losses per ion are usually quoted as a voltage ΔV_L, such that $\Delta V_L \times I_{beam} =$ Energy Loss Rate. The useful work ion is $1/2\, m_i c^2$, and so the efficiency is

$$\eta = \frac{\frac{1}{2}m_i c^2}{\frac{1}{2}m_i c^2 + e\Delta V_L} = \frac{1}{1 + \frac{2e\Delta V_L}{m_i c^2}} \qquad [1.4]$$

It is clear that higher m_i leads directly to higher efficiency. For example, using $\Delta V_L = 200$ V (a conservative estimate) Fig. 1.1 shows the thruster efficiencies with Xe, Hg and C_{60} used as propellants. The advantage of fullerene is most striking in the specific impulse range between 1000 and 2000 seconds, where many space missions optimize, and where the conventional propellants give unacceptably low efficiencies (as well as low thrust densities, (see Eq. [1.2]). The dramatic thrust density and efficiency improvements with C_{60} fuel are shown in Table 1.1.
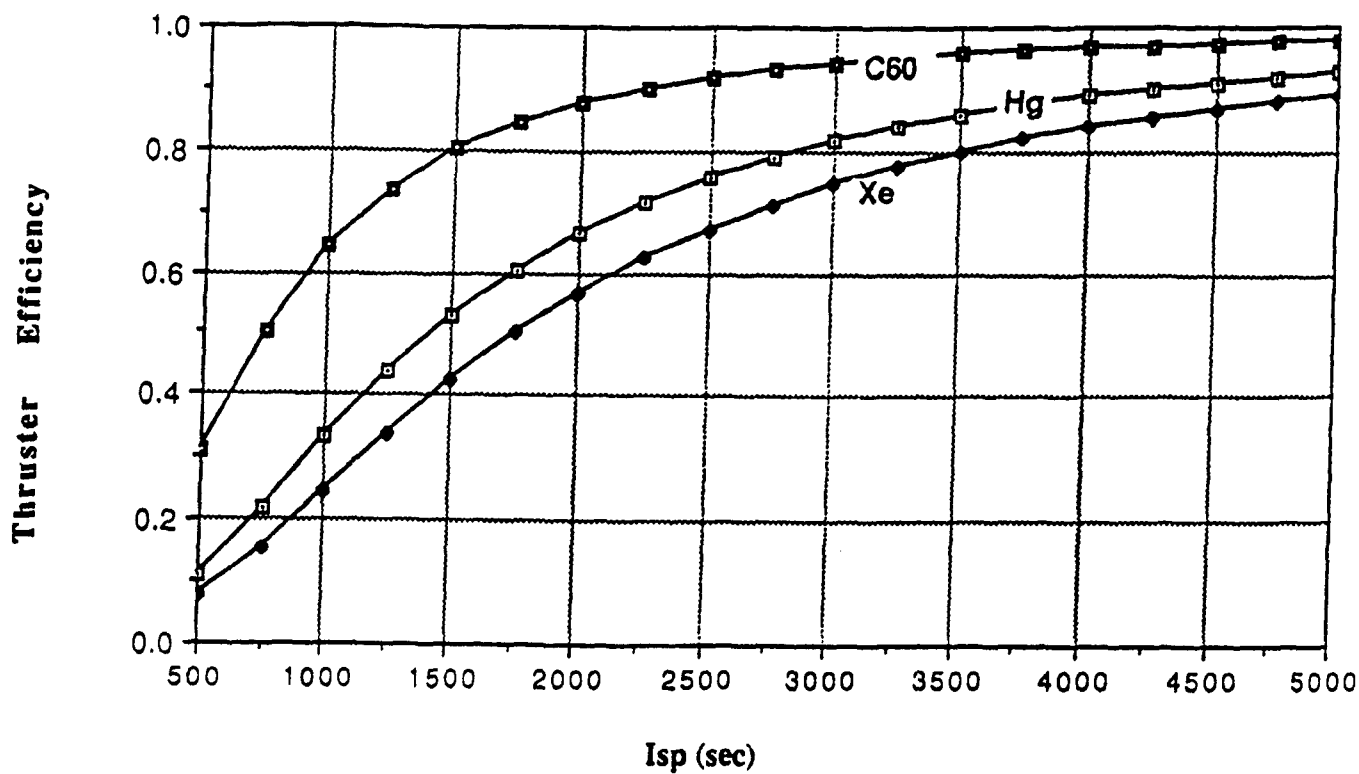
Fig. 1.1 The C$_{60}$ Greatly Improves Ion Thruster Efficiency in the Range of I$_{sp}$ Where Most Missions Optimize (1500 to 2500). At I$_{sp}$ = 1500 the C$_{60}$ thruster has double the efficiency of Xe fueled thruster.

TABLE 1.1

Propellant Comparison for c = 50,000 m/sec, d = 1 mm, ΔV_L = 200 volts
$$VaXe/VaC_{60} = miXe/miC_{60}$$

Propellant	m_i (g/mol)	V (Volt)	F/A (N/m^2)	P_{jet}/A (W/m^2)	η
Xe	131	1700	21.8	5.46×10^5	0.89
C_{60}	720	9340	659	1.65×10^7	0.97

Although intergrid voltage approaching 10 kV with 1 mm spacing may not be achievable (in test chambers at p ~ 10^{-5} torr the peak practical voltage may be 2 kV and go up as pressure goes down), Table 1.1 does illustrate the fullerene ion thruster potential.

1.2 Fullerene Ion Thruster Work by Others

The potential advantages of the fullerene ion thruster were recognized by several groups, some of which carried their work to experimental demonstration. The two most active groups are at the Jet Propulsion Laboratory[2-7] and Tokyo Metropolitan Institute of Technology.[8-10]

Numerical modeling was performed at MIT[11] and unpublished exploratory work was performed at Hughes. Our own initial work is described in Refs. 12 and 13.

At JPL, Leifer, et al[2,4,5] focused their effort on investigation of the fundamental fullerene properties with fullerene thermal stability being the principal issue. The salient results were that fullerenes decompose above 800°C especially in contact with hot metal surfaces. The use of hot filament cathodes in the discharge chamber was therefore judged undesirable and the group constructed laboratory thrusters with RF discharge. The experimental work was primarily carried out by Anderson, et al[3,6,7] who found that the RF discharge established on Xe quenches when appreciable fullerene number density was introduced into the discharge chamber. This was explained by known electronegativity of the fullerene molecule which was reported to scavenge low energy electrons and creating negative fullerene ions. It was ascertained that although more power could be delivered to the plasma, the oscillatory electron motion in the RF discharge necessarily creates time dependent electron energy distribution with the low energy electrons getting captured by the C_{60} and therefore applying higher RF power was not productive.

Given Leifer's and Anderson's, et al[2-6] reasoning for selection of RF discharge over filament cathode, (i.e., avoid hot surfaces inside discharge chamber) the next step would be to use Electron Cyclotron Resonance (ECR) discharge. This however, was not implemented and instead, Anderson, et al[7] used filament cathode. Using this system he found that up to 2/3 of the fullerenes fragmented and remained as a residue inside the discharge chamber. The unacceptably high degree of fragmentation was attributed to electron impact ionization process which is in conflict with published results (Refs. 21-23 from Ref. 7) which indicate that electron impact fragmentation occurs at energies over 45 eV. Since the discharge voltage was about 40 to 50 volts, the fragmentation was explained by long residence time of the ions in the discharge chamber (~1 msec), as opposed to 1 μsec in the experiments where the 45 eV threshold was measured. Since the fullerene ions have energy dependent half life for dissociation, Anderson, et

BUSEK

al[7] concluded that unless techniques for much shorter residence time of the fullerene ions in the thruster discharge chamber are found, fullerenes will not be practical propellant.

The Japanese research[8-11] lead to substantially different conclusions. Their work also started with RF discharge[8] and evolved into dc discharge using filament cathode.[9-11] The extent to which the fullerenes fragmented and how much if any of the sublimed propellant remained as a fragmented residue in the discharge chamber is not reported. Their best results are 36 mA of beam current, extracted with 1050 volts intergrid voltage, at 12.2% propellant utilization efficiency. The beam was collected on a target plate that was negatively polarized 150 volts below the accelerator grid. The discharge chamber diameter was approximately 11.5 cm in dia. No information on grid system was given. Fragmentation of fullerenes was detected in the beam from beam spectral analysis but only at high discharge voltage (60 volts which is well above the published limit of 45 eV). Reference 11 concludes that while the grid system, discharge stability and plasma confinement require improvements, the fullerene ion thruster is viable.

BUSEK

2.0   IONIZATION METHOD & THRUSTER DESIGN OPTIONS

2.1   Background

During the Phase I program experiments were conducted with quartz discharge chamber with 2% thoriated tungsten filament cathode at its center.[15] The filament had a life time of a few minutes. This was due to the cathode poisoning caused by carbon ion bombardment which in some cases created a carbon layer as much as 0.05 mm thick. The carbon layer then became the electron emitter which, due to its poor emission characteristic, required increased temperature of the cathode filament eventually causing its rapid demise. Thus, cathode selection became a significant issue with broad implications to the design of the overall thruster system.

2.2   Discharge Selection

Fullerenes fragment to graphite when exposed to temperatures above approximately 750°C. A survey of literature has shown no elements or carbides capable of thermionic emission at or below this temperature.[16] The best hollow cathodes tested to date operate at about 1100°C. Thus, operating a filament cathode or a hollow cathode on C_{60} is an unlikely proposition. Without hollow cathode inside the discharge chamber, the conventional ionization by electron bombardment must be replaced by some electrodeless discharge such as RF or electron cyclotron resonance (ECR). However, the RF and ECR approach requires heavy, inefficient power supplies and discharge chamber walls that must be dielectric. Since some C_{60} fragmentation and carbon deposition on the discharge cavity walls is likely to occur, it could lead to a build-up of conductive layer, inhibiting the RF energy transfer and shorting the discharge. The high probability of this event and the fact that the external neutralizer is likely to require noble gas (at least for long duration missions), lead us to select the dc discharge method with conventional hollow cathodes operated on Ar for both the internal discharge and the external neutralizer. The selection process is depicted graphically in Fig. 2.1.

Even though the mass flow of Ar is 10% or less of the C_{60} flow, the use of this mixed propellant with very large differences in molecular weight may have some undesirable consequences. Among them is system complications because the spacecraft must carry dual propellant and the possibility of larger grid erosion due to the C_{60}/Ar interaction.

The increased system complexity must be considered relative to the increased power conditioning mass, and inefficiency if the dc power source is replaced with RF or ECR power source. The preferred approach is not clear. Initially NASA JPL selected the RF approach[2-5] which was a factor in our selection of the dc approach because it offers the Air Force an opportunity to compare the two.

The C_{60}/Ar interactions were considered in two ways. The first was to ask what could be done to keep the two species apart while allowing electrons from Ar cathode to ionize C_{60} vapor and the second was if we cannot keep them apart what are the consequences, primarily to the lifetime of the grids? These issues are discussed below.

2.3   Alternative DC Discharge Approaches

A conventional ion thruster dc discharge chamber has a coaxial hollow cathode at its upstream end that operates on the same gas as the main discharge. For reasons described above, this is not possible for the fullerene ion thruster (FIT). We therefore considered using an E-beam

BUSEK
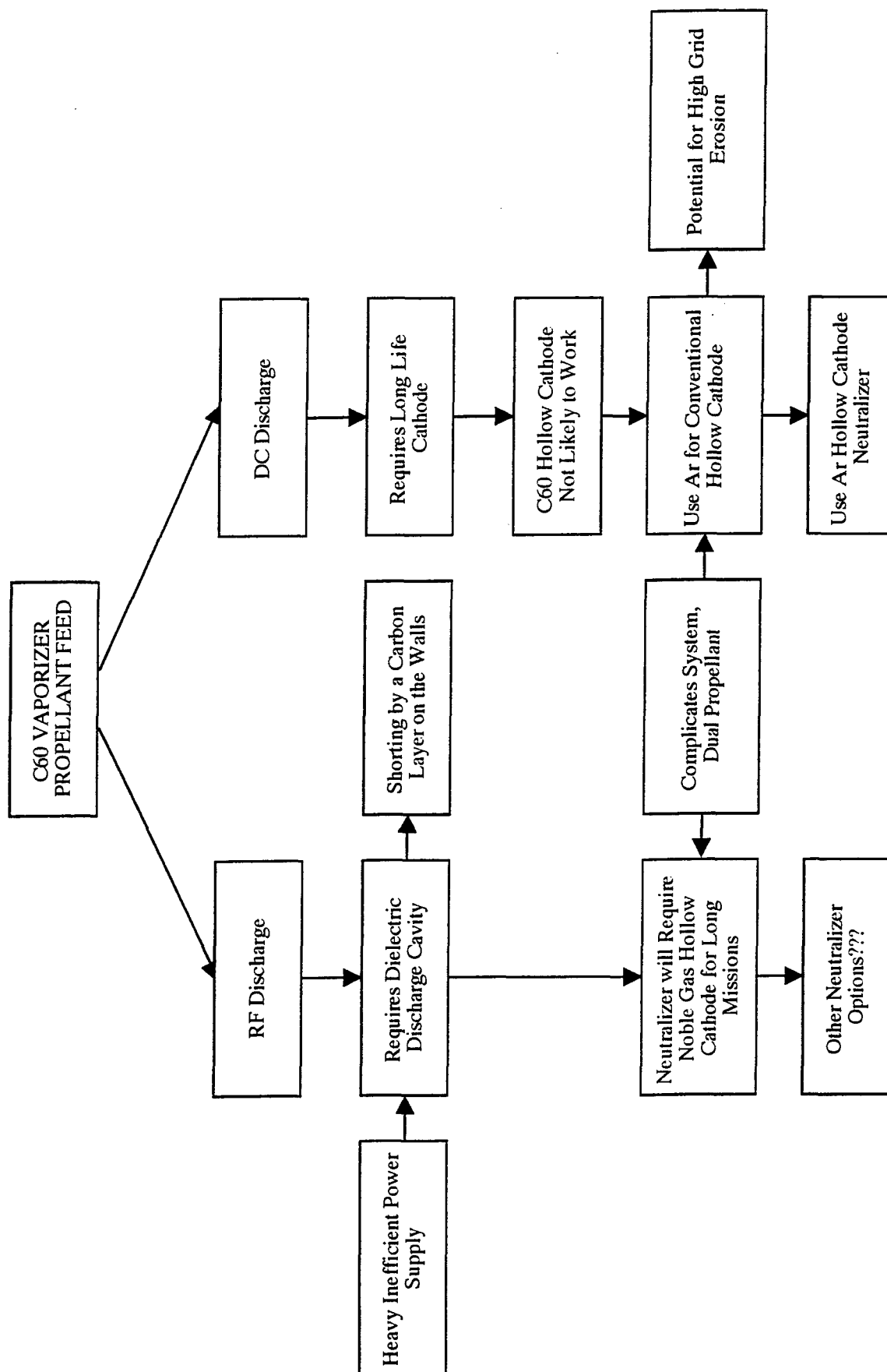
Fig. 2.1 Ionization Method Selection Tree

The boxes in the selection tree contain the following text:

- C60 VAPORIZER PROPELLANT FEED
- RF Discharge
- DC Discharge
- Heavy Inefficient Power Supply
- Requires Dielectric Discharge Cavity
- Requires Long Life Cathode
- Shorting by a Carbon Layer on the Walls
- C60 Hollow Cathode Not Likely to Work
- Complicates System, Dual Propellant
- Use Ar for Conventional Hollow Cathode
- Neutralizer will Require Noble Gas Hollow Cathode for Long Missions
- Potential for High Grid Erosion
- Use Ar Hollow Cathode Neutralizer
- Other Neutralizer Options???

and also placing the hollow cathode in or near the discharge chamber in such a way that would allow the electrons to enter the C_{60} vapor but would minimize its mixing with argon.

Ionization of the fullerene vapor with E-beam is possible but a disadvantage is the significant complexity of the E-beam source, high electron energy and low current density. The current density can be increased to a significant level only by increasing the electron energy near or beyond that acceptable for fullerenes which is about 50 eV. Above this threshold the fullerenes are likely to fragment upon C_{60}/electron collision. Because of this difficulty this approach was at least temporarily abandoned.

A configuration that uses hollow cathode as the source of electrons for C_{60} ionization while limiting the mixing of the hollow cathode gas with the fullerenes is shown in Fig. 2.2. It is basically an Ar (or Xe) ion thruster inside a C_{60} ion thruster that share a common hollow cathode. This approach minimizes C_{60}/Ar mixing within the discharge chamber and offers interesting operational possibilities. The noble gas would have its own distinct ion optics and would deliver high I_{sp} and low thrust while C_{60} at the same grid voltage would deliver higher thrust at lower I_{sp}.

This may be most attractive for large ion thrusters with power levels exceeding 10 kW and grid diameter exceeding 50 cm where the grid structure shown in Fig. 2.2 is necessary for mechanical and thermal reasons irrespective of the nature of the propellant.

A simpler version of the same concept is to eliminate the Ar discharge (anode and power supply) and the Ar grids and simply exhaust the Ar used by the hollow cathode.

2.3.1 Negative Ion Beam

Given the electronegative nature of C_{60}, it is natural to consider construction of fullerene ion thruster where the C_{60} ions are negative instead of the conventional positive ions. Negative C_{60} ions can be created by flowing the fullerene vapor over electronically emissive surface which amounts to contact ionization. The C_{60} acquires low energy electron (energy approximately equal to the emitter work function) and becomes a negative ion. The negative ions can then be accelerated just like the positive ions except for reversed grid polarity.

The issue then becomes how to neutralize the negative beam which must be accomplished by equal beam current of positive charges. One possibility would be to simply use two closely spaced thrusters, one operating on negative C_{60} ions and the other a conventional noble gas positive ions. Another more integrated option would be the coaxial dual thruster schematically shown in Fig. 2.2. Electrons from the central hollow cathode would impact ionize only the noble gas and openings between the inner chamber and outer (C_{60}) chamber would be sealed. The C_{60} would be charged negatively by contact ionization as described above.

The fact that the two grid systems require opposite polarity presents an engineering challenge. The good feature is absence of external cathode neutralizer which is not needed for this dual beam thruster.

2.4 Grid Erosion by Mixed Ar/C_{60} Propellant

The concept shown in Fig. 2.2 was evolved because of our concerns over unacceptable grid erosion caused by the dual/mixed propellant. However, before embarking down this path, an assessment of the magnitude or relative grid erosion increase was needed. Therefore, ERC, Inc. was subcontracted to utilize their Plasma Particle Simulation Code[17] to predict what is likely to happen to the grids due to direct impingement by either C_{60} or Ar and due to charge exchange

BUSEK
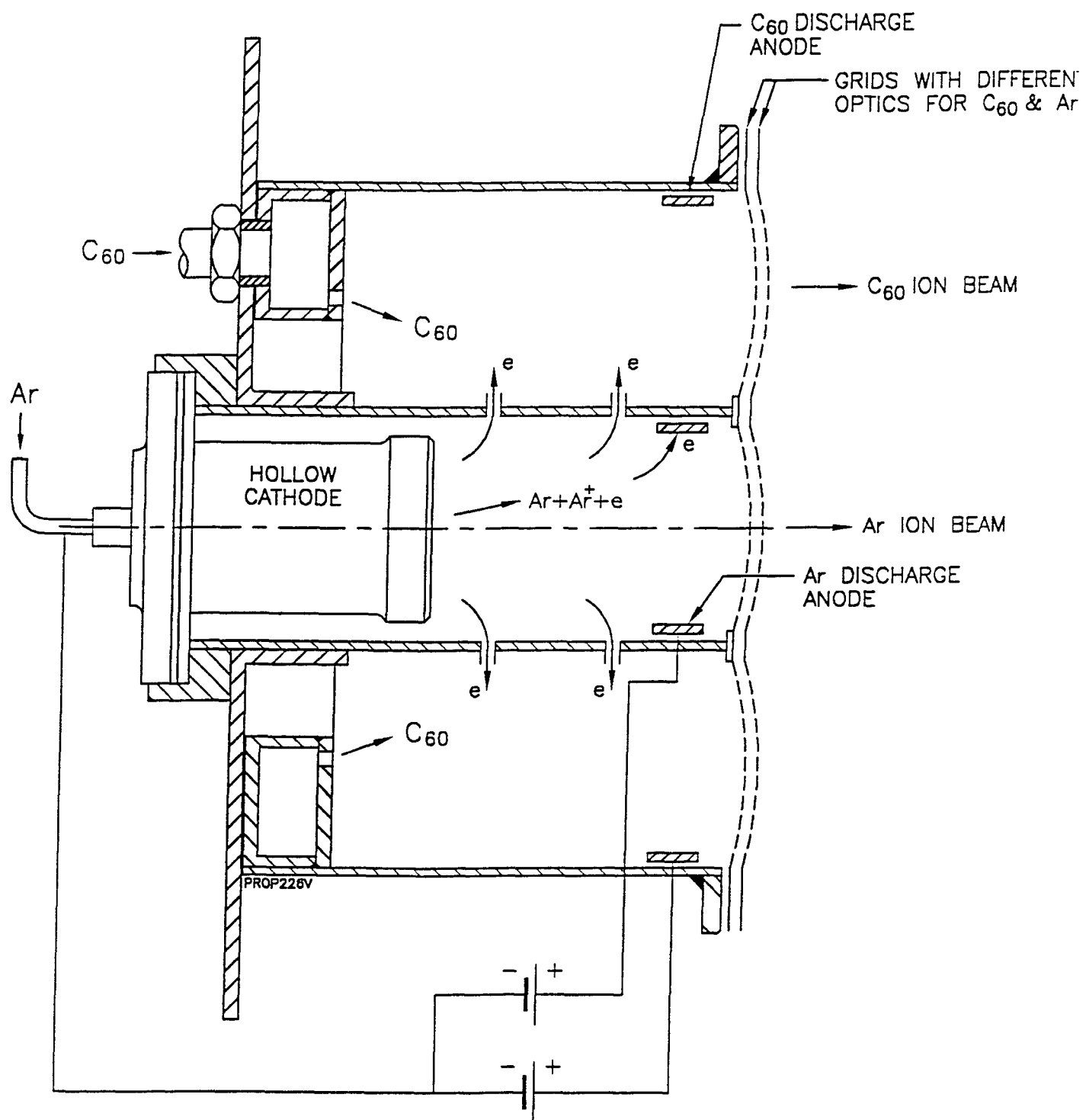
Fig. 2.2 Common Hollow Cathode with C_{60} and Ar Beams

collisions with corresponding impingement on the external side of the acceleration grid. The charge exchange collisions that were considered are:

$$C_{60}^+ \text{ (fast)} + Ar \text{ (slow)} \rightarrow C_{60} \text{ (fast)} + Ar^+ \text{ (slow)}, \qquad [2.1]$$

$$Ar^+ \text{ (fast)} + C_{60} \text{ (slow)} \rightarrow Ar \text{ (fast)} + C_{60}^+ \text{ (slow)}, \qquad [2.2]$$

$$C_{60}^+ \text{ (fast)} + C_{60} \text{ (slow)} \rightarrow C_{60} \text{ (fast)} + C_{60}^+ \text{ (slow)}, \qquad [2.3]$$

$$Ar^+ \text{ (fast)} + Ar \text{ (slow)} \rightarrow Ar \text{ (fast)} + Ar^+ \text{ (slow)}. \qquad [2.4]$$
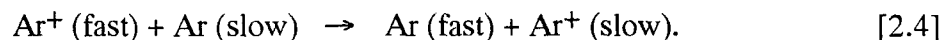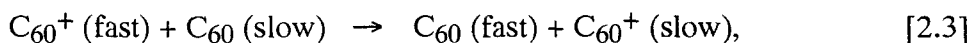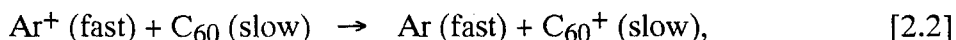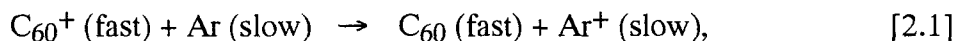
However, due to the lack of collisional cross-section data, only the fourth charge exchange reaction was actually evaluated and resulted in negligible molybdenum grid erosions (8.5 x 10^{-8} kg/hr at 2000 volts intergrid voltage). A low direct impingement of C_{60} was also predicted. The calculations were performed for three different ion optics with three different voltages with the Ar mass flow being 10% of the C_{60} mass flow. The complete ERC report is reproduced in Appendix A.

2.5 Penning Ionization Reaction

Because no data exists, it was estimated that the Penning charge transfer reaction of excited Ar and Ar^+ ions at thermal energies of interest has a rate constant greater than 10^{-9} cm^3/molecule sec.[18] This is a very fast rate which means that at 2 microns discharge chamber pressure, which is about 6 x 10^{13} C_{60}/cm^3 the Ar^+ reacts to make C_{60}^+ in about 17 x 10^{-6} sec and the mean free path is less than 1 cm. The rate constant of the Penning ionization reaction which is $Ar^* + C_{60} \rightarrow Ar + C_{60}^+$ has not been measured but is expected to be greater than 10^{-10} cm^3/mol sec in which case the mean free path at 2 microns could be 10 cm. Thus the charged Ar ions should all convert to C_{60}^+ and some of the excited Ar should produce C60$^+$. However, a fraction of the Ar^+ may be lost on the walls of the chamber.

In either case, the concentration of Ar^+ species near the grid should be small and therefore grid erosion due to direct impingement or charge-exchange collisions should be small. Most importantly, the ionized and accelerated species should be fullerenes only.

2.6 Section Summary

A dc discharge with hollow cathode operated on Ar was selected for fullerene vapor ionization. This selection was based on (1) assessment of electrodeless discharge techniques relative to the dc discharge; (2) survey of available high emissivity elements and carbides; (3) estimate of Ar^+ concentration near the grids; and (4) estimate of dual propellant effects on grid erosion. Although this approach complicates the spacecraft propellant system due to the dual fuel storage, it simplifies the neutralizer design and operation and appears to have greater chance of success than the RF discharge. An alternative dual beam concept was presented where the C_{60} beam uses negative ions and the noble gas beam uses conventional positive ions for overall beam neutrality. Both beams of course produce thrust and external cathode neutralizer is not needed.

BUSEK

3.0 FULLERENE STUDIES

The fullerene vapor pressure data that were obtained during the Phase I investigation[15] fell substantially above the anticipated values (Fig. 3.1). Because vapor pressure (p) and temperature (T) determines the propellant mass ($\dot{m}$) flow which is a crucial variable in evaluating space thrusters, the Phase I experiments were repeated.

The balanced beam apparatus constructed in Phase I was used initially to measure the mass flow real time and which was then related to the vaporize pressure and temperature through the equations below.

$$p = p_r e^{-\frac{\Delta H_s}{RT}} \qquad [3.1]$$

$$\dot{m} = pA \sqrt{\frac{M_w}{2\pi RT}} \qquad [3.2]$$

where A is the orifice flow area, M_w is molecular weight, R is the universal gas constant, ΔH_s is fullerene sublimation energy and P_r is a reference pressure. ΔH_s and P_r are given in Table 3.1 below.

Table 3.1 C_{60} and C_{70} Vapor Pressure Related Constants

	C_{60}	C_{70}
Pr (mTorr)	4×10^{10}	1.4×10^{12}
ΔH_s (cal/mole)	38,000	45,000
M_w (g/mole)	720	840

Prior to the mass flow measurements, all fullerene samples are first "dried" which entails heating the batch -- typically few grams at a time to 300°C in vacuum (p ~ 10^{-4} torr) for about 24 hours. During drying the sample is held in an open quartz container inside a vacuum furnace.

The vapor pressure data obtained with the balanced beam apparatus were found to be inconsistent with poor repeatability. As was later shown, this was due to the inconsistent fullerene quality. Furthermore, the fullerene residue -- (carbon left in the vaporizer that would not sublime) was higher than previously and reached as much as 30% of the initial load. This varied from batch to batch for a given fullerene supplier and especially from supplier to supplier. High residue is of course unacceptable (a useless mass lifted to space) so it was decided to investigate fullerene sublimation and purification using another apparatus that is simpler and removes balanced beam accuracy/thermal drift concerns.

The apparatus is shown schematically in Fig. 3.2. It consists of two separate quartz tubes, separated by a replaceable orifice. The tube on the left is loaded with fullerenes and the entire apparatus instrumented with indicated thermocouples is inserted into a 3" dia. tube style vacuum furnace. The section to the left of the orifice is located in the hot zone of the furnace and serves as the vaporizer. Most of the section to the right of the choked orifice is in the cold zone of the furnace and serves as the fullerene condenser.

BUSEK

DATA AND CURVE FIT
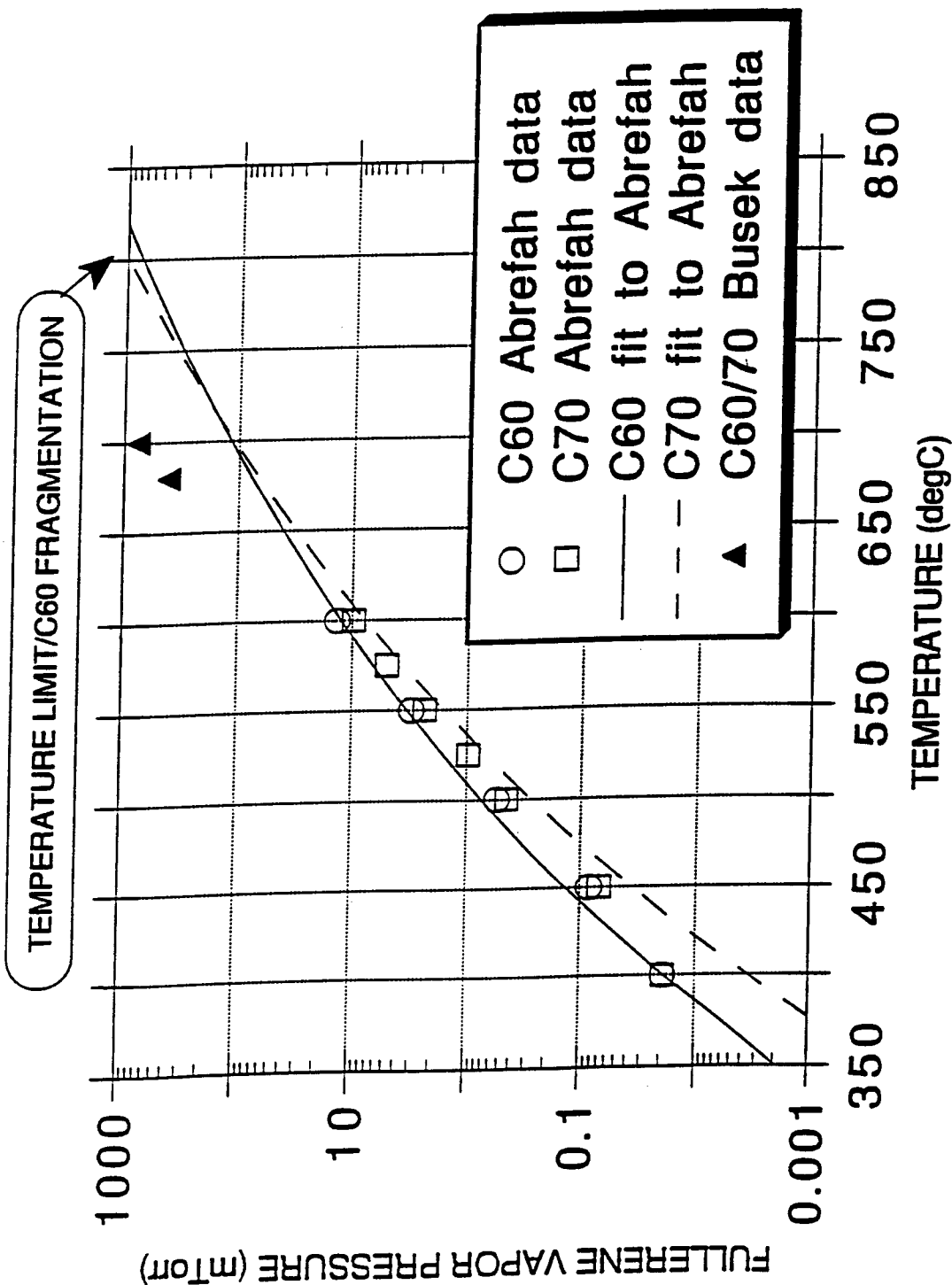
Fig. 3.1 Fullerene High Temperature Pressure Data were Calculated from Measured Mass Flow. The high temperature data obtained by Busek fall above the curve extrapolated from low temperature data by Abrefah [Ref: J. Abrefah and D.R. Orlander, "Vapor Pressure of Buckminsterfullerene," Appl. Phys. Lett. 69 (11), March 1992]

0077

12
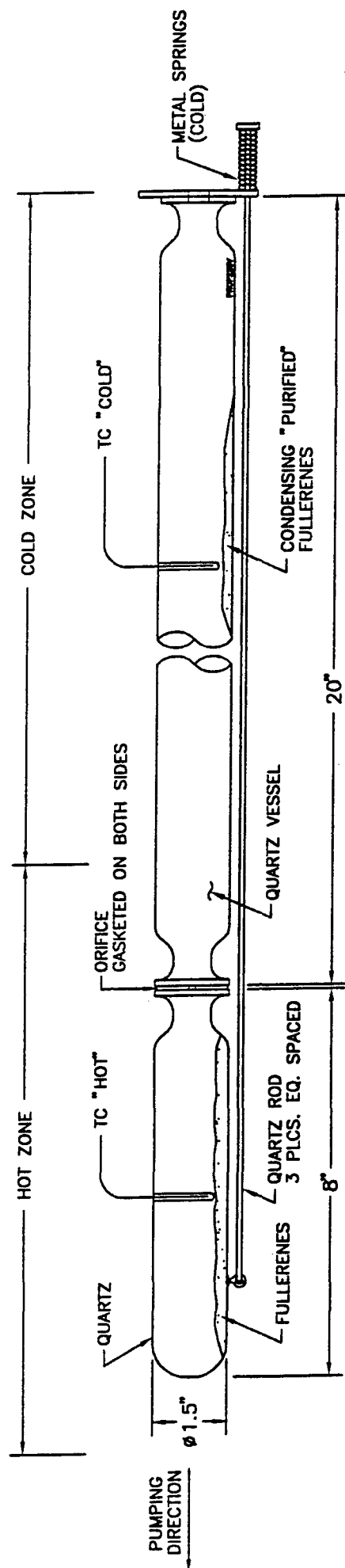
Fig. 3 .2 Fullerene Sublimation Apparatus

13

Typical test involves loading known mass of fullerenes into the vaporizer section, rapidly heating to specified temperature to minimize mass loss in the transient, holding temperature for an hour or longer depending on the test objective, followed by a rapid cool down. After that the fullerene mass in the condenser and the mass in the vaporizer is weighed. The vaporized mass and the test duration are then used to calculate $\dot{m}$ and finally the pressure from Eq. [3.1].

The results of these tests are summarized in Table 3.2 and plotted in Fig. 3.3.

All samples purchased from three different suppliers were mixed fullerenes, typically 80% C_{60} and 20% C_{70}. The suppliers were MER Corp., Bucky USA and Hoechst AG of Germany. Of these, the German material was the most consistent and yielded the most repeatable data.

The quality of the material depends on the production method, purification method and storage. Of these, the purification/extraction solvents are the most important. Typically, solvents such as benzene, toluene or CS_2 are used. The hydrocarbons enter the C_{60}/C_{70} cage and are very difficult to remove. Even traces can be responsible for polymerization of the fullerenes which may remain soluble and retain the basic geodesic structure but cannot be sublimed. A study of photo-illumination of C_{60} crystals and films[19] lead to the same conclusion. This study also reports formation of polymerized "skin" on the C_{60} crystals which then inhibits free sublimation of the interior C_{60} thereby lowering vapor pressure.

The conclusions are:

1) Pre qualification of fullerene vendors with rigid specifications for processing and storage is be required.

2) Drying of all samples is required.

3) Purification by sublimation is probably the best procedure to ensure low residue. (Most thruster tests were carried out only with in-house sublimed samples using the apparatus in Fig. 3.2. For large quantities the vendor supplying the fullerenes should carry out sublimation before delivery).

4) Fullerenes must be stored under inert gas in dark containers.

5) Direct vapor pressure measurement in the vaporizer is highly desirable but no instrumentation currently exists to perform this measurement.

6) Sublimation of the propellant should be performed at as low a temperature as possible and on as small a fraction of the total propellant as practical. This preliminary conclusion is based upon uncertainties of C_{60} behavior when repeatedly heated and possible photo-illumination induced "skin" formation by hot vaporizer walls (radiation from metal surfaces at or above 600°C is partially in the visible spectrum).

BUSEK

RUN	FULL BATCH	FULL LOAD [g]	AVR. PEAK T [K]	TIME AT T [sec]	FULL VAPORIZED [g]	FULL UNVAPORIZED [g]	FULL CONDENSED [g]	FULL LOST [g]	ORIFICE DIA [mm]	MASS FLOW [mg/sec]	VAP PRESSURE [mTorr]
36-J-01	36-01	6.97	926	3852	6.1	0.87	6.01	0.09	4.737	1.584	171.86
36-J-02	36-01	4.89	927	3792	4.18	0.71	4.04	0.14	4.737	1.102	119.69
36-J-04	36-02	8.57	887	3654	1.63	6.94	1.59	0.04	4.737	0.446	47.38
36-J-05	36-02	6.94	887	6738	0.86	6.08	0.83	0.03	4.737	0.128	13.56
36-J-06	36-02	6.08	922	7227	1.79	4.29	1.76	0.03	4.737	0.248	26.82
36-J-07	36-02	4.29	888	11157	1.38	2.91	1.37	0.01	4.737	0.124	13.14
36-J-08	36-02	2.91	922	7530	1.56	1.35	1.53	0.03	4.737	0.207	22.43
36-J-09	36-02	1.35	922	7107	0.69	0.66	0.65	0.04	4.737	0.097	10.51
36-J-10	36-02	0.66	922	6648	0.05	0.61	0.04	0.01	4.737	0.008	0.81
36-J-11	36-02	7.88	922	7554	4.46	3.42	4.37	0.09	4.737	0.590	63.94
36-J-12	36-02	3.42	920	3627	0.9	2.54	0.88	0.02	4.737	0.248	26.84
36-J-13	36-02	2.47	916	3480	0.28	2.19	0.24	0.04	4.737	0.080	8.68
36-J-14	36-02	2.17	915	3276	0.23	1.94	0.23	0	4.737	0.070	7.57
36-J-16	36-03	5.11	916	15870	0.81	4.3	0.77	0.04	4.737	0.051	5.51
36-J-17	36-03	4.30	1004	14508	4.23	0.07	4.12	0.11	4.737	0.292	32.95
36-J-18	36-03	0.27	920	900	0.18	0.09	0.17	0.01	4.737	0.200	21.63
36-J-19	36-03	5.36	918	10953	2.32	3.04	2.29	0.03	4.737	0.212	22.89
36-J-20	36-03	3.04	921	7140	1.96	1.08	1.91	0.05	4.737	0.275	29.71
36-J-21	36-03	1.07	923	3480	0.79	0.28	0.77	0.02	4.737	0.227	24.60
36-J-22	36-03	9.08	915	14085	6.35	2.73	6.23	0.12	4.737	0.451	48.63
36-J-23	36-03	8.75	919	16422	6.62	2.13	6.53	0.09	4.737	0.403	43.58
36-J-24	36-03	2.13	915	10530	0.32	1.81	0.32	0	4.737	0.030	3.28

Table 3.2   Fullerene Vapor Pressure and Purification Experiments
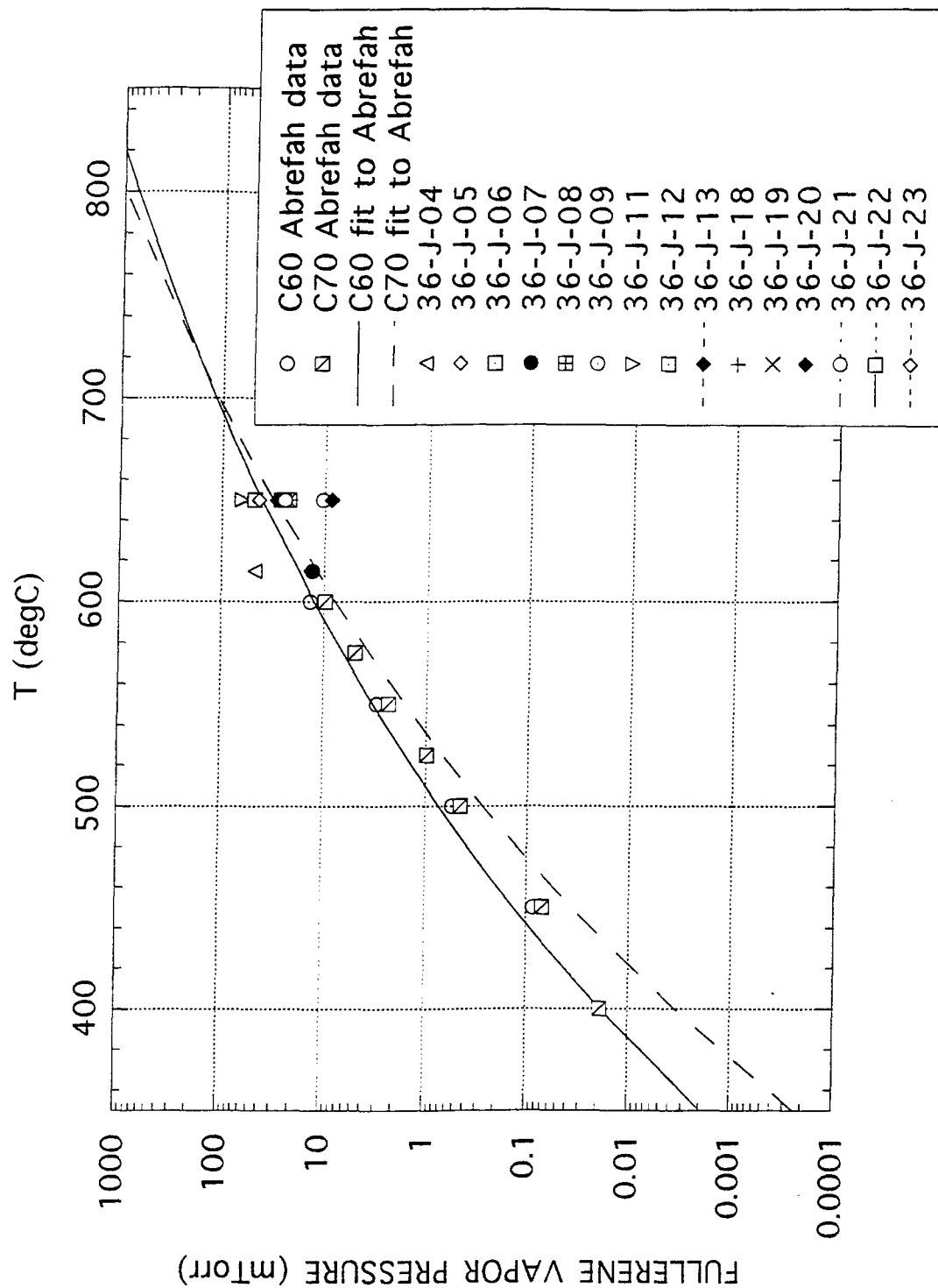
Fig. 3.3 Fullerene Vapor Pressure Data

4.0 LABORATORY FULLERENE ION THRUSTER (FIT) DESIGN AND ANALYSIS

The size of the thruster discharge chamber was selected to be approximately 15 cm and the active grid diameter is approximately 13 cm. This size is both convenient to work with and its performance should be comparable to existing fullerene ion thrusters constructed by others[2-11] discussed in Section 1.2.

This section contains the description of the overall design and performance estimates on which the design is based followed by a description of each major component of the laboratory thruster system.

4.1 Overall Design and Design Analysis

The schematic of the laboratory fullerene ion thruster designated as the FIT-13 is shown in Fig. 4.1. Unlike most laboratory thruster experiments the propellant storage and vaporization unit is inside the vacuum tank and forms structurally integral unit with the thruster itself. We are simultaneously developing both the thruster and the propellant feed systems. As usual, the power supplies, control and data acquisition system are located outside of the tank.

The sizing and design analysis of the FIT-13 system with two different grids operating at voltages ranging from 1000 to 3000 volts are shown in Tables 4.1 and 4.2. The equations used to make these predictions are summarized in Appendix B.

Table 4.1 shows the anticipated thrust, beam current, discharge current and fullerene mass flow (along with other parameters of interest) for a set of grids that have 829 of 2 mm dia. holes, spaced 4 mm apart. This set has been fabricated and represent the initial low cost, low performance version.

Table 4.2 shows the important design parameters for the same thruster with more advanced grids. The thruster system has been designed to accommodate this new higher mass flow, beam and discharge current intergrid voltage, etc., listed in this table. This set of grids may be fabricated in future programs.

4.2 Propellant Storage and Vaporization

A spacecraft with fullerene ion thrusters performing a low to GEO orbit transfer may have on board hundreds of kilograms of fullerenes. How to store the propellants and how to feed it into the vaporizer is a challenging engineering problem. Several approaches can be considered which defer depending on the spacecraft mission and hence, the amount stored .

Fundamentally they can be divided into: (1) heating the entire fuel storage in which case the storage tank becomes the vaporizer; or (2) heating small portions of the propellant in a small vaporizer that is fed incrementally or continuously from the storage tank.

Both approaches have drawbacks and advantages. The obvious disadvantage of the first approach is that one is heating large volume (of the order of 0.6 m^3 for 1000 kg of propellant) which implies large heat loss and large thermal inertia.

BUSEK

Fig. 4.1 Schematic of the 13 cm Laboratory Fullerene Ion Thruster (FIT-13)

18

Table 4.1
13cm Laboratory Fullerene Thruster

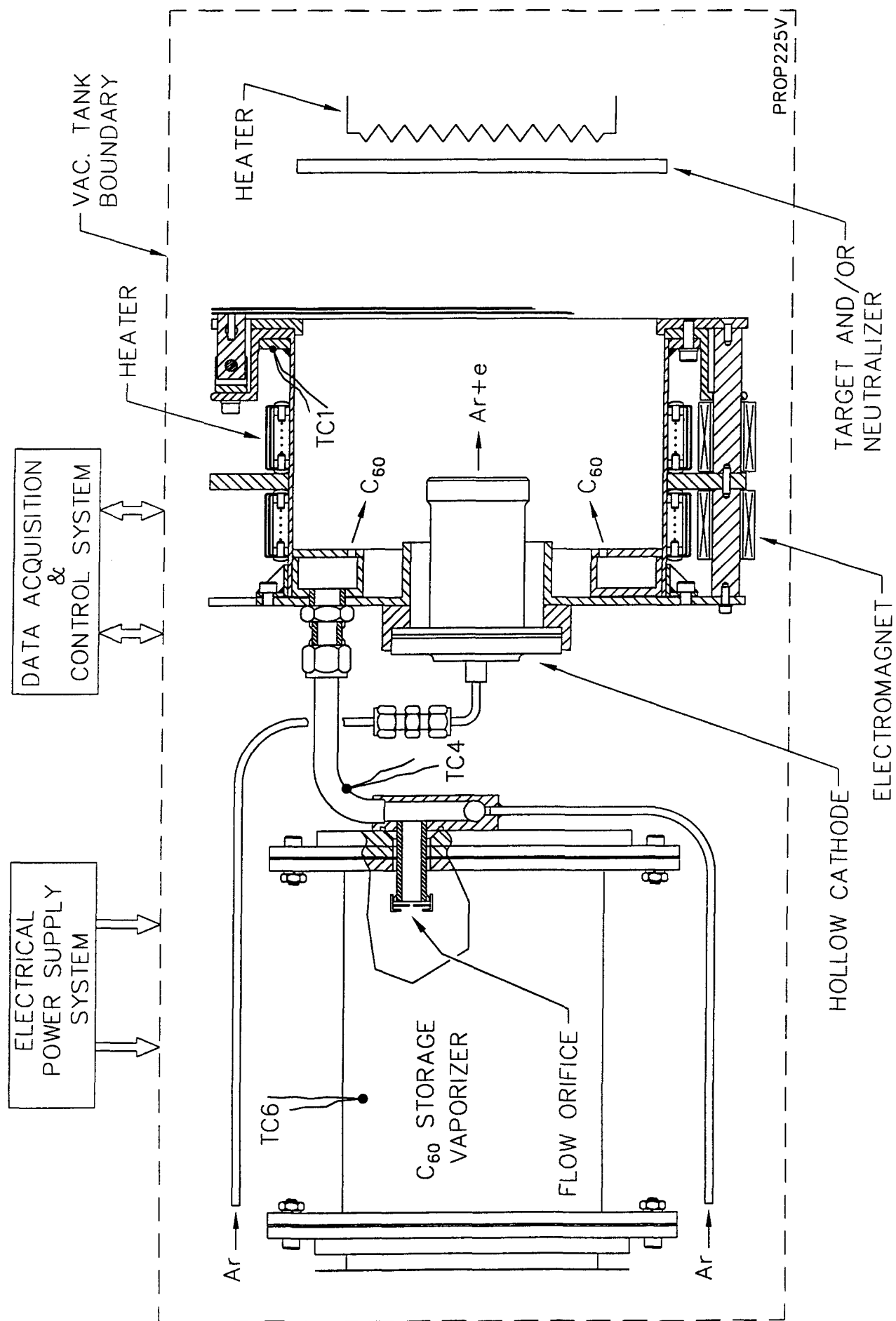| INPUT/CASE NO	1	2	3	4	5
Dact.(m) grid active dia	0.13	0.13	0.13	0.13	0.13
ds(m) screen grid hole dia.	0.002	0.002	0.002	0.002	0.002
da(m) acc. grid hole dia.	0.002	0.002	0.002	0.002	0.002
p(m) grid hole pitch	0.004	0.004	0.004	0.004	0.004
lg(m) grid spacing	0.0020	0.0020	0.0020	0.0020	0.0020
Vt(Volt) total inter. grid voltage	1000	1500	2000	2500	3000
Vn(volts) net voltage=mi*c^2/e	500	1000	1500	2000	2500
eatu(-) propellant utilization	0.8	0.8	0.8	0.8	0.8
Tn (k) guess at dis. cham. Tvapr-ITERATE	662	676	687	695	702
epsbi(volts) loss per beam ion	500	500	500	500	500
Vdis.(Volts) guess discharge voltage	30	30	30	30	30
etabase(-), base eff.	0.8	0.8	0.8	0.8	0.8
Mw(kg/kgmol) propellt mol. wt.	720	720	720	720	720
dstar vap(mm) vaporizer orifice dia.	5.8	5.8	5.8	5.8	5.8
Mwcathode(kg/kgmole) c. gas mole weight	39.9	39.9	39.9	39.9	39.9
fcn=(n of Ar)/(n of C60) cathode flow fract.	3.62	2	1.31	0.94	0.72
(vary fcn to get at most 3sccm cathode flow)					
OUTPUT - THRUSTER					
fo(-) open area fraction	0.196	0.196	0.196	0.196	0.196
Aat(m2) surface area of grid	1.327E-02	1.327E-02	1.327E-02	1.327E-02	1.327E-02
Aao(m2) open area of acc. grid	2.604E-03	2.604E-03	2.604E-03	2.604E-03	2.604E-03
N (-)numbr of holes	829	829	829	829	829
mi(kg) mass of prop. ion	1.195E-24	1.195E-24	1.195E-24	1.195E-24	1.195E-24
ci(m/sec) ion exit speed	1.158E+04	1.637E+04	2.005E+04	2.315E+04	2.589E+04
le(m) effective grid spacing	2.236E-03	2.236E-03	2.236E-03	2.236E-03	2.236E-03
J(A/m2) beam current density	1.289E+01	2.367E+01	3.645E+01	5.093E+01	6.695E+01
Ibeam (A) beam current	0.034	0.062	0.095	0.133	0.174
ni(1/m3) ion number density	6.948E+15	9.025E+15	1.135E+16	1.373E+16	1.614E+16
cn(m/sec) speed of neutrals	124	125	126	127	127
ni/nn(-)	0.0427	0.0305	0.0251	0.0219	0.0197
nn(1/m3) neutral number density	1.626E+17	2.957E+17	4.516E+17	6.275E+17	8.207E+17
ntot(1/m3) tot number density	1.696E+17	3.047E+17	4.629E+17	6.412E+17	8.368E+17
ntot(1/m3) based on Tdis. chamb. input	1.650E+17	2.940E+17	4.551E+17	6.199E+17	8.076E+17
ntot(=R42)/ntot(=R43)iteterate to =1	1.028E+00	1.036E+00	1.017E+00	1.034E+00	1.036E+00
Tdis. cavity (degC) based ntot	389	403	414	422	429
p(N/m2) in dis. cavity based on ntot	1.549E-03	2.843E-03	4.389E-03	6.150E-03	8.107E-03
p(Torr) in dis. cavity based on ntot	1.154E-05	2.118E-05	3.270E-05	4.582E-05	6.040E-05
F(N) thrust from eq.4	0.0029	0.0075	0.0142	0.0229	0.0337
F(grams)) thrust from eq.4	0.30	0.77	1.45	2.34	3.44
mdot(kg/sec) mass flow eq.5	3.129E-07	5.749E-07	8.851E-07	1.237E-06	1.626E-06
mdot(mg/sec) mass flow eq.5	0.313	0.575	0.885	1.237	1.626
Isp(sec) specific impls	947	1338	1638	1891	2114
etat(-) thrust efficiency	0.40	0.53	0.60	0.64	0.67
Pttl=F^2/(2*mdot*eta)	33.73	92.80	190.37	332.43	524.24
Pdis=Pttl-Pbeam=Pttl-Ibeam*Vnet	16.95	31.17	48.04	67.21	88.45
Idis.(amps)=Pdis/Vdis	0.57	1.04	1.60	2.24	2.95
OUTPUT - VAPORIZER					
guess Tv(degC)	625	653	673	689	703
Pc60(mTorr)	2.23E+01	4.25E+01	6.59E+01	9.22E+01	1.23E+02
Pc60(N/m2)	3.00E+00	5.71E+00	8.84E+00	1.24E+01	1.65E+01
mdot c60 (mg/sec)	3.10E-01	5.82E-01	8.91E-01	1.24E+00	1.63E+00
mdot/mdot(from row#52)	0.99	1.01	1.01	1.00	1.00
(iterate Tv to get Mdot/mdot=1)					
OUTPUT - cathode max flow					
Nc.gas(1/m3) cathode gas number densty	6.14E+17	6.09E+17	6.06E+17	6.03E+17	6.03E+17
cc(m/sec) thermal speed of cathode gas	525	531	535	538	541
mdot.cgas(mg/sec)	5.56E-02	5.58E-02	5.60E-02	5.59E-02	5.62E-02
Vdot cgas(sccm) (keep at min.=about 2sccm)	2.00E+00	2.00E+00	2.01E+00	2.01E+00	2.02E+00
mass fration (mdot cgas/mdotC60)	1.78E-01	9.70E-02	6.32E-02	4.52E-02	3.46E-02

19

Table 4.2
13cm Laboratory Fullerene Thruster

INPUT/CASE NO	1	2	3	4	5
Dact.(m) grid active dia	0.13	0.13	0.13	0.13	0.13
ds(m) screen grid hole dia.	0.002	0.002	0.002	0.002	0.002
da(m) acc. grid hole dia.	0.002	0.002	0.002	0.002	0.002
p(m) grid hole pitch	0.003	0.003	0.003	0.003	0.003
lg(m) grid spacing	0.0020	0.0020	0.0020	0.0020	0.0020
Vt(Volt) total inter. grid voltage	1000	1500	2000	2500	3000
Vn(volts) net voltage=mi*c^2/e	500	1000	1500	2000	2500
eatu(-) propellant utilization	0.8	0.8	0.8	0.8	0.8
Tn (k) guess at dis. cham. Tvapr-ITERATE	662	676	687	695	702
epsbi(volts) loss per beam ion	500	500	500	500	500
Vdis.(Volts) guess discharge voltage	30	30	30	30	30
etabase(-), base eff.	0.8	0.8	0.8	0.8	0.8
Mw(kg/kgmol) propellt mol. wt.	720	720	720	720	720
dstar vap(mm) vaporizer orifice dia.	5.8	5.8	5.8	5.8	5.8
Mwcathode(kg/kgmole) c. gas mole weight	39.9	39.9	39.9	39.9	39.9
fcn=(n of Ar)/(n of C60) cathode flow fract.	2.05	1.13	0.74	0.53	0.41
(vary fcn to get at most 3sccm cathode flow)					
OUTPUT - THRUSTER					
fo(-) open area fraction	0.349	0.349	0.349	0.349	0.349
Aat(m2) surface area of grid	1.327E-02	1.327E-02	1.327E-02	1.327E-02	1.327E-02
Aao(m2) open area of acc. grid	4.629E-03	4.629E-03	4.629E-03	4.629E-03	4.629E-03
N (-)numbr of holes	1474	1474	1474	1474	1474
mi(kg) mass of prop. ion	1.195E-24	1.195E-24	1.195E-24	1.195E-24	1.195E-24
ci(m/sec) ion exit speed	1.158E+04	1.637E+04	2.005E+04	2.315E+04	2.589E+04
le(m) effective grid spacing	2.236E-03	2.236E-03	2.236E-03	2.236E-03	2.236E-03
J(A/m2) beam current density	1.289E+01	2.367E+01	3.645E+01	5.093E+01	6.695E+01
Ibeam (A) beam current	0.060	0.110	0.169	0.236	0.310
ni(1/m3) ion number density	6.948E+15	9.025E+15	1.135E+16	1.373E+16	1.614E+16
cn(m/sec) speed of neutrals	124	125	126	127	127
ni/nn(-)	0.0427	0.0305	0.0251	0.0219	0.0197
nn(1/m3) neutral number density	1.626E+17	2.957E+17	4.516E+17	6.275E+17	8.207E+17
ntot(1/m3) tot number density	1.696E+17	3.047E+17	4.629E+17	6.412E+17	8.368E+17
ntot(1/m3) based on Tdis. chamb. input	1.650E+17	2.940E+17	4.551E+17	6.199E+17	8.076E+17
ntot(=R42)/ntot(=R43)Iteterate to =1	1.028E+00	1.036E+00	1.017E+00	1.034E+00	1.036E+00
Tdis. cavity (degC) based ntot	389	403	414	422	429
p(N/m2) in dis. cavity based on ntot	1.549E-03	2.843E-03	4.389E-03	6.150E-03	8.107E-03
p(Torr) in dis. cavity based on ntot	1.154E-05	2.118E-05	3.270E-05	4.582E-05	6.040E-05
F(N) thrust from eq.4	0.0052	0.0134	0.0253	0.0408	0.0599
F(grams)) thrust from eq.4	0.53	1.37	2.58	4.16	6.11
mdot(kg/sec) mass flow eq.5	5.563E-07	1.022E-06	1.573E-06	2.199E-06	2.891E-06
mdot(mg/sec) mass flow eq.5	0.556	1.022	1.573	2.199	2.891
Isp(sec) specific impls	947	1338	1638	1891	2114
etat(-) thrust efficiency	0.40	0.53	0.60	0.64	0.67
Pttl=F^2/(2*mdot*eta)	59.96	164.98	338.44	590.98	931.98
Pdis=Pttl-Pbeam=Pttl-Ibeam*Vnet	30.14	55.41	85.40	119.49	157.24
Idis.(amps)=Pdis/Vdis	1.00	1.85	2.85	3.98	5.24
OUTPUT - VAPORIZER					
guess Tv(degC)	651	680	701	719	733
Pc60(mTorr)	4.07E+01	7.64E+01	1.18E+02	1.68E+02	2.20E+02
Pc60(N/m2)	5.46E+00	1.03E+01	1.58E+01	2.26E+01	2.95E+01
mdot c60 (mg/sec)	5.57E-01	1.03E+00	1.57E+00	2.22E+00	2.89E+00
mdot/mdot(from row#52)	1.00	1.01	1.00	1.01	1.00
(iterate Tv to get Mdot/mdot=1)					
OUTPUT - cathode max flow					
Nc.gas(1/m3) cathode gas number densty	3.48E+17	3.44E+17	3.43E+17	3.40E+17	3.43E+17
cc(m/sec) thermal speed of cathode gas	525	531	535	538	541
mdot.cgas(mg/sec)	5.60E-02	5.60E-02	5.62E-02	5.61E-02	5.69E-02
Vdot cgas(sccm) (keep at min.=about 2sccm)	2.01E+00	2.01E+00	2.02E+00	2.01E+00	2.04E+00
mass fration (mdot cgas/mdotC60)	1.01E-01	5.48E-02	3.57E-02	2.55E-02	1.97E-02

The second approach, where one can consider feeding pelletized fuel using gun-like magazines, requires complex mechanical system with a hermetic seal in between the vaporizer and the storage tank so that fullerene vapor does not flow back into the storage tank where it would condense. The hermetic seal would have to be basically a high temperature valve operating at up to 700°C so that condensation does not occur within it, which could freeze it up and plug the conduit. The pros and cons of these approaches are summarized in Table 4.3.

4.2.1 Laboratory Vaporizer and Storage

As indicated in Fig. 4.1 for the laboratory version of the FIT-13, we selected Option #1 from Table 4.3 which is the more likely approach for the "early" fullerene thruster application in space and for material processing on the ground.

Per Table 4.2 the design vaporization rate is 5 mg/sec. The volume of the vaporizer was selected to be 850 cm^3 which will deliver 5 mg/sec for approximately 50 hours when initially 60% full. The maximum vaporizer temperature was selected to be 750°C because at approximately 800°C fullerenes start to fragment. Because the fullerene vapor pressure is exponentially dependent on temperature, the vaporizer internal surface temperature uniformity requirement was selected to be ±5°C. Worst case analysis indicate that the required heater power to maintain the laboratory vaporizer at the design temperature is 1500 Watts. This can be mitigated by adding more radiation shields.

The fullerene wetted inside surface of the vaporizer are made of SST 316. The temperature uniformity is achieved by explosion bonding Cu layer into the SST inside layer. The copper acts as a heat spreader. Heating was initially accomplished by tungsten wire threaded through Aℓ_2O$_3$ tubes and placed in grooves in the Cu layer. Later the tungsten wire and Aℓ_2O$_3$ insulators were replaced by swaged tantalum cable. The general construction is shown in the photograph of the partially assembled vaporizer in Fig. 4.2.

Fullerene vapor is transported through two 0.375 dia. SST 304 tubes into the fullerene manifold located inside the discharge chamber. The size of the transport lines was selected on the basis of Fig. 4.3 which shows an orifice diameter vs. fullerene vapor temperature. The graph was constructed with the aid of Eqs. [3.1] and [3.2].
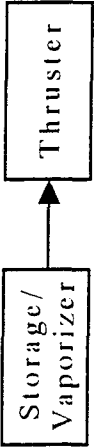
4.2.2 Future Vaporizer and Feeding System Concept

The fundamental options of heating all propellant in a single large volume that serves as a storage and a vaporizer or a small fraction of the propellant fed incrementally into a small vaporizer were discussed at the beginning of Section 4.2 and Table 4.3. For long term missions it may be advantageous to choose Option 2 from Table 4.3 for the following reasons:

1) The C$_{60}$/C$_{70}$ thermal degradation appears to be a function of not only temperature but also time at temperature and number of reheat cycles. Thus, heating a large volume of propellant and keeping it hot for the whole time an orbit may not be advisable (aside of heat losses consideration).

2) Heating a large volume of propellant just for the thruster operating period which may be as short as 1/2 hour per day would be extremely energy intensive and may affect the vapor pressure depending on the number of reheat cycles.

Thus, feeding a small fraction of the propellant into a small vaporizer with fast heat up and low thermal losses may be the best approach. Final determination will however, require data from long duration fullerene vaporization experiments. The transport of the solid fullerenes from a large

BUSEK

Table 4.3 Fundamental Options for Fullerene Storage and Vapor Generation

Configuration	Pros	Cons
Option 1 Storage/Vaporizer → Thruster	- Passive System - No mechanism to incrementally feed propellant - Hence, more reliable	- Large volume/mass to heat - Large heat losses - Large thermal inertia
Option 2 Storage — Vaporizer — Thruster	- Low power to vaporizer due to low volume - Low thermal losses - Low thermal inertia/fast response	- Complex mechanical feed system - Requires high temperature valve between storage and vaporizer - System failes if the valve fails
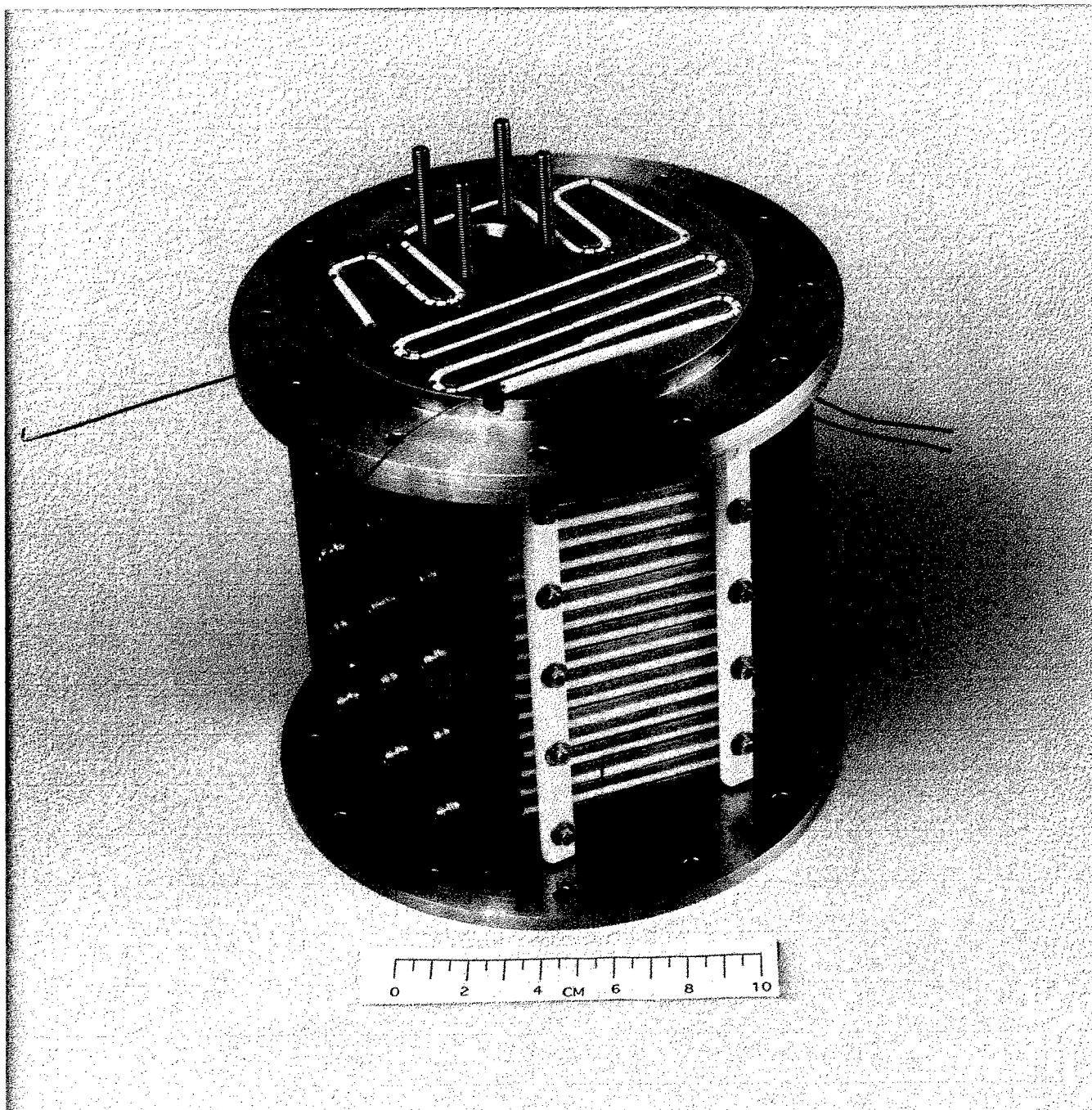
0260

Fig. 4.2 Partially Assembled Fullerene Vaporizer
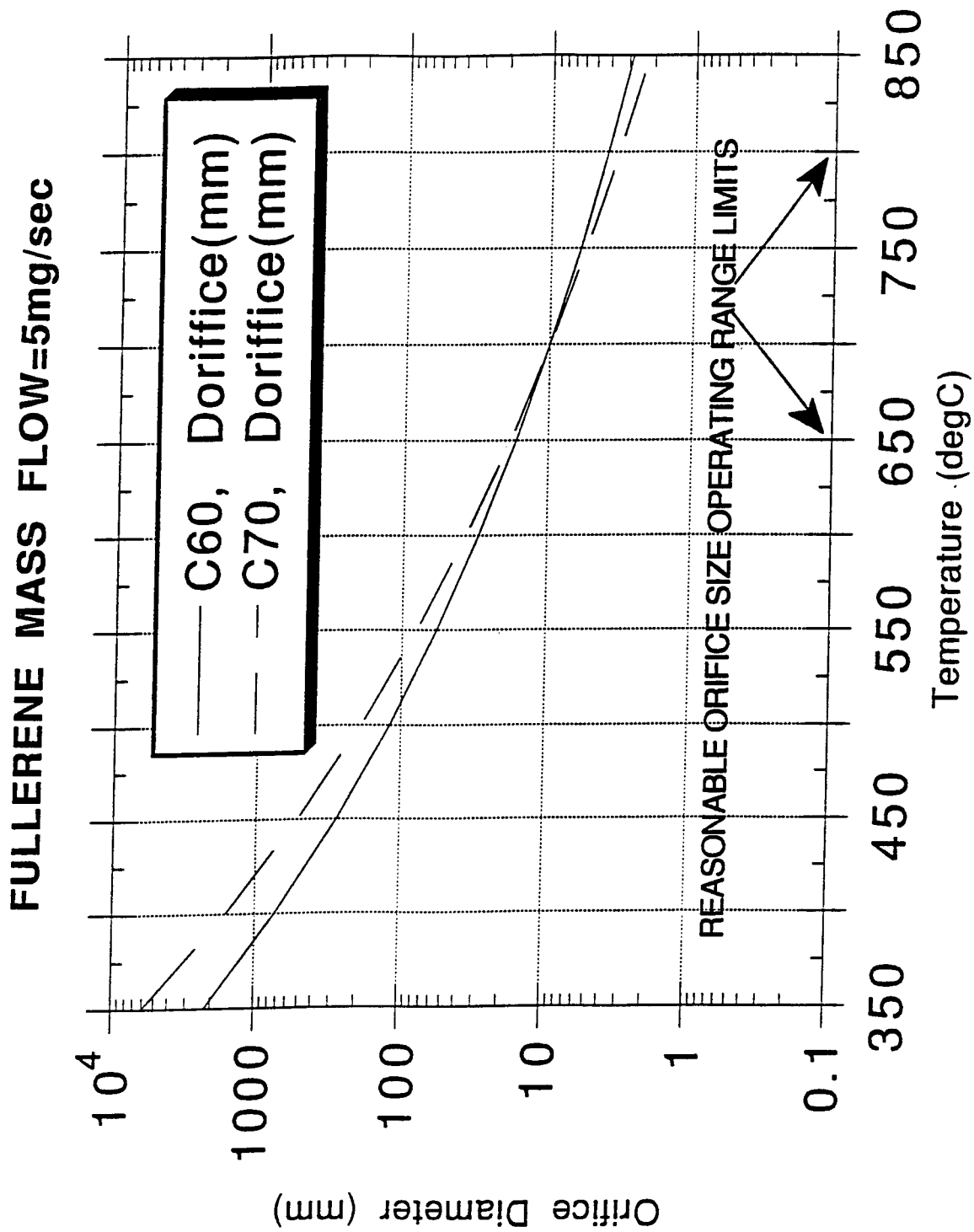
Fig. 4.3 Orifice Size for 5 mg/sec Fullerene Mass Flow vs. Vapor Temperature

24

storage tank to a small vaporizer and the rejection of unvaporized fullerene residue from the vaporizer which may be necessary, makes this approach difficult to implement. A concept which appears to deserve further exploration is shown in Fig. 4.4 which depicts a conceptual sketch of an incremental fullerene storage and feeding system. The C_{60} powder is stored pressed in a cartridge of some desirable volume, say 10 to 50 grams depending on the mission. An arbitrary number of cartridges are strung together in a machine gun-like belt. The cartridges could be made of some suitable light weight plastic, metal or even quartz. To insert the propellant into the vaporizer, the cartridge is positioned in front of the breach and a piston forces the compressed powder into a small vaporizer. The breach closes and provides a gas tight seal at temperature $T = 700°C$. If it is shown that unvaporized residue is significant and must be periodically removed from the vaporizer, then the whole cartridge (for example, made of quartz) must be inserted into the vaporizer and heated and after a cool down, the cartridge with the unvaporized residue in it is then ejected.

There are many variations on this basic concept. An appealing feature of this approach is that the unvaporized residue (if any) can be rejected and that the system is scaleable for any quantity of propellant by making the belt longer. The mechanism does not appear overly complicated except for the breach (i.e., gas tight, high temperature valve).

4.3 Thruster Design

The schematic of the FIT-13 thruster is shown in Fig. 4.5. Unlike conventional Xe fueled ion thruster, the FIT must have heated walls to prevent condensation of fullerene ions. The minimum wall temperatures are listed in Tables 4.1 and 4.2 for two different grid designs. Cusp magnetic field was initially provided by the indicated electromagnets and later replaced by permanent rod magnets (see Section 5). Another consequence of high discharge chamber wall temperature is the need to provide heat shields around the whole vaporize/thruster flow train and to accommodate differential thermal growth of the discharge chamber and the grids which necessitates pivoting dielectric grid mounting system. These features that set it apart from the conventional ion thruster and the salient components of the FIT-13 are described in the subsequent section.

4.3.1 Cathode

The hollow cathode schematic is shown in Fig. 4.6. The fundamental approach to the design follows NASA JPL and NASA Lewis designs.[21,22] The cartridge emitter is tungsten impregnated with Ba and Ca oxides. The orifice size is approximately 0.033". The orifice plate is made of W and replaceable to allow easy change of orifice size. The cathode shroud (enclosure) is isolated and serves as a keeper electrode. The heater was initially made of BN with VM type tungsten wire as the heating element and later replaced by swaged tantalum cable. This approach was taken to permit the replaceability of the orifice plate size. Orifice size in combination with internal Ar pressure dictates the Ar mass flow which must be sufficient to preclude diffusion of C_{60} ions into the hollow cathode interior thereby lowering its emissivity.

Several tests were conducted with the hollow cathode replaced by 2% Th tungsten wire cathode that was heated by separate power supply. The design of this cathode is shown in Fig. 4.7.

4.3.2 Discharge Chamber

The unconventional features of the FIT-13 are the discharge chamber heaters and the magnetics to create the desired cusp field.

BUSEK

VAPOR TO THRUSTER

VAPORIZER

NEEDS A HIGH TEMPERATURE VALVE

C_{60} CARTRIDGE

BELT WITH CARTRIDGES

EMPTIES (TO BE EJECTED)

1.9cm DIA.

4.25cm
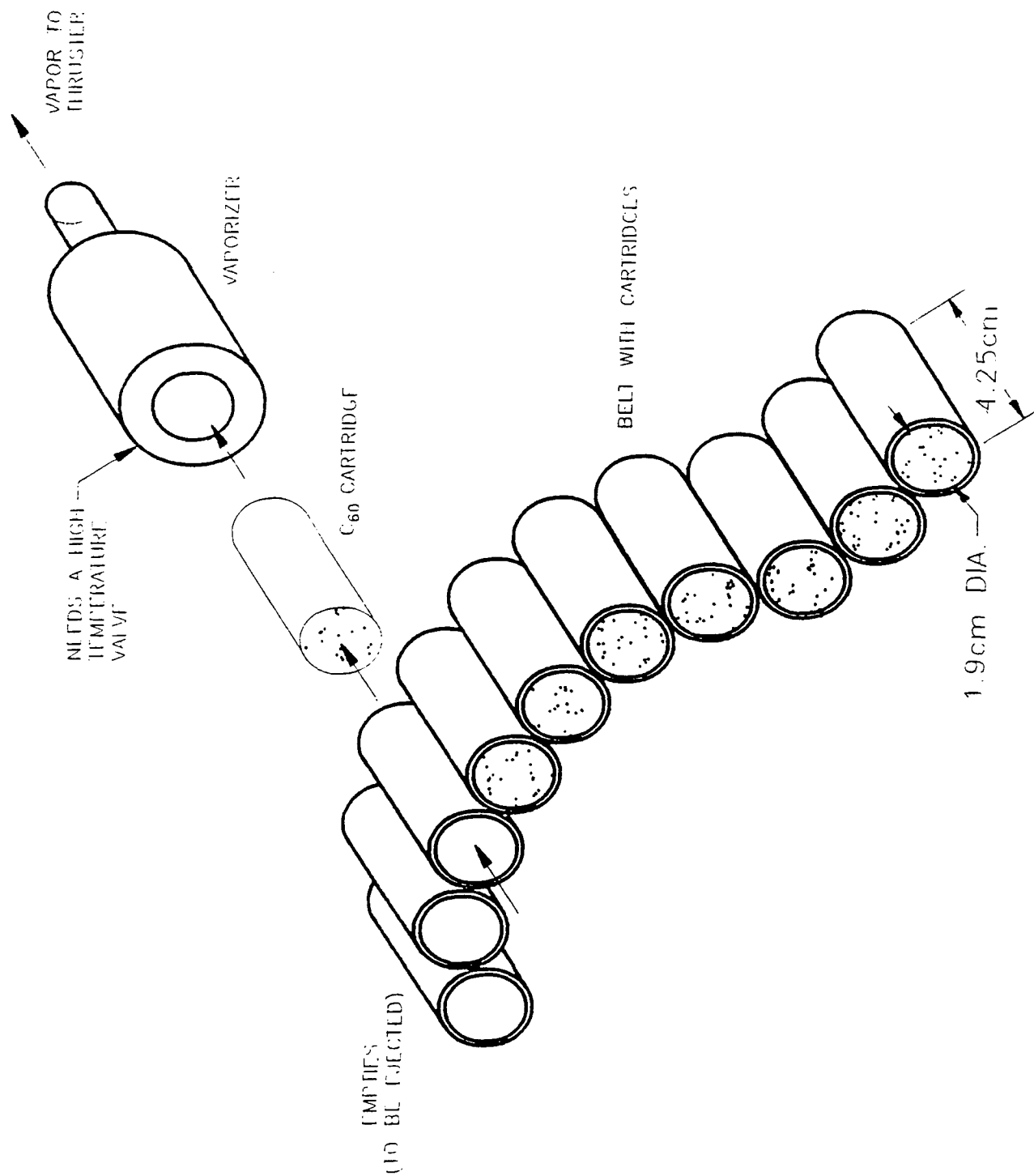
Fig. 4.4 Schematic of Incremental Feeding and Vaporization System for Long Term Missions
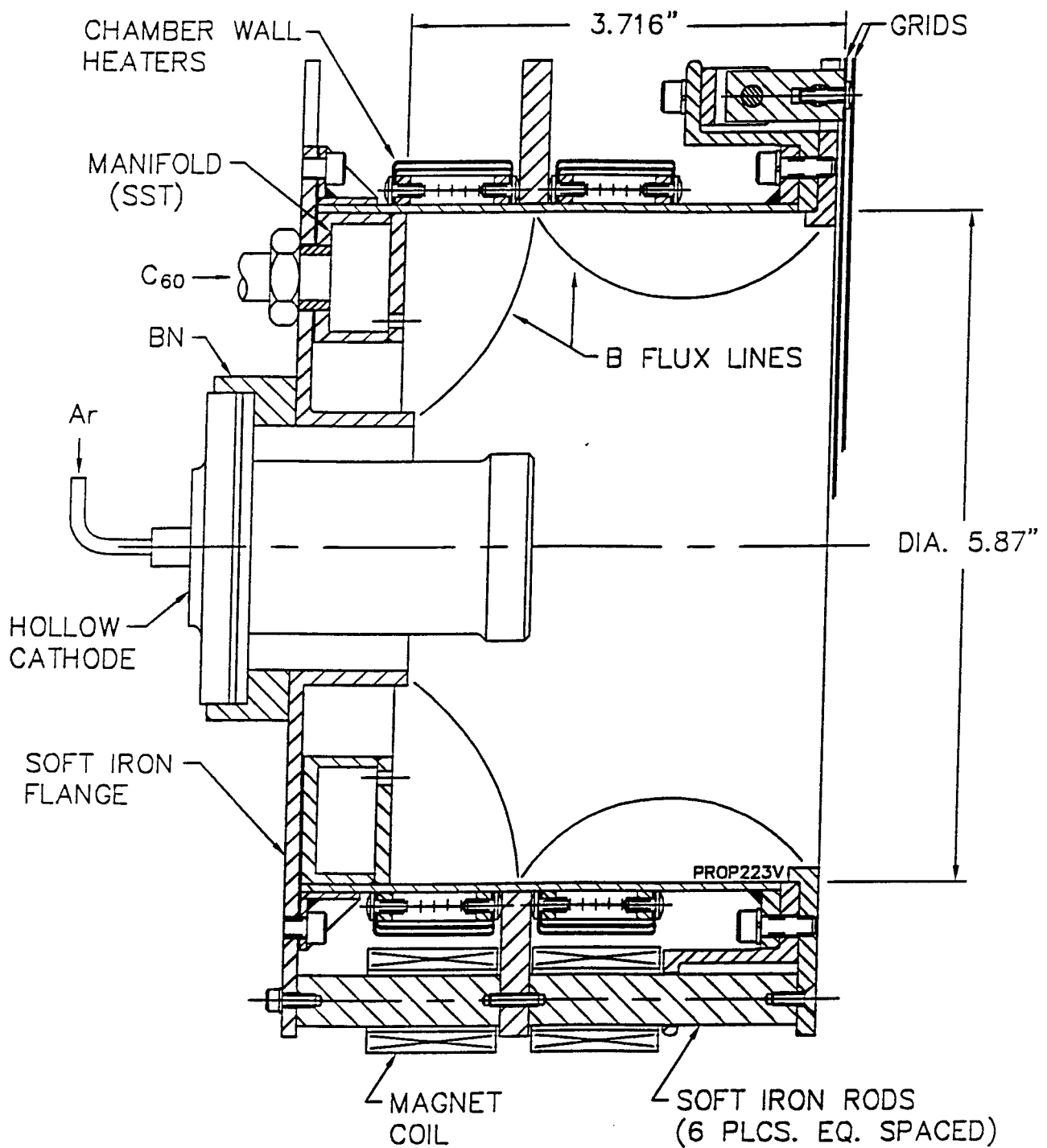
Fig. 4.5 FIT-13 Discharge Chamber Schematic
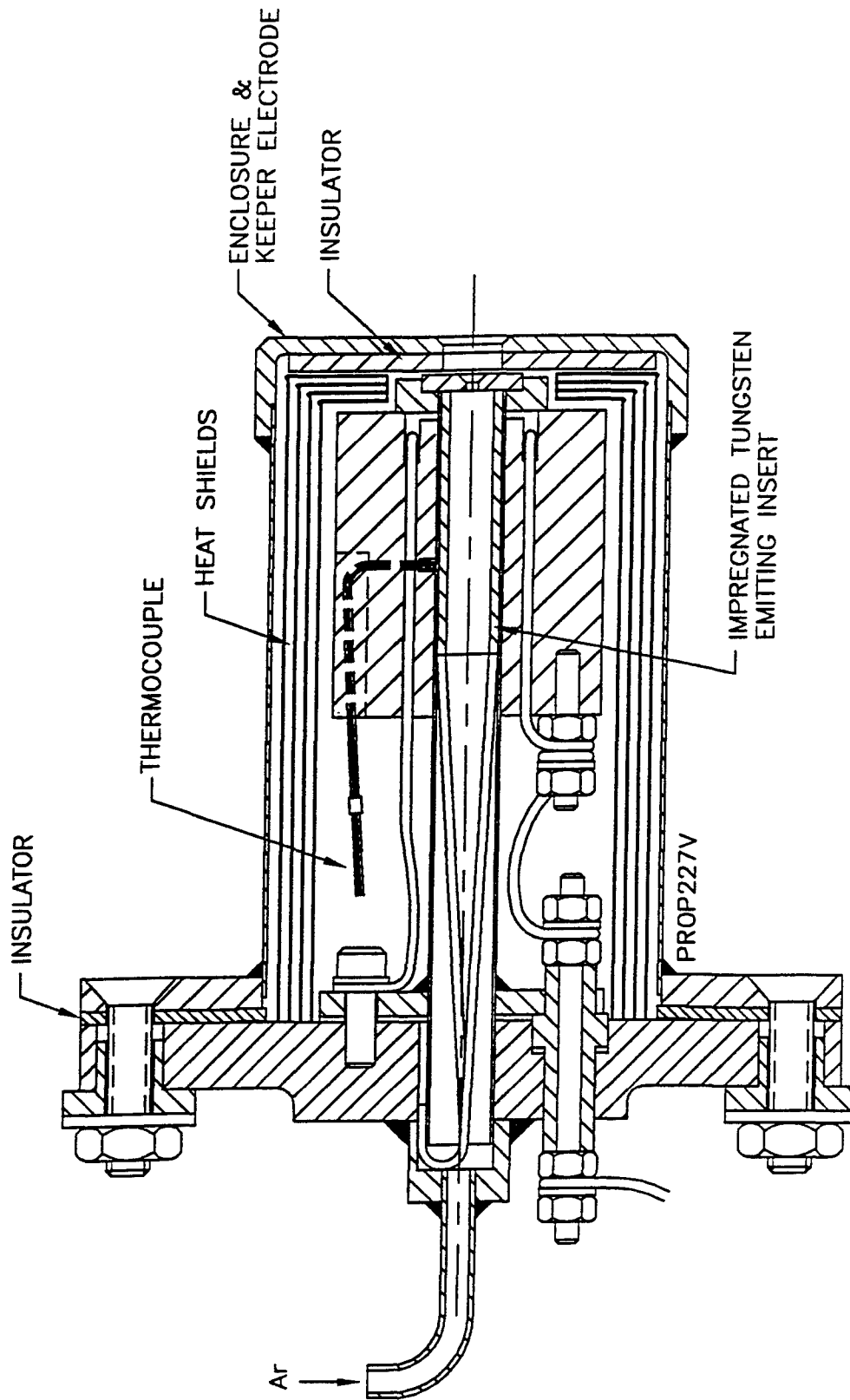
Fig. 4.6 Hollow Cathode Operated on Ar for the FIT-13

INSULATOR

THERMOCOUPLE

HEAT SHIELDS

ENCLOSURE & KEEPER ELECTRODE

INSULATOR

IMPREGNATED TUNGSTEN EMITING INSERT

PROP227V

Ar

POWER
LEAD

ALUMINA
SLEEVE

Ar
(OPTIONAL)

PROP285V

2% THORIATED
TUNGSTEN WIRE
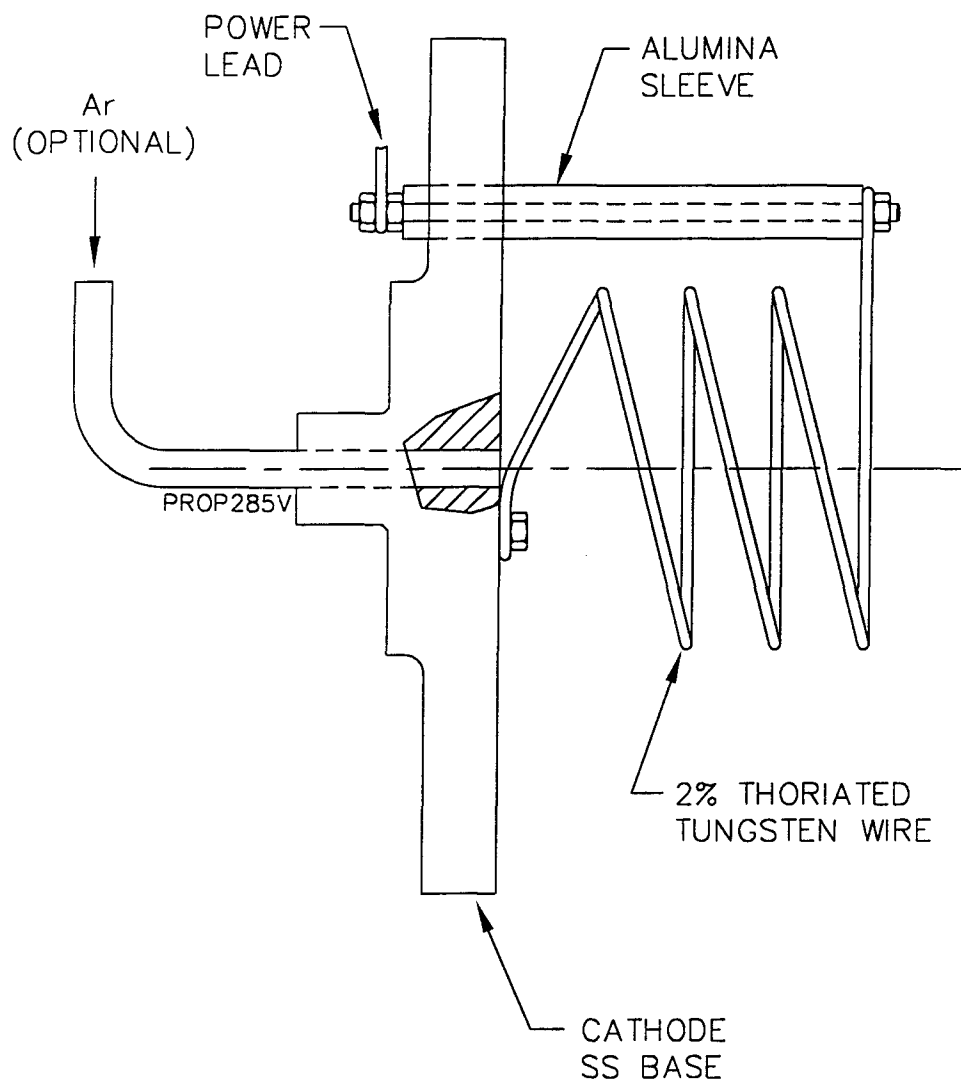
CATHODE
SS BASE

Fig. 4.7 Tungsten Filament Cathode

BUSEK

The heaters initially consisted of a double wound coil made of VM tungsten wire with radiation heat shields. There were two identical heaters that fit over the outside diameter of the discharge chamber as indicated in Fig. 4.5. The double winding was employed to ensure that magnetic fields generated by the heaters are near zero as one winding cancels the magnetic field of the other. The estimated total heat power to maintain the discharge chamber walls at about 500°C is 350 Watts. This assumes no discharge on the inside and which reduces the heater input power. Further reduction can be obtained by additional heat shields. The VM tungsten heaters were later replaced by a heated insert into the discharge chamber which is further discussed in Section 5.

The magnetic structure is shown in Fig. 4.8. The goal of the design was to create magnetic field contours similar to the high performance thrusters with cusp field reported by Sovey[20] and Matossian, et al.[21] The field was initially created by a set of 12 coils located on 12 soft iron rods. The rods mate up against a soft iron mid flange conducting the opposite direction flux into this flange. The flux lines split into B1 and B2 components on the inside of the discharge chamber as indicated. The B1 flux lines are conducted through the soft iron flange that surrounds the hollow cathode in the rear of the thruster. The B2 flux lines are conducted through the front soft iron flange. Other magnetic materials may be used in the flight version of the thruster that have higher saturation field and therefore require less material to conduct the flux. A list of materials to be considered is shown in Table 4.4. The electromagnetic coils were later replaced by permanent magnets which are further discussed in Section 5.

The design calculations were carried out using the 2D version of a commercial finite element numerical code known as Maxwell. The geometry of the physical situation which as implemented is three-dimensional, had to be modified for the 2D software package. The modified geometry which approximates the actual design in the thruster interior flux and B field magnitude is shown in Fig. 4.9. The 12 magnets employed in practice are replaced by 2 coils as indicated and the magnetic rods are replaced by a continuous soft iron shell. The cross-sectional area of each physical rod is equal to 1/6 of the cross-sectional area of the shell. Matching the flux in the shell to the iron rods will yield the same B field distribution in the discharge chamber. The calculated flux lines are shown in Fig. 4.10 and the maximum field contours are shown in Fig. 4.11.

4.3.3 Grid Design

Two grid sets have been designed following the principals set out by Rovang and Wilbur.[22] Each set is specified in Table 4.5. The major difference between the two sets is the hole pitch (center-to-center distance) which is 4 mm for set 1 and 3 mm for set 2. As a result set 1 has 829 holes in each grid and set 2 has 1474 holes in each grid. The material of construction is Molybdenum. To save funds the grids were made flat and only one set has been made. Performance of each set is estimated in Tables 4.1 and 4.2 and also in Appendix A.

Each grid is mounted on 6 pivoting posts made of hot pressed SiN. Each post pivots on a pin with its retaining bracket mounted on the discharge chamber. This allows unrestrained independent differential thermal expansion in the radial direction of the discharge chamber and the grids.

4.3.4 Electrical System

The FIT-13 electrical system schematic is shown in Fig. 4.12. It appears unusually complex because it contains several elements not associated with a conventional ion thruster. This includes the fullerene vaporization chamber with two heaters each with an independent power supply, discharge cavity heater and a power supply plus discharge chamber electromagnets with its power supply. Additionally, the schematic contains separately heated beam target/collector.

BUSEK
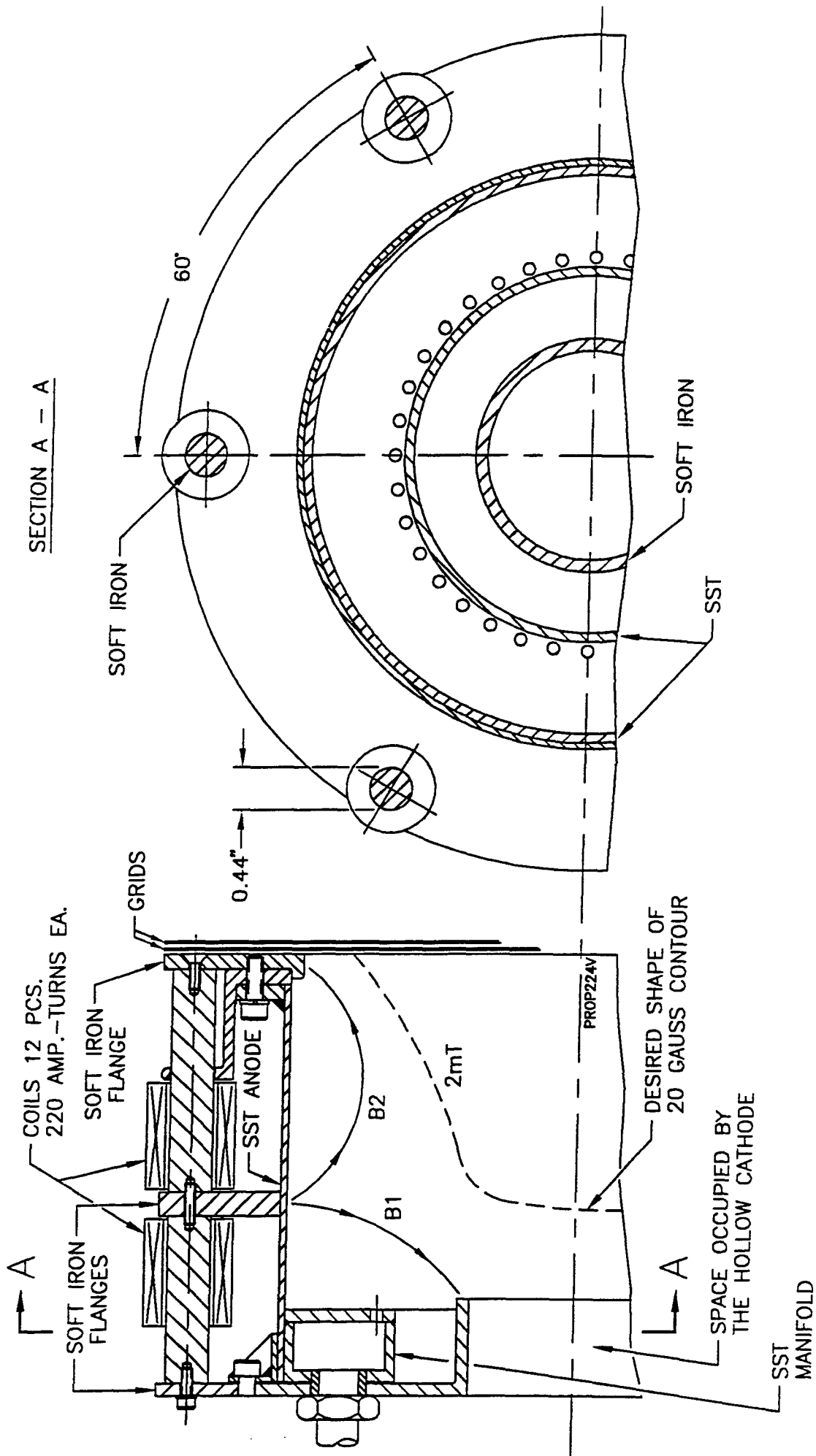
Fig. 4.8 Magnetic Structure for the FIT-13 Laboratory Thruster

Table 4.4   Magnetic Core Material Characteristics

Trade Names	Composition	Saturated Flux Density* Tesla	DC Coercive Force Amp-Turn/cm	Squareness Ratio	Material Density** g/cm³	Curie Temp.	Weight Factor
Supermendur Permendur	49% Co 49% Fe 2% V	1.9-2.2	0.18-0.44	0.90-1.0	8.15	930	1.066
Magnesil Silectron Microsil Supersil	3% Si 97% Fe	1.5-1.8	0.5-0.75	0.85-0.75	7.63	750	1.00
Deltamax Orthonol 49 Sq Mu	50% Ni 50% Fe	1.4-1.6	0.125-0.25	0.94-1.0	8.24	500	1.079
Allegheny 4750 48 Alloy Carpenter 49	48% Ni 52% Fe	1.15-1.4	0.062-0.187	0.80-0.92	8.19	480	1.073
4-79 Permalloy Sp Permalloy 80 Sq Mu 79	79% Ni 17% Fe	0.66-0.82	0.025-0.82	0.80-1.0	8.73	460	1.144
Supermalloy	78% Ni 17% Fe 5% Mo	0.65-0.82	0.0037-0.01	0.40-0.70	8.76	400	1.148
Ferrites F N27 3C8	Mn Zn	0.45-0.50	0.25	0.30-0.5	4.8	250	0.629

*Tesla = 10^4 Gauss   **g/cm^3 = 0.036 lb/in^3

BUSEK

32
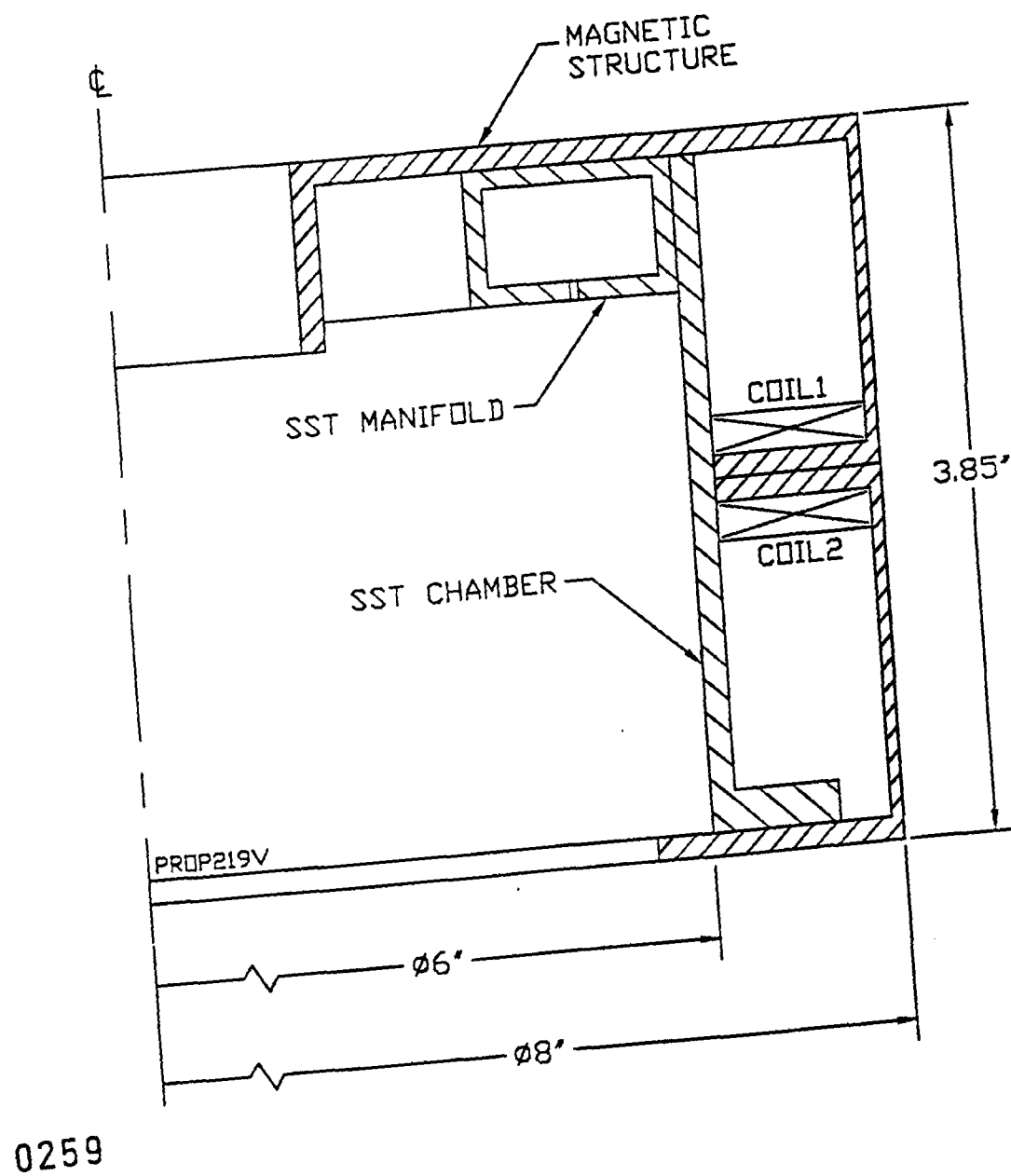
Fig. 4.9 2D Magnetic Circuit Schematic of the FIT-13 for Maxwell Modeling

0259

BUSEK

3.5000e-005
3.0333e-005
2.5667e-005
2.1000e-005
1.6333e-005
1.1667e-005
7.0000e-006
2.3333e-006
-2.3333e-006
-7.0000e-006
-1.1667e-005
-1.6333e-005
-2.1000e-005
-2.5667e-005
-3.0333e-005
-3.5000e-005
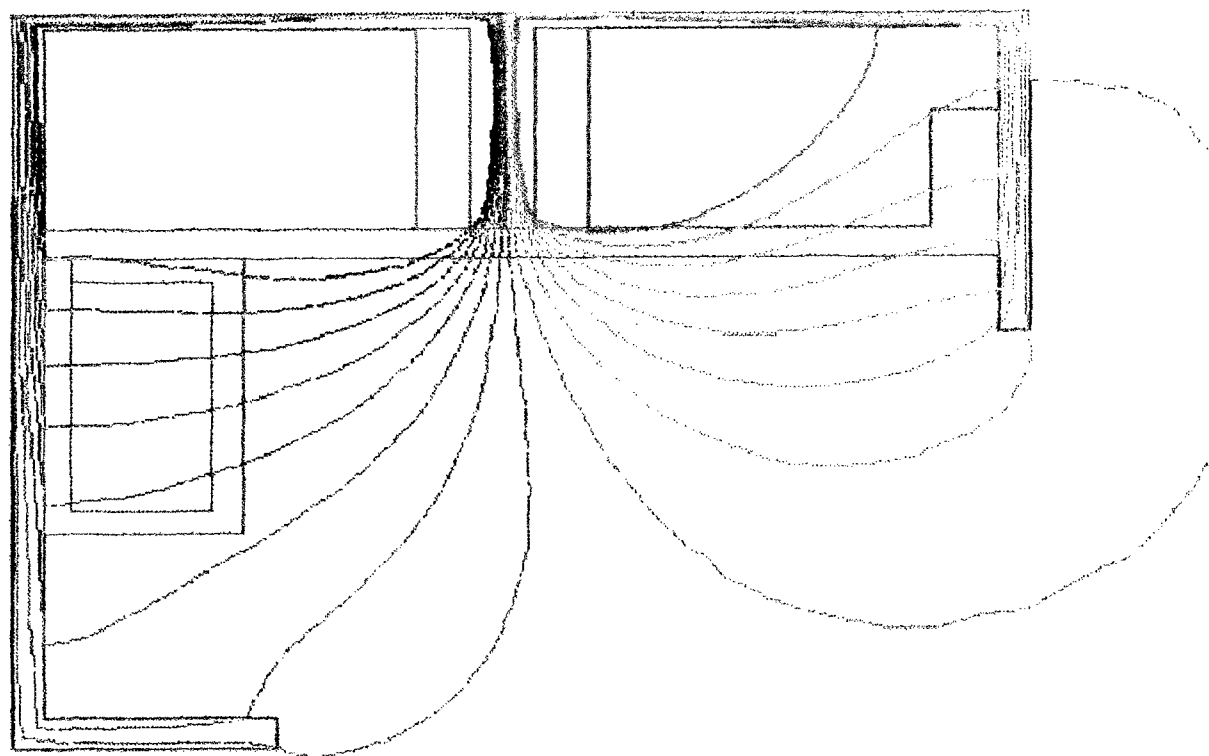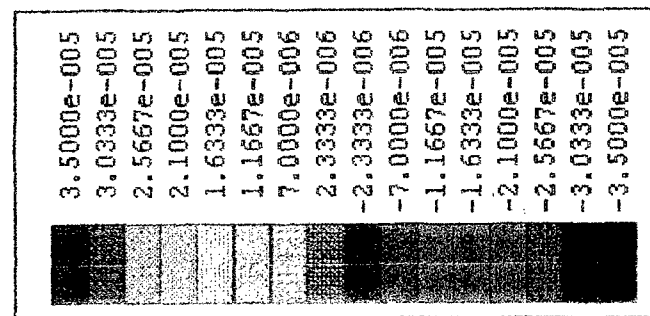
Fig. 4.10 Calculated Flux Lines for the FIT-13

| 5.0000e-002 |
| 4.6800e-002 |
| 4.3600e-002 |
| 4.0400e-002 |
| 3.7200e-002 |
| 3.4000e-002 |
| 3.0800e-002 |
| 2.7600e-002 |
| 2.4400e-002 |
| 2.1200e-002 |
| 1.8000e-002 |
| 1.4800e-002 |
| 1.1600e-002 |
| 8.4000e-003 |
| 5.2000e-003 |
| 2.0000e-003 |
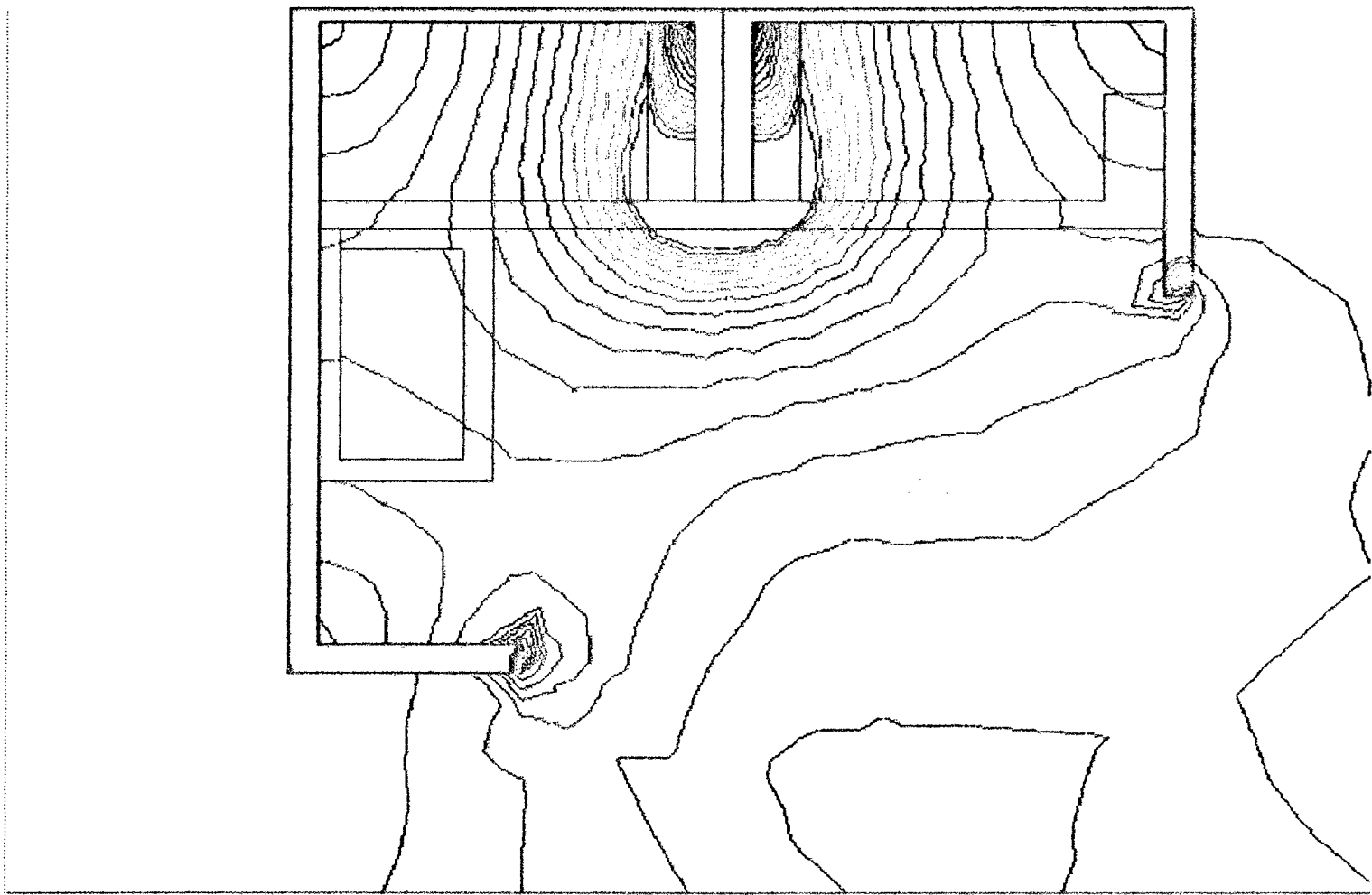
Fig. 4.11 Maximum Field Contours for the FIT-13
in Units of Tesla

Table 4.5   FIT-13 Grid Specifications

Parameter	Set 1	Set 2
d_a (mm)	2	2
d_S (mm)	2	2
p (mm)	4	3
lg (mm)	1	1
t_S (mm)	0.5	0.5
ta (mm)	0.5	0.5
N (number of holes)	829	1474
Pattern	Rectangular	Rectangular
Active Diameter (mm)	130	130
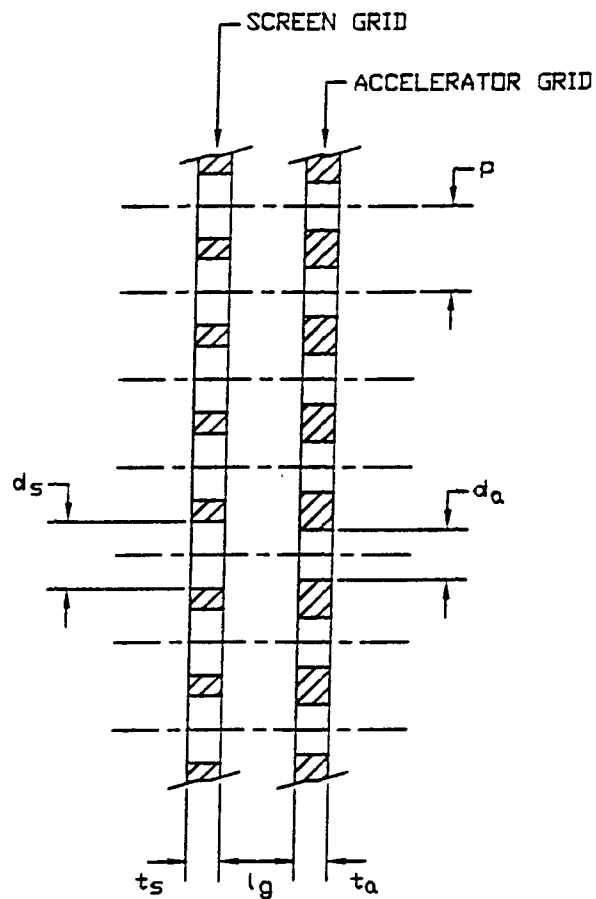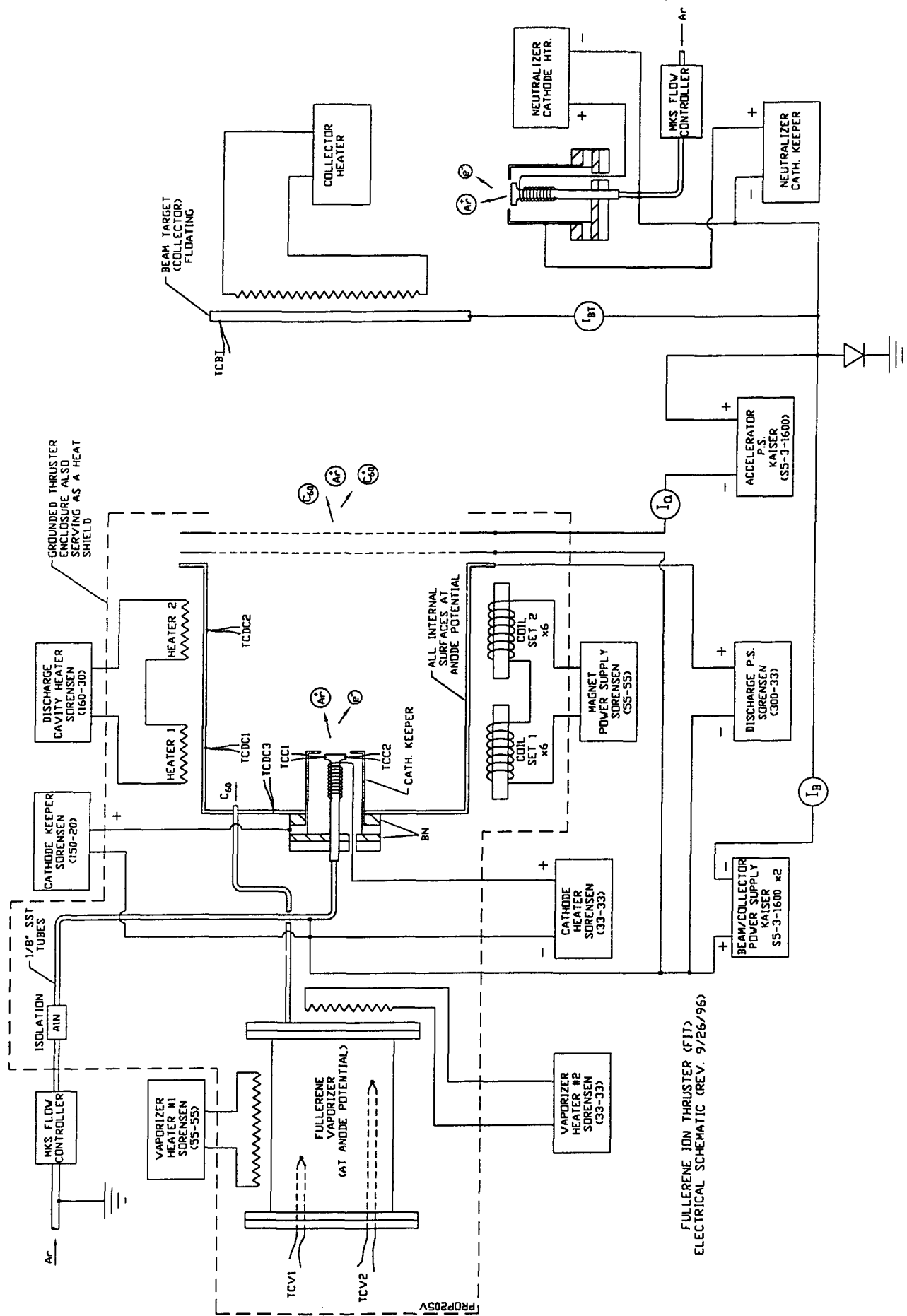
Fig. 4.12 Fullerene Ion Thruster Electrical Schematic

37

All power supplies are floating fed with separate isolation transformer. The entire system is remotely controlled from a PC style computer which also functions as the data acquisition system. Further description of this system is relegated to Section 6.

BUSEK

5.0 THRUSTER CONSTRUCTION AND DESIGN EVOLUTION

All machined components of the thruster system were fabricated by outside vendors per Busek drawings and assembled in-house. Photographs of the major components are shown in Figs. 5.1 through 5.3 showing the vaporization chamber, the back flange of the thruster and the discharge chamber, respectively. The vaporizer design and construction features were discussed in Section 4. A key aspect is internal temperature uniformity requirement achieved through the use of explosion bonded Cu and SST vaporizer walls. The back flange of the thruster (Fig. 5.2) is made of soft iron acting as a guide of the magnetic field flux. The flange also contains the fullerene distribution manifold made of SST. The photograph of the discharge chamber (Fig. 5.3) shows the mid and front magnetic flanges to form the internal cusp magnetic field structure. Also shown is a portion of the chamber wall heaters to prevent internal fullerene condensation and pivoting grid mounting system. The pivoting insulators made of SiN which allows free radial and azimuthal differential thermal expansion of both the chamber and the grids.

Photographs of the assembled thruster system are shown in Figs. 5.4 and 5.5. The connection between the vaporizer and the discharge chamber is revealed in Fig. 5.4 along with a portion of the hollow cathode mounted on a BN flange. The electromagnet coils creating the internal cusp field are visible in both Figs. 5.4 and 5.5, the later also shows the grid and the grid mounting system. The entire assembly is mounted on ceramic standoffs which in turn are mounted on a grounded skid with rails. The rails support grounded shroud (not shown) that encloses the entire assembly and acts as the outer most heat shield.

Following assembly, the magnetic field prediction (see Section 4) was verified using a Gauss meter and the traditional technique of flux mapping using iron filings. Figure 5.6 shows a photograph of the flux lines formed by iron filings on cardboard paper inserted into the discharge chamber. This photograph and measurements confirm predictions shown in Figs. 4.10 and 4.11.

Initial experiments revealed several difficulties with operating the thruster and led to the following design changes.

1) The external discharge chamber heater was replaced by heated sleeve that is inserted into the discharge chamber. The design of this sleeve is shown in Fig. 5.7. Heating is accomplished by coaxial swaged wire whose outer sheet is periodically tack welded to the sleeve.

2) The change in item 1 facilitated improved discharge chamber heating and permitted replacement of electromagnets Alnico 5, 1/2" dia. cylindrical permanent magnets that yielded approximately the same magnetic field.

3) The stainless steel conduits for fullerene vapor that connect the vaporizer and the discharge chamber were replaced with copper tubes of the same size to affect better temperature uniformity and prevent internal C_{60} vapor condensation.

4) Initially tested hollow cathode heater was later replaced by swaged tantalum cable.

5) Initially tested tungsten wire vaporizer heater was replaced by swaged tantalum cable.

The results reported in subsequent sections were obtained after implementation of the above discussed changes.
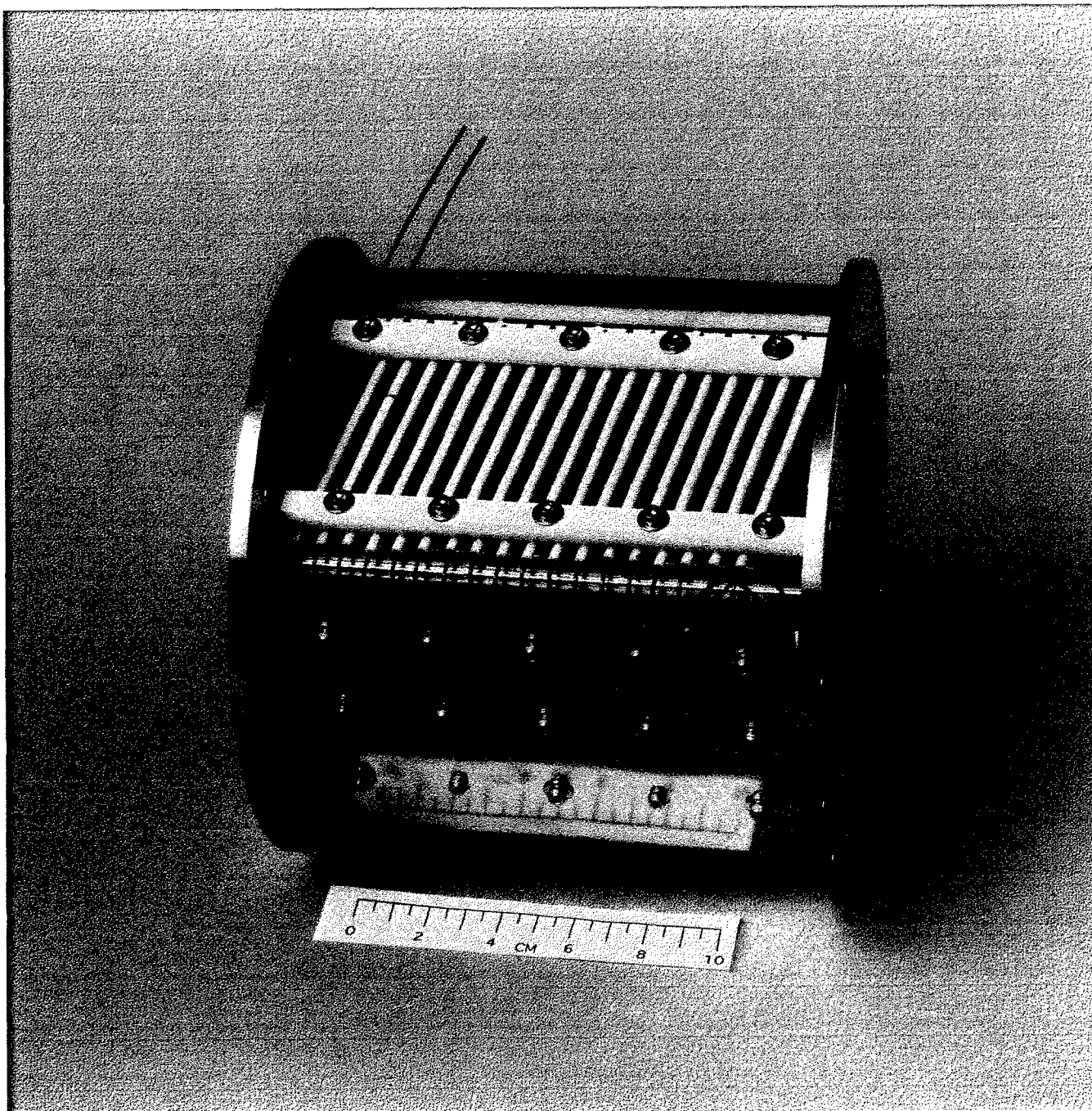
0261

Fig. 5.1 FIT-13 Vaporization chamber
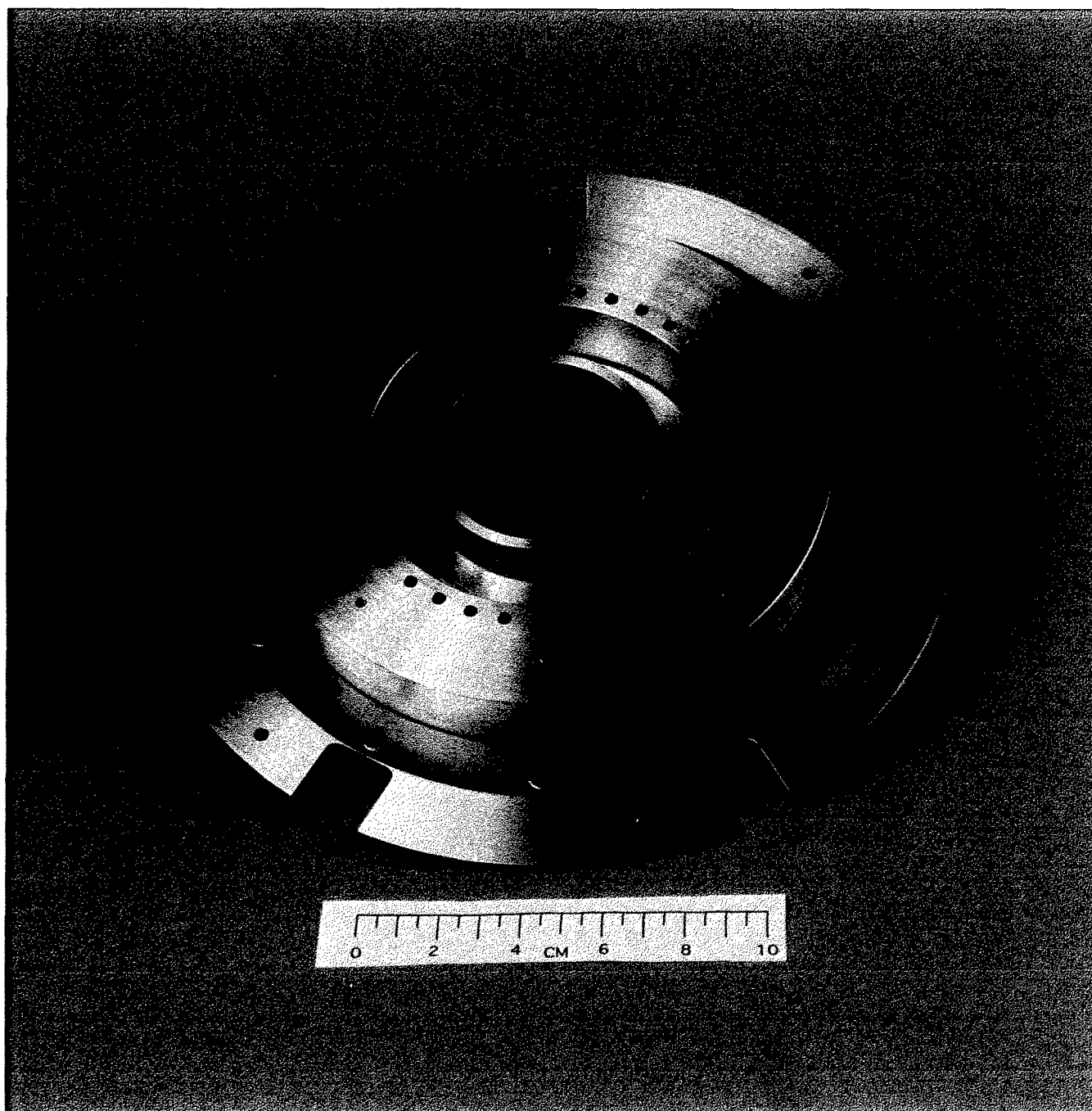
0262

Fig. 5.2 FIT-13 Back Flange with Fullerene Manifold

BUSEK
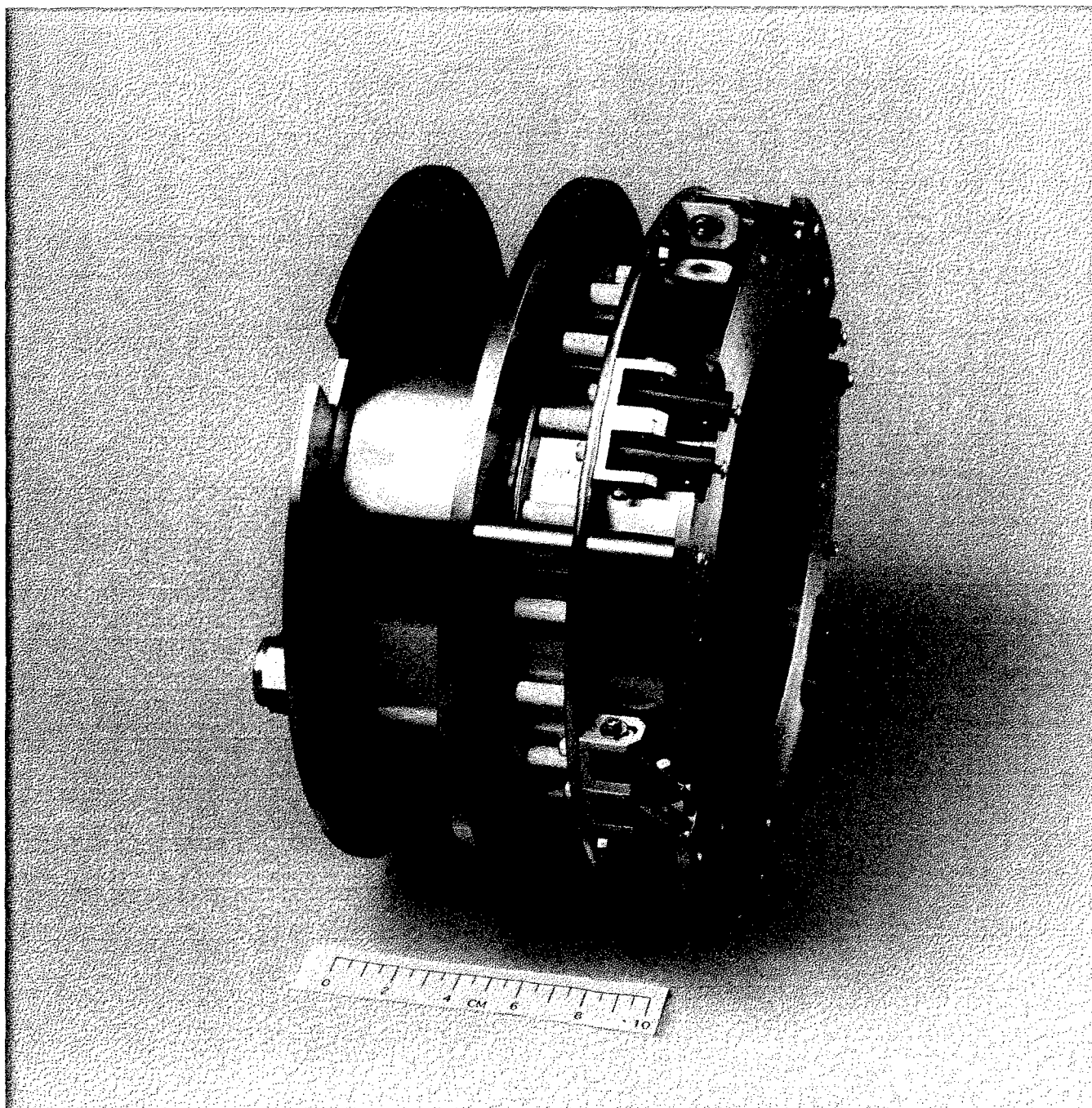
0263

Fig. 5.3   FIT-13 Discharge Chamber Showing Elements of the Magnetic Circuit,
Chamber Heater and Grid Mounting System

BUSEK
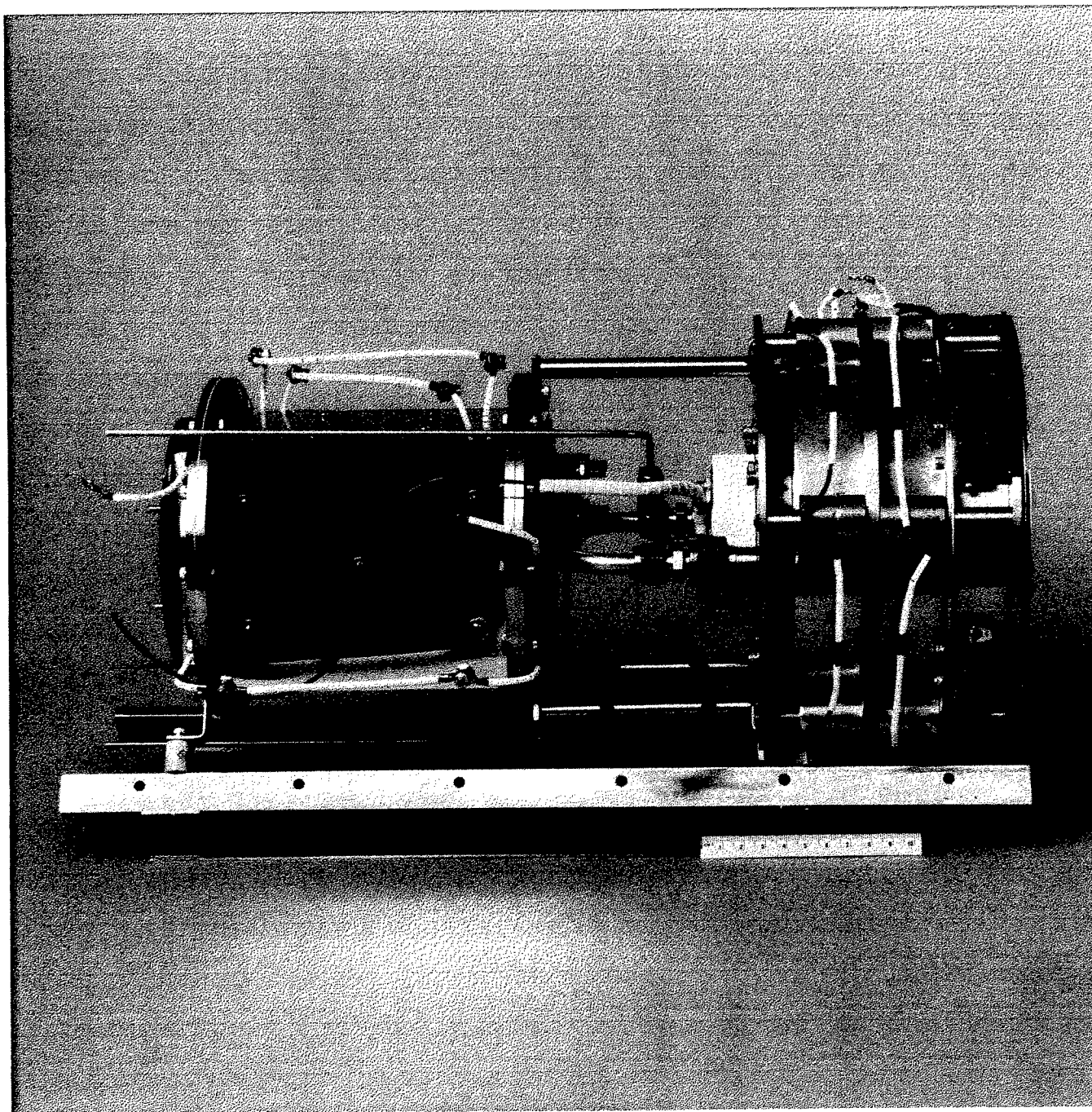
0267

Fig. 5.4　Side view of the FIT-13 thruster system showing C_{60} vaporization (left)
and the discharge chamber (right)

BUSEK
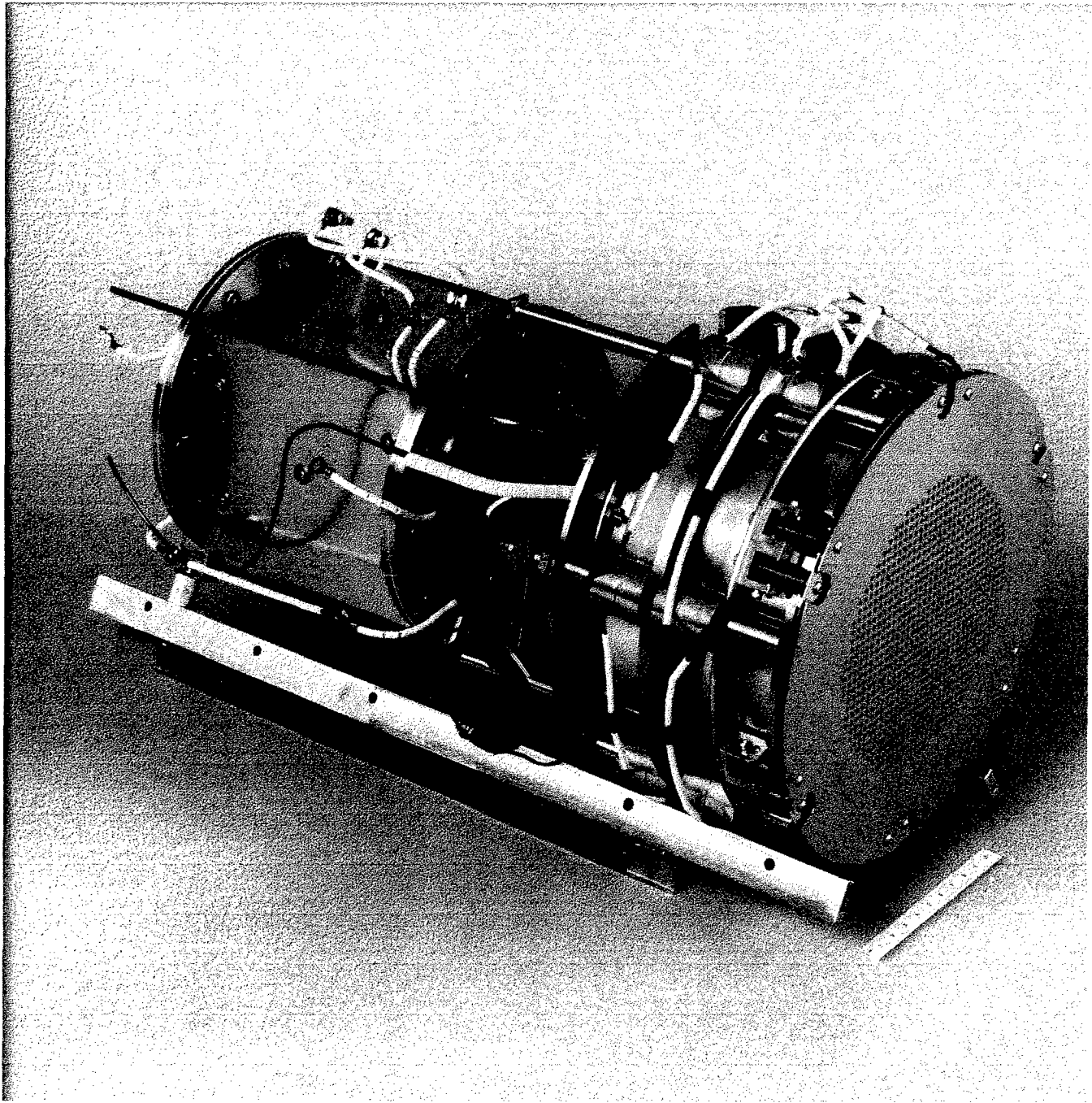
0265

Fig. 5.5 FIT-13 Thruster System Showing Vaporizer, Discharge Chamber
and Simple Mo Grids

44
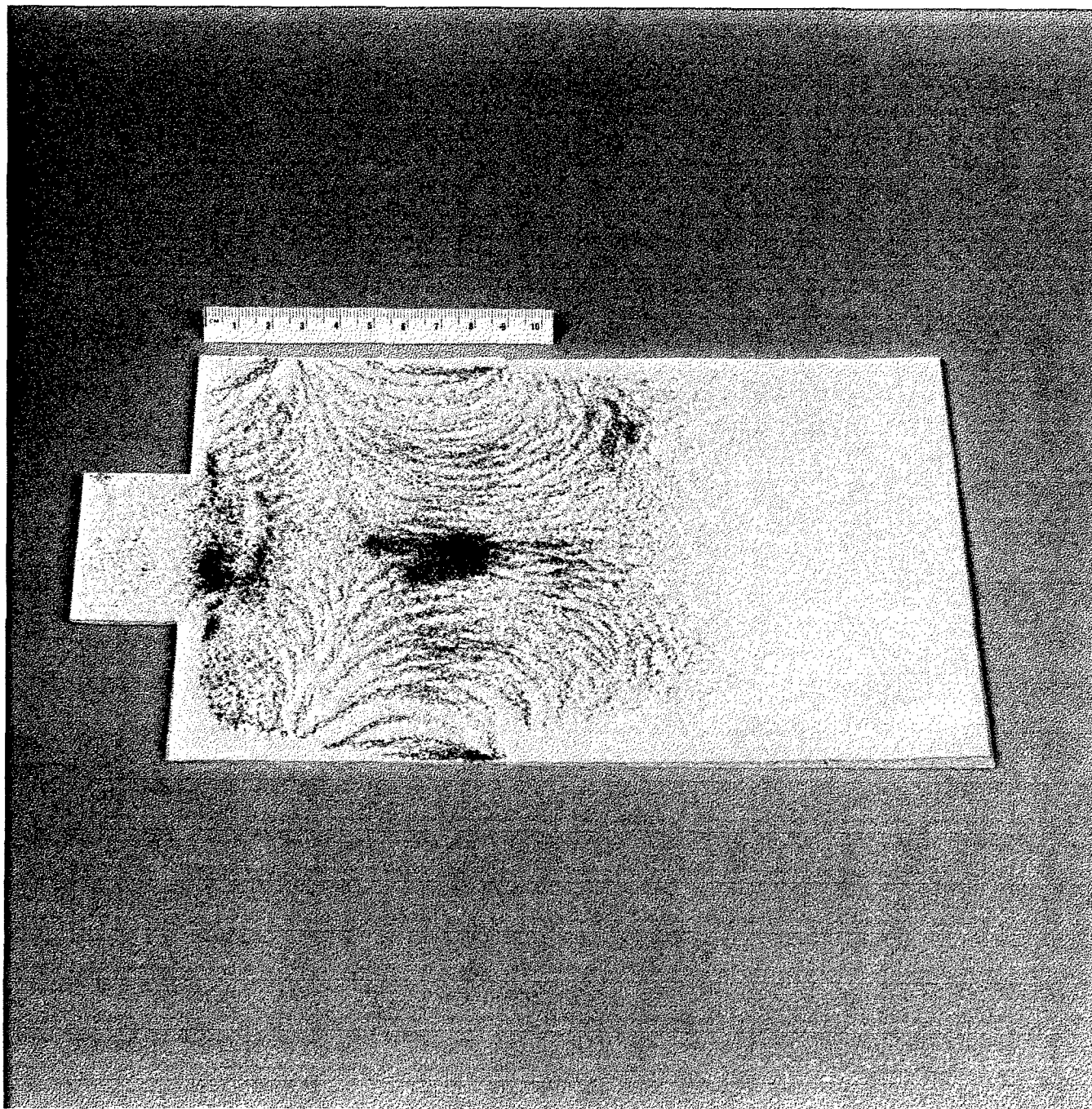
0266

Fig. 5.6 Iron Fillings Indicate Distribution of the Field Lines Inside the Discharge Chamber

BUSEK
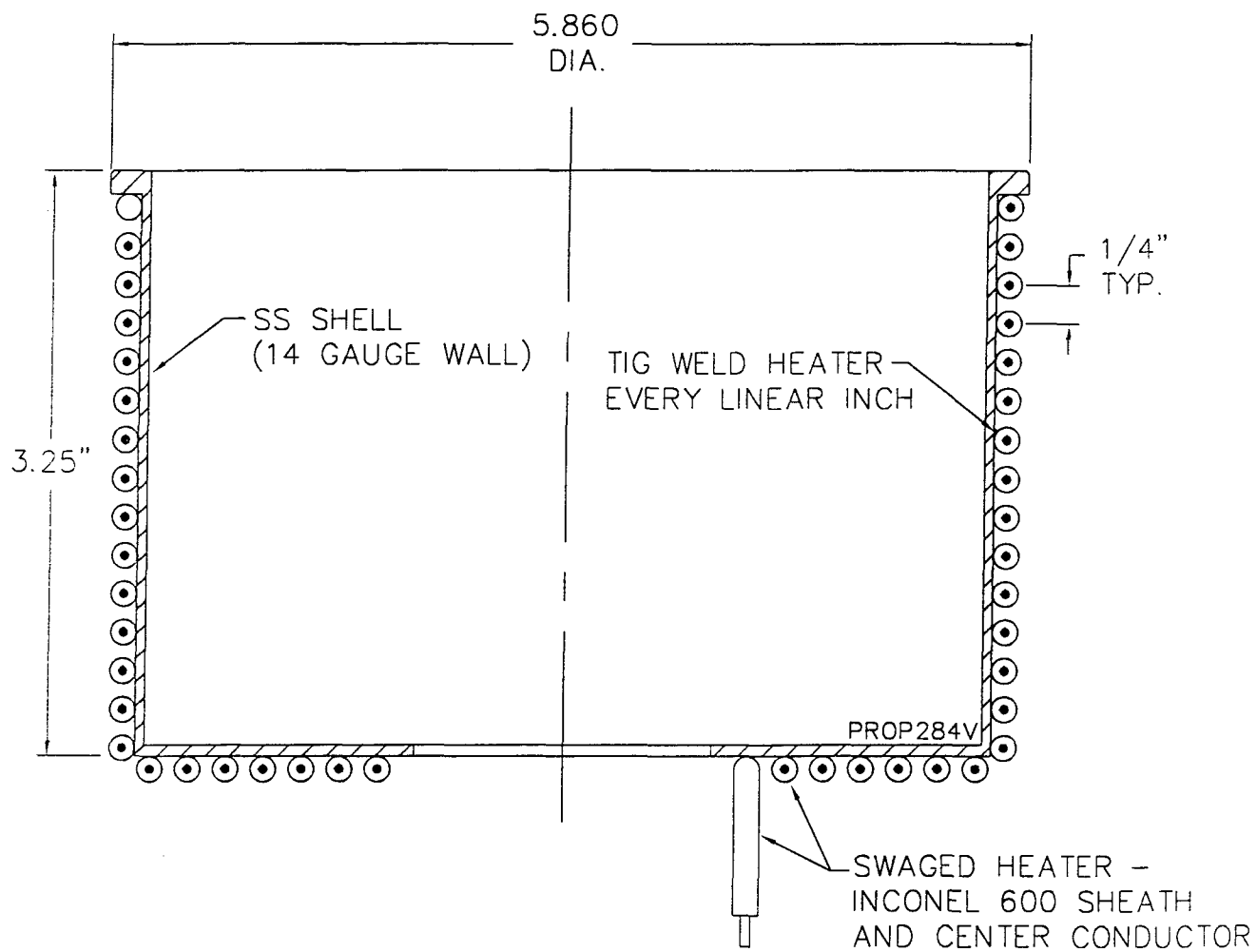
Fig. 5.7 Heated Insert/Liner for the Discharge Chamber

46

6.0   FACILITY

The vacuum tank is a cylindrical stainless steel vessel approximately 4 ft. in diameter and 5 ft. long with hinged doors on both ends of the cylinder and 3 flanged access ports each 24" dia. The tank is pumped with a 24" oil diffusion pump backed by 355 CFM two-stage system that consists of a blower and mechanical pump.

The thruster system is installed within a 20" dia. cylindrical side enclosure as shown in Fig. 6.1. The thruster system is mounted on a grounded bracket within this enclosure and electrically floats at the beam power supply potential. In order to prevent streaming of neutralizer electrons to the thruster system a grounded baffle is installed near the acceleration grid as indicated in Fig. 6.1. A commercial neutralizer cathode is operated on Ar as is the internal/discharge cathode when in use.

The electrical system consists of 9 dc power supplies, installed in 3 adjacent 24" instrumentation cabinets. Each power supply can float with respect to ground and can be connected to arbitrary potential in the system (see Fig. 4.11). Isolation rated to 3 kV is accomplished by feeding each power supply with an isolation transformer and mounting the power supply on fiberglass rails inside the grounded metallic cabinets. An overall photograph of the system is shown in Fig. 6.2.

Control of the power supplies and data acquisition is performed by a PC style computer. The interface between the floating high voltage system and the grounded computer consists of high voltage (3 and 4.5 kV) isolation amplifiers mounted on two different types of printed circuit boards. One type is used for straight isolation without amplification (Datatrak boards, 4.5 kV isolation) and the other type is used for thermocouple signals and has adjustable gain (KD Physics, 3 kV isolation). The system is controlled and data are stored using software called LabView made by National Instruments. Operator inputs his commands either via the PC keyboard or a mouse. Each power supply can also be controlled manually by using isolated control knob extension shafts to ensure operator safety. The manual control and manual data taking was often used instead of the computerized system because of frequent failures of the isolation amplifiers that shorted when the grids sparked.

BUSEK
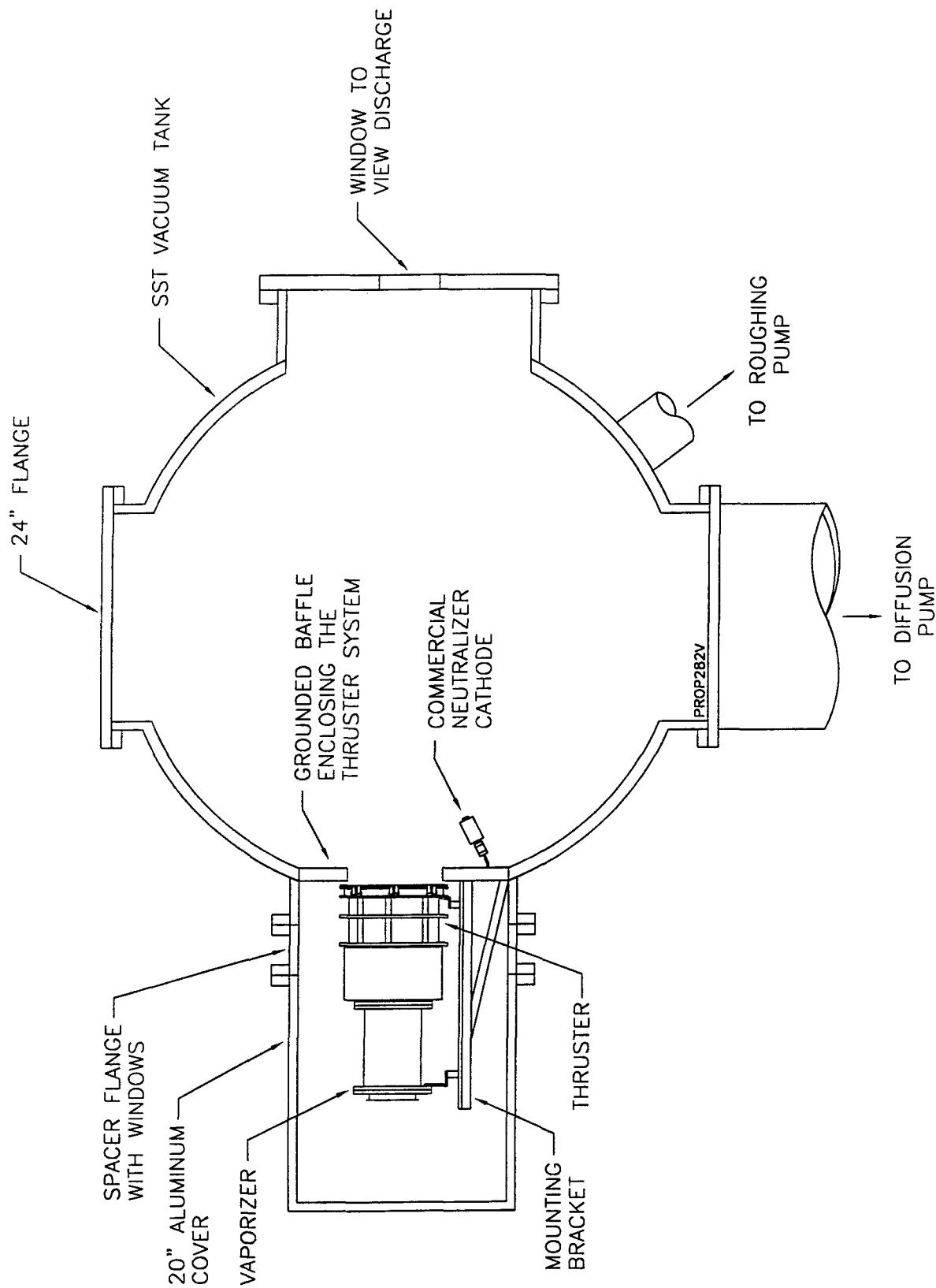
Fig. 6.1 Overall Vacuum System Schematic— C_{60} Fullerene Thruster Experiment
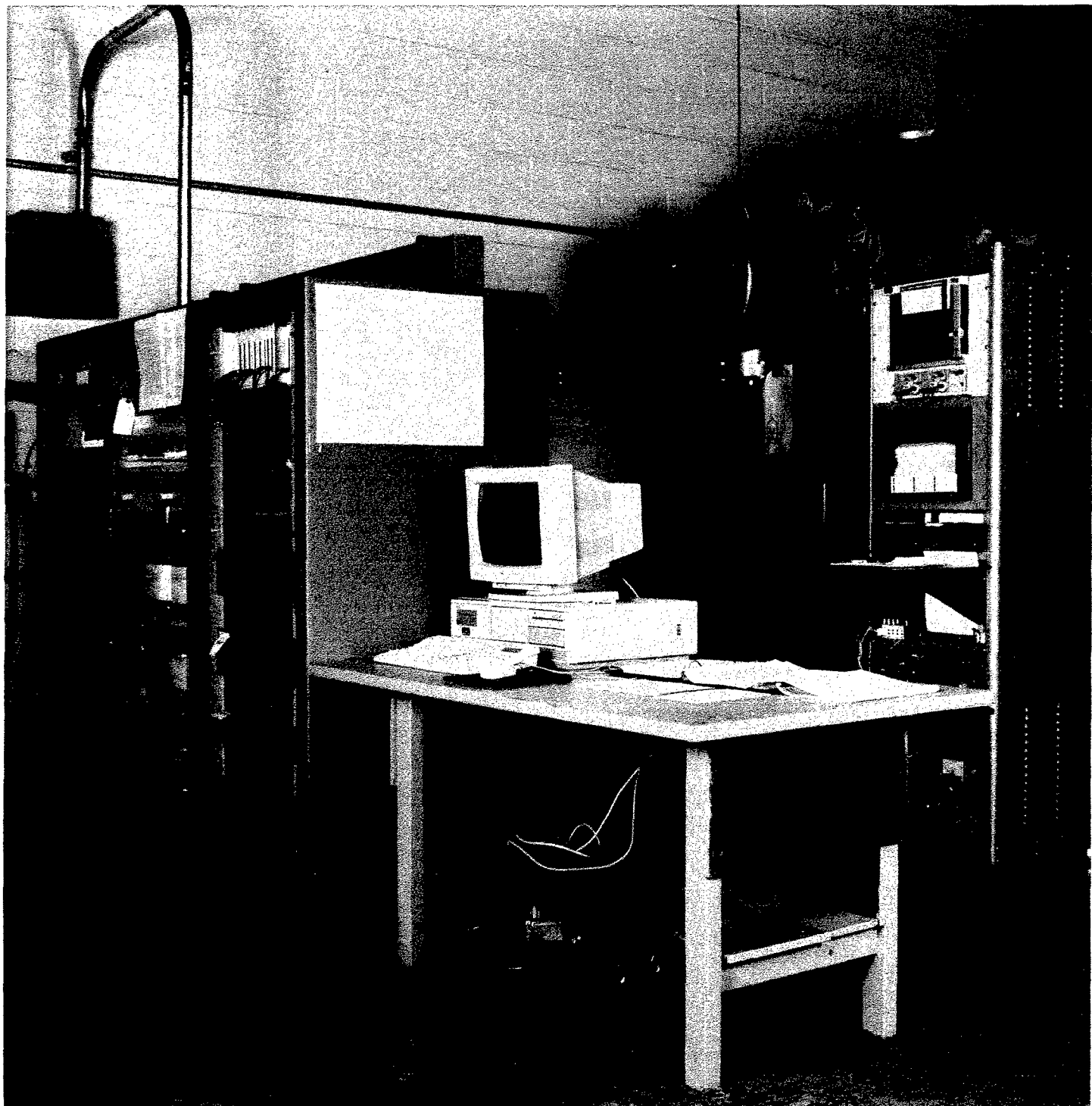
Fig. 6.2 Large Throughput Vacuum Facility

0251

7.0 EXPERIMETNAL RESULTS & DISCUSSION

7.1 Procedures

Fullerene propellant was prepared two different ways. The simpler preparation method involved simple vacuum drying of the as purchased sample while the more complex process involved sublimation of the as purchased sample, capture and condensation of the vapor. Only the condensate was then used as the propellant. The propellant typically consisted of C60/C70 mix with 80/20 split. The suppliers and preparation details were discussed in detail in Section 3.0.

Regardless of the preparation procedure the propellant was always weighed and placed into the thruster system vaporizer prior to the installation of the system in the vacuum chamber (see Section 6, Fig. 6.1). Typical propellant batch had 10 grams. Upon test completion the mass of the propellant remaining in the vaporizer was weighed were any remnants in the discharge chamber. Following thruster system installation into the test chamber, the chamber was pumped down to low $10^{-5}/10^{-6}$ torr level. Argon was then introduced into the discharge chamber via the hollow cathode. Following cathode insert heating the cathode was started using the keeper circuit followed by discharge initiation on the cathode Ar flow only. The Ar flow rate was generally kept to a minimum as dictated by the cathode operation. Ar beam was established by applying voltages to the screen and the acceleration grid. Typical screen voltage also referred to as the beam voltage was 1 kV (relative to ground) while the accelerator voltage was typically at -500 V. Beam neutralization was achieved using a commercially available cathode operated on argon.

Once the thruster system was operating on argon and the baseline Ar beam was established, the discharge chamber heating is applied followed by heating of the vaporizer. As the fullerene mass flow increased the beam gradually changed appearance from blue/purple to a light yellow which is a visual indication that the discharge operates on fullerenes. This is shown in Fig. 7.1 where the top photo shows the discharge operating on Ar (as viewed through the grids) and the bottom photo shows the discharge color when operating on fullerenes. The bright region in the center is the dense Ar plasma emanating from the hollow cathode.

Several tests were conducted with the Ar hollow cathode replaced by 2% Th heated tungsten filament. During these tests the procedure described above was slightly modified.

Several tests were also conducted with stainless steel sheet metal target exposed to the beam to explore carbon film deposition. The target was approximately 30 cm downstream from the grids and was always kept at zero potential (ground level). Results of such test are discussed in Section 8.4.

7.2 Representative Experimental Data

Typical data sheets that contain all measured quantities recorded as a function of time are shown in Tables 7.1 and 7.2. The tank pressure, cathode flow, keeper current and voltage, the neutralizer flow, keeper current and voltage, the discharge current and voltage, the potential of the grids, the accelerator current and the beam current were measured. Additionally the outputs of three thermocouples were recorded as were the voltages and currents of the vaporizer and discharge chamber heaters. The thermocouple labeled Tc1 is located on the front flange of the thruster just upstream of the grids (external to the discharge chamber) and is the coldest portion of the system. Thermocouple Tc4 is located on the vaporizer manifold between the vaporizer and the thruster and approximately corresponding to the temperature of the vapor conduits between the

BUSEK

(a)
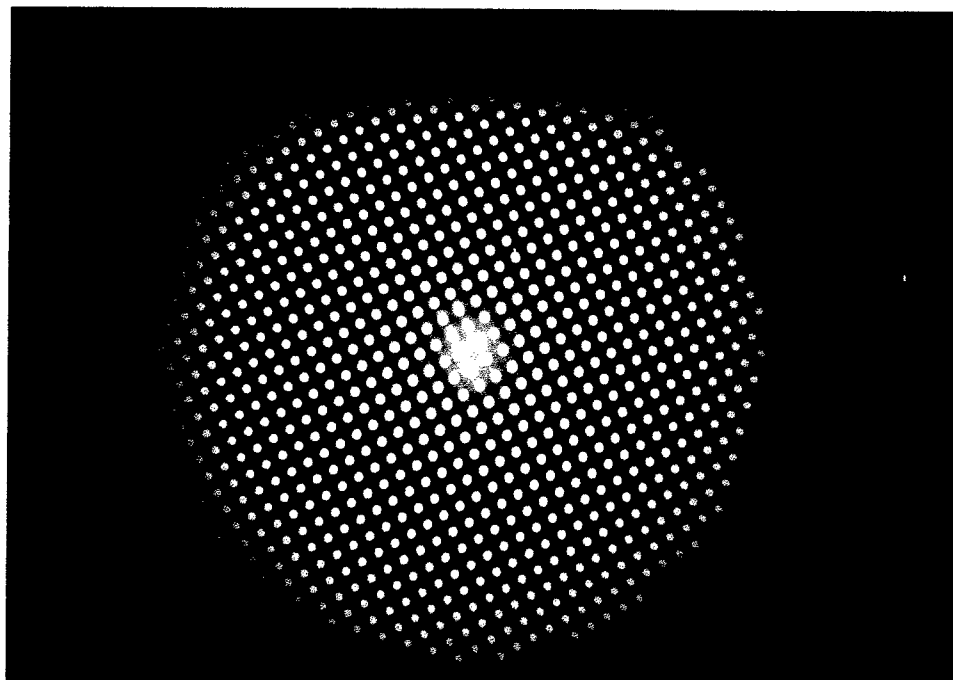
(b)

Fig. 7.1   Photo of the Discharge Through the Grids Showing (a) Argon Plasma Only
(b) Fullerene/Argon Plasma. The former is blue/purple, the latter is yellow.
The bright spot in the center is the dense Ar plasma emanating from the hollow
cathode

BUSEK

Test Conditions: 1) Load of 15.38g of Hoechst batch C60 (dried at 300deg C apx. 18 hours), 2) 4 Stainless Steel targets installed on the rotating "feed thru" rod Targets (1,2,3,4) will be rotated clockwise to be sputtered at diff beam currents
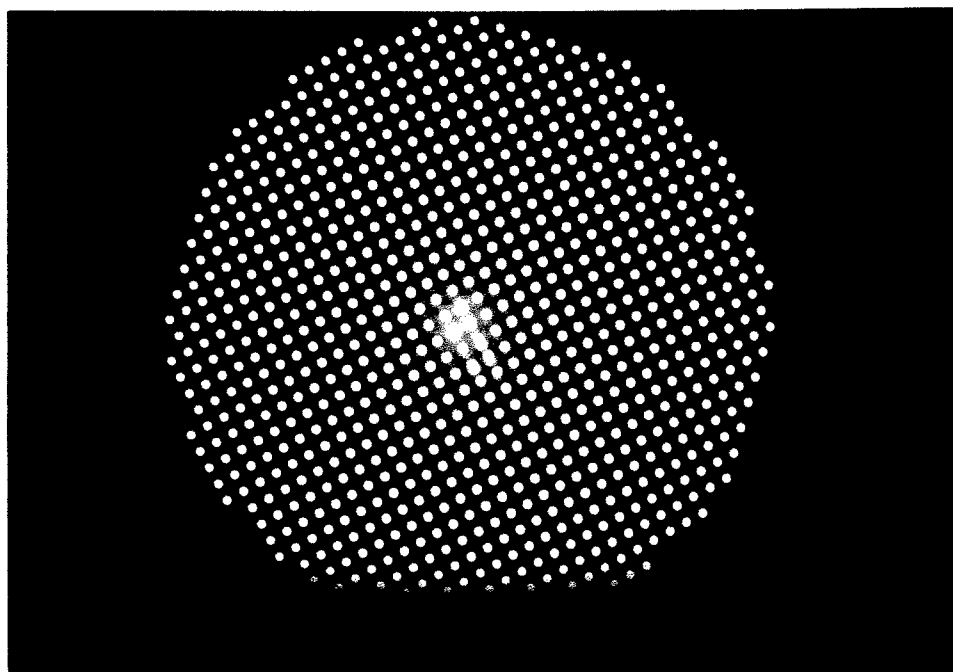(i.e. at following Beam Voltages 1,000V, 800V, 650V, 500V)

Time	p - Tank (x 10⁻) [Torr]	Hollow Cathode Ar Flow [cm³/min]	Hollow Cathode Keeper Current [A]	Hollow Cathode Keeper Voltage [V]	Neutralizer Ar Flow [cm³/min]	Neutralizer Keeper Current [A]	Neutralizer Keeper Voltage [V]	Discharge Chamber Discharge Current [A]	Discharge Chamber Discharge Voltage [V]	Discharge Chamber Heater Current [A]	Discharge Chamber Heater Voltage [V]	Beam Current [mA]	Beam Voltage [kV]	Accelerator Current [mA]	Accelerator Voltage [kV]	Vaporizer Htr #1 Current [A]	Vaporizer Htr #1 Voltage [V]	Vaporizer Htr #2 Current [A]	Vaporizer Htr #2 Voltage [V]	TC1 Fr. Flange [deg C]	TC4 Manifold [deg C]	TC6 Vaporizer [deg C]
10:15	0.8	3	0.5	15.1	3	0.3	55	1.0	43.0	9.5	58	12.4	1.00	0.62	0.5	0	0.0	0	0.0	195	42	32
10:42	0.8	2.5	0.5	15.6	3	0.3	50	1.0	46.5	9.5	57	11.4	1.00	0.58	0.5	0	0.0	0	0.0	342	72	39
10:58	0.7	2.5	0.5	13.3	3	0.3	53	1.5	53.1	9.5	57	14.1	1.00	0.96	0.5	0	0.0	0	0.0	388	98	50
11:25	0.7	2.5	0.5	16.0	3	0.3	56	1.5	53.3	9.5	57	13.4	1.00	1.01	0.5	14	5.2	18	18.8	421	136	75
11:37	0.8	2.5	0.5	16.2	3	0.3	57	1.0	46.1	9.0	55	10.6	1.00	0.70	0.5	14	10.3	18	25.4	421	212	137
11:52	1.2	2.5	0.5	16.1	3	0.3	57	1.0	45.1	9.0	54	10.9	1.00	0.74	0.5	14	11.4	20	34.2	418	322	265
12:02	0.9	2.5	0.5	16.4	3	0.3	57	1.0	44.6	9.0	54	12.7	1.00	0.70	0.5	14	11.9	22	35.7	418	413	381
12:12	1.0	2.5	0.5	18.3	3	0.3	58	1.0	44.4	9.0	54	13.0	1.00	0.73	0.5	14	12.1	22	42.2	421	479	420
12:16	1.0	2.5	0.5	16.9	3	0.3	60	0.7	43.2	9.0	54	10.3	1.00	0.65	0.5	14	12.0	22	42.4	421	524	480
12:25	2.0	2.5	0.5	17.0	3	0.3	61	0.7	39.7	9.0	55	10.6	1.00	0.64	0.5	14	12.4	22	42.4	424	542	530
12:28	2.8	2.5	0.5	16.9	3	0.3	61	0.7	39.4	9.0	55	10.7	1.00	0.67	0.5	14	12.5	22	42.3	427	554	545
12:33	2.5	2.5	0.5	17.0	3	0.3	61	0.7	38.9	9.0	55	10.5	1.00	0.70	0.5	14	12.6	22	42.3	430	565	566
12:38	2.7	2.5	0.5	16.8	3	0.3	61	0.7	41.4	9.0	56	11.7	1.00	0.78	0.5	14	12.7	22	42.3	434	576	575
12:43	3.0	2.5	0.5	16.3	3	0.3	61	0.7	40.6	9.0	56	11.4	1.00	0.73	0.5	14	12.7	22	42.3	437	583	580
12:47	3.0	2.5	0.5	16.0	3	0.3	61	0.7	39.6	9.0	56	10.8	1.00	0.68	0.5	14	12.8	22	42.3	440	589	590
12:52	2.5	2.5	0.5	16.1	3	0.3	61	0.7	40.3	9.0	56	10.3	1.00	0.67	0.5	14	12.9	22	42.3	444	595	602
12:59	2.8	2.5	0.5	16.2	3	0.3	61	0.7	41.3	9.0	56	9.9	1.00	0.68	0.5	15	14.2	22	42.3	447	601	619
13:02	2.5	2.5	0.5	16.4	3	0.3	61	0.7	41.6	9.0	56	9.5	1.00	0.68	0.5	15	14.3	22	42.3	449	604	625
13:13	3.0	2.5	0.5	16.5	3	0.3	61	0.7	41.6	9.0	56	8.3	1.00	0.72	0.5	15	14.3	22	42.3	451	608	629
13:15	2.8	2.5	0.5	16.5	3	0.3	61	0.7	41.3	9.0	56	8.6	1.00	0.75	0.5	15	14.3	22	42.3	455	612	639
13:22	2.5	2.5	0.5	16.6	3	0.3	61	0.7	41.0	9.0	56	7.5	0.80	0.67	0.5	15	14.3	22	42.3	456	613	654
13:33	2.5	2.5	0.5	16.6	3	0.3	61	0.7	40.4	9.0	56	6.7	0.80	0.73	0.5	15	14.4	22	42.3	458	615	659
13:38	2.5	2.5	0.5	16.5	3	0.3	61	0.7	40.3	9.0	56	6.8	0.65	0.65	0.5	15	14.4	22	42.3	459	616	667
13:48	1.2	2.5	0.5	16.5	3	0.3	61	0.7	39.9	9.0	56	6.4	0.65	0.68	0.5	15	14.4	22	42.2	460	617	671
13:53	1.2	2.5	0.5	16.5	3	0.3	61	0.7	39.8	9.0	56	6.3	0.65	0.61	0.5	15	14.4	22	42.2	460	617	673
13:57	1.0	2.5	0.5	16.5	3	0.3	61	0.7	39.7	9.0	56	6.2	0.50	0.61	0.5	15	14.4	22	42.2	461	617	676
14:05	1.0	2.5	0.5	16.5	3	0.3	61	0.7	39.6	9.0	56	6.1	0.50	0.61	0.5	15	14.4	22	42.1	461	617	678
14:25	0.9	3	0.0	0.0	3	0.3	60	0.0	0.0	9.0	56	0.0	0.00	0.00	0.0	0	0.0	0	0.0	458	560	655
15:07	0.7	3	0.0	0.0	3	0.0	0	0.0	0.0	0.0	0	0.0	0.00	0.00	0.0	0	0.0	0	0.0	430	286	420
15:22	0.8	3	0.0	0.0	3	0.0	0	0.0	0.0	0.0	0	0.0	0.00	0.00	0.0	0	0.0	0	0.0	347	262	350
15:55	0.3	0	0.0	0.0	0	0.0	0	0.0	0.0	0.0	0	0.0	0.00	0.00	0.0	0	0.0	0	0.0	247	184	270
17:05	50.0	0	0.0	0.0	0	0.0	0	0.0	0.0	0.0	0	0.0	0.00	0.00	0.0	0	0.0	0	0.0	159	122	250

6.98g of C60 left in the vaporizer - 8.4g vaporized.

Average intergrid distance l_g [m]:	1.91E-03

Table 7.1 Representative Data Sheet Containing all Measured Quantities as a Function of Time

C60 ION THRUSTER RUN (6/17/96)

Few unsuccessfull runs attempted before this one

Test Conditions: 1) Intergrid distance increased to 0.133" 2) Disch Cavity Heater Polarity Changed, 3) 10g of new Hoechst batch C60 loaded on 6/6/96

Time	p Tank ($\times10^{-5}$) [Torr]	Hollow Cathode Ar Flow [cm³/min]	Hollow Cathode Keeper Current [A]	Hollow Cathode Keeper Voltage [V]	Neutralizer Ar Flow [cm³/min]	Neutralizer Keeper Current [A]	Neutralizer Keeper Voltage [V]	Discharge Current [A]	Discharge Voltage [V]	Heater Current [A]	Heater Voltage [V]	Beam Current [mA]	Beam Voltage [kV]	Accelerator Current [mA]	Accelerator Voltage [kV]	Vaporizer Htr #1 Current [A]	Vaporizer Htr #1 Voltage [V]	Vaporizer Htr #2 Current [A]	Vaporizer Htr #2 Voltage [V]	TC1 Fr Flange [deg C]	TC4 Manifold [deg C]	TC6 Vaporizer [deg C]
9:55	1.9	5	0.5	13.3	3	0.3	33	1.5	34.0	9	55	30.7	1.0	1.16	0.50	0.0	0.0	0.0	0.0	413	160	106
10:12	2.0	5	0.5	13.1	3	0.3	34	1.5	33.5	9	55	30.3	1.0	1.22	0.50	14.0	11.0	18.0	28.0	418	288	226
10:32	2.0	5	0.5	12.9	3	0.3	34	1.5	32.9	9	55	29.4	1.0	1.22	0.50	15.0	13.2	20.0	35.3	434	494	494
10:57	2.5	5	0.5	12.8	3	0.3	34	1.5	33.3	9	56	27.8	1.0	1.27	0.50	15.0	13.7	20.0	35.7	439	518	530
11:02	3.0	4	0.5	13.3	3	0.3	35	1.5	38.4	9	56	31.7	1.0	1.48	0.50	15.0	13.2	20.0	35.8	441	540	561
11:10	6.5	4	0.5	13.5	3	0.3	36	1.5	37.7	9	56	31.2	1.0	2.35	0.50	14.0	12.1	20.0	36.2	449	568	593
11:16	30.0	4	0.5	14.1	3	0.3	34	1.5	34.4	9	56	30.4	1.0	3.78	0.50	14.0	11.9	21.0	39.1	451	572	602
11:21																						
11:37	5.0	5	0.7	13.7	3	0.3	33	1.5	32.5	9	55	29.7	1.0	1.73	0.50	12.0	9.8	22.0	41.8	445	498	620
11:57	5.0	5	0.7	13.4	3	0.3	31	1.5	33.6	9	55	28.1	1.0	1.74	0.50	12.0	9.1	22.0	42.0	453	571	580
12:07	7.0	5	0.7	13.6	3	0.3	30	1.5	33.0	9	56	26.5	1.0	2.17	0.50	13.0	9.5	22.0	42.1	456	587	620
12:16	9.0	5	0.7	13.8	3	0.3	31	1.5	32.6	9	56	24.8	1.0	3.93	0.50	14.0	9.7	22.0	42.1	458	595	620
12:28	30.0	4	0.7	14.3	3	0.3	32	1.5	36.6	9	56	29.1	1.0	3.11	0.50	14.0	9.7	22.0	42.1	460	601	620
12:43	7.0	4	0.7	14.1	3	0.3	30	1.5	35.8	9	56	25.9	1.0	2.16	0.50	14.0	9.7	22.0	42.2	426	609	630
13:10	6.0	4	0.7	14.3	3	0.3	29	1.5	35.5	9	56	23.1	1.0	1.58	0.50	14.0	9.7	22.0	42.1	429	613	630
13:25	5.0	3.5	0.7	14.4	3	0.3	30	1.5	38.2	9	56	25.7	1.0	1.59	0.50	14.0	9.7	22.0	42.0	431	613	650
13:36	4.0	3	0.7	14.9	3	0.3	30	1.5	40.4	9	56	27.4	1.0	1.60	0.50	14.0	9.8	22.0	42.0	431	613	650
13:42	4.0	3	0.7	15.2	3	0.3	30	1.5	40.6	9	56	27.5	1.0	1.55	0.50	14.0	9.8	22.0	41.9	431	613	665
14:00	3.0	3	0.7	15.1	3	0.3	30	1.5	40.6	9	56	27.2	1.0	1.49	0.50	14.0	9.8	22.0	41.8	431	612	665
14:28	2.5	2.5	0.7	14.9	3	0.3	28	1.5	40.4	9	56	26.9	1.0	1.42	0.50	14.0	9.8	22.0	41.6	431	612	665
14:33	2.3	2	0.7	15.7	3	0.3	28	1.5	41.4	9	56	27.2	1.0	1.42	0.50	14.0	9.8	22.0	41.5	431	612	665
14:39	2.3	2	0.7	16.7	3	0.3	28	1.5	47.4	9	56	30.2	1.0	1.45	0.50	14.0	9.8	22.0	41.5	428	611	670
14:45	2.0	2	0.7		3	0.3		1.5		9	56		1.0		0.50	14.0	9.8	22.0	41.4			670
14:58	2.0	2	0.7	21.9	3	0.3	27	0.7	36.5	9	55	8.3	1.0	0.87	0.50	14.0	9.7	22.0	41.3	423	611	670
15:10	1.9	2	0.7	22.0	3	0.3	29	0.7	37.0	9	55	8.6	1.0	0.87	0.50	14.0	9.7	22.0	41.3	423	610	670
15:15	1.9	2	0.7	22.1	3	0.3	29	0.7	37.3	9	55	8.8	1.0	0.88	0.50	14.0	9.7	22.0	41.2	426	610	670
15:21	1.8	1.5	0.7	21.7	3	0.3	28	0.7	37.6	8.5	50	8.9	1.0	0.93	0.50	0.0	0.0	0.0	0.0	418	609	670
15:30	1.8	1.5	0.7	22.6	3	0.3	29	0.7	45.9	NA	NA	11.1	1.0	0.93	0.50	0.0	0.0	0.0	0.0	440	609	670
15:42	1.5	1.5	0.7	22.1	3	0.3	29	0.7	48.5	9	54	12.7	1.0	0.99	0.50	0.0	0.0	0.0	0.0	440	523	640
15:51	1.2	1.5	0.7	23.5	3	0.3	28	0.7	48.9	9	54	16.3	1.0	0.97	0.50	0.0	0.0	0.0	0.0		483	590
16:15	1.0	1.5	0.7	23.8	3	0.3		0.7	50.0	9		15.9	1.0		0.50	0.0	0.0	0.0	0.0			540
16:22	1.0	1.5	0.7	24.5	3	0.3	35	0.7	47.7	0	0	4.3	1.0	0.61	0.50	0.0	0.0	0.0	0.0	327	396	420

Experiment shut down

Only 0.14 grams of C60 left in the vaporizer - 9.86g vaporized

Average intergrid distance l_g [m]: 1.91E-03

Table 7.2   Representative Data Sheet

53

vaporizer and the thruster. The thermocouple Tc6 is on the inside of the vaporizer. Tc6 was used to calculate the fullerene vapor pressure (not measured directly) and consequently the mass flow through the propellant orifice (see Fig. 4.1 for orifice location). Flow through the orifice lowered the vapor pressure and Tc4 was maintained at or above condensation temperature at that pressure. Tc1 was maintained at or above the fullerene condensation temperature that corresponds to the anticipated fullerene vapor pressure in the discharge chamber.

7.3 Typical Post Test Observations

The walls of the discharge chamber following a typical test were covered with thin, hard carbon film. This film adhered well to the walls until after several tests it accumulated to measurable thickness (~0.1 mm or less) at which point it formed poorly adhering flakes that could be scraped off with a hard object. The flakes were insoluble in benzene and appeared to be consistent with diamond-like carbon (DLC). There was no film in the locations of highest magnetic flux where the discharge current electrons are likely to strike the chamber walls (anode). The film free areas were bear metal bands around the circumference of the discharge chamber about 6 mm wide in the locations of the external magnetic flanges.

The upstream side of the screen grid was coated with extremely hard carbon film which could be removed with difficulty only by vigorous sanding. The film appeared to be hardest and best adhering in the center of the screen grid covering an area about 30 to 40 mm in diameter. Wetting the film with benzene did not dissolve it. It also appeared as a DLC film although no quantitative analysis were performed.

This observation is consistent with DLC film deposition by Gruen[23] who used argon/fullerene plasma created by microwave discharge.

The upstream side of the acceleration grid was coated with thin brownish film primarily in the areas where the screen and accelerator grid misaligned due to their differential expansion (see Fig. 7.1). This film was soft and could be wiped off.

For tests utilizing the hollow cathode, there was no significant carbon debris in the chamber however, after test with the filament cathode (both with and without Ar) there was copious amount of carbon in the chamber approaching the total vaporized fullerene mass. This is consistent with the Anderson's, et al[7] results who reported up to 2/3 of the vaporized fullerenes remaining in the discharge chamber as fullerene fragments when using filament cathode.

BUSEK

8.0 DATA ANALYSIS & DISCUSSION

The equations used to reduce the experimental data are summarized in Table 8.1. All of these equations are straightforward, conventional, relationships that require no explanations except for two aspects related to the estimation of the average intergrid gap and the appropriate ion mass that is required for evaluation of the space charge limited beam current density and thrust. These two issues are discussed next followed by the presentation of the experimental results.

8.1 Average Intergrid Gap

The intergrid separation, is not precisely known due to thermal distortion of the grids. For the test in Table 7.1 the intergrid distance was estimated to be 1.91 mm (see bottom right corner of the table). As indicated in Section 4, the grids, due to high cost of dished grids, were flat 0.5 mm thick Molybdenum and allowed to grow radially on pivoted insulators. Because the screen grid is at higher temperature than the accelerator (outer) grid it bows outward more than the accelerator grid as schematically indicated in Fig. 8.1.

During our initial tests, the cold state intergrid distance was set to 2 mm which always resulted in grid electrical shorting while approaching the operating temperature. This led us to increase the cold separation to between 2.70 to 3.38 mm. At 2.7 mm the grids still occasionally shorted so that the minimum hot condition intergrid gap at the center was estimated to be 3.38 - 2.70 = 0.62 mm. The average gap shown in Tables 7.1 and 7.2 was then estimated using the following weighted average gap relationship

$$\ell_{gave} = \frac{0.9\left(\ell_{g\,cold} + \ell_{g\,center\,hot}\right)}{2}$$

8.2 Beam Ion Mass

The space charge limited beam current density (J_{BCL}, Eq. 18 in Table 8.1) and the thrust (T, Eq. 20 in Table 8.1) depend on ion mass (m_i). When the discharge operates on a mixture of Ar, C_{60} and C_{70} it is not immediately evident which ion species will dominate the beam. To simplify the data reduction we discuss the limiting cases, i.e., when the beam consists of argon ions and when it consists of predominantly fullerene ions.

Before the vaporizer is heated to above (~400°C) the C_{60} + C_{70} vapor flow is negligible and the discharge operates on Ar (supplied via the hollow cathode or in the case of filament cathode via an adjacent port). Thus in this case the appropriate m_i is that corresponding to Ar ($m_{iAr} = 6.63 \times 10^{-26}$ kg). When the vaporizer is delivering mass flow of fullerenes ($\dot{m}_f$) that is comparable or greater than the flow of argon mass flow ($\dot{m}_{Ar}$), the ion number density of each species in the discharge chamber and the beam composition is dominated by fullerene ions. This is supported by the following analysis.

Consider the classical experiments carried by Rapp, et al.,[24] where they measure the total ionization cross-sections (Q) by measuring electron beam current (I_e) that intersects a molecular (or atomic) beam and produces an ion beam (I_i). The cross-section is then computed as

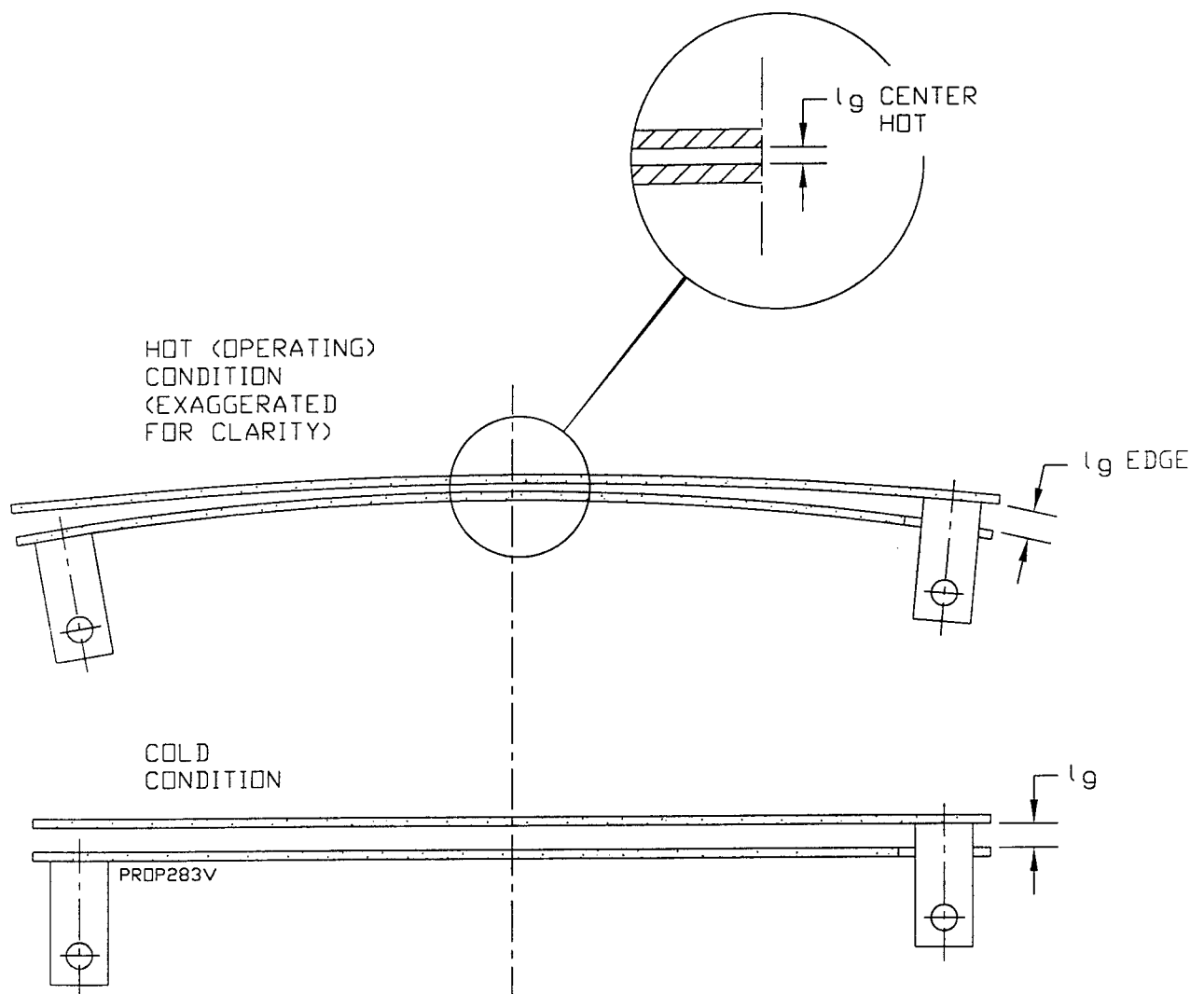**BUSEK**

Fig. 8.1 Schematic of the Thermal Distortion of the Grids

BUSEK

TABLE 8.1

EQUATIONS USED FOR DATA REDUCTION

	Quantity	Equation	Notes
1.	Partial Pressure of C_{60} or C_{70} (N/m²) in the vaporizer	$p = p_R e^{-\Delta Hs/RT}$	R = universal gas constant, T = measured vaporizer temperature
2.	Reference Pressure C_{60} (N/m²)	$p_{RC60} = 5.368 \times 10^9$	
3.	Reference pressure C_{70} (N/m²)	$p_{Rc70} = 1.879 \times 10^{11}$	
4.	Sublimation Enthalpy C_{60} (cal/mole)	$\Delta Hs_{C60} = 38,000$	
5.	Sublimation Enthalpy C_{70} (cal/mole)	$\Delta Hs_{C70} = 45,000$	
6.	Total Fullerene Pressure (C_{60} + C_{70})	$p_{ttl} = p_{C60} + p_{C70}$	
7.	Propellant Mass Flow (kg/sec)	$\dot{m}_f = P_{ttl} A \sqrt{\dfrac{\langle M_w \rangle}{2\pi RT}}$	A = vaporizer orifice flow area
8.	Average Molecular Weight (kg/kmole)	$\langle M_w \rangle = 720 \dfrac{P_{C60}}{P_{ttl}} + 840 \dfrac{P_{C70}}{P_{ttl}}$	
9.	Average Mass of Fullerene Ion or Molecule (kg)	$\langle m_i \rangle = \dfrac{\langle M_w \rangle}{6.02 \times 10^{26}}$	
10.	Total Mass Flow (kg/sec)	$\dot{m}_{ttl} = \dot{m}_f + \dot{m}_{Ar}$	
11.	Discharge Power (Watts)	$P_{dis} = I_{dis} V_{dis}$	Idis and Vdis are measured discharge current and voltage

TABLE 8.1 (CON'T)

	Quantity	Equation	Notes
12.	Beam Power (Watts)	$P_B = I_B V_B$	I_B = measured ion beam current, V_B = net, acceleration voltage = $|V_{screen}| - |V_{acc}|$
13.	Total Power (Watts)	$P_t = I_B V_B + P_{dis}$	
14.	Beam Ion Energy Cost (Volts)	$\varepsilon_B = \dfrac{P_{dis}}{I_B}$	
15.	Propellant Utilization Efficiency (-)	$\eta_{lu} = \dfrac{I_B \langle m_i \rangle}{q_e \dot{m}_{ttl}}$	q_e is elementary charge, assumes single ionization
16.	Electrical Efficiency (-)	$\eta_e = \dfrac{P_{dis}}{P_t}$	
17.	Overall Thruster Efficiency	$\eta_t = \eta_u \eta_e$	
18.	Theoretical Space Charge Limited Beam Current Density (A/m²)	$J_{BCL} = \dfrac{4\sqrt{2}}{9}\varepsilon_o \left(\dfrac{q_e}{m_i}\right)^{1/2}\dfrac{V_{ttl}^{3/2}}{\ell_{eff}^2}$	$\varepsilon_o = 8.85 \times 10^{-12}$ F/m $V_{ttl} = |V_{screen}| + |V_{acc}|$ $\ell_{eff} = [(\ell_{gave}+t_s)^2 + (d_s/4)^2]^{1/2}$ ℓ_{gave} = average intergrid distance t_s = screen grid thickness d_s = screen grid hole diameter when $\dot{m}_{C60}/\dot{m}_{Ar} \geq 2.5$ then $m_i = \langle m_i \rangle$ of $C_{60}+C_{70}$ otherwise m_i corresponds to Ar ion mass

TABLE 8.1 (CON'T)

	Quantity	Equation	Notes
19.	Theoretical Space Charge Limited Beam Current (Amps)	$I_{BCL} = J_{BCL} N_H A_H k$	N_H = number of holes in grid $A_H = \pi d_s^2/4$, k factor to account for thermal grid misalignment taken to be 0.75
20.	Thrust (Newtons)	$T = I_B \left(\dfrac{2m_i V_B}{q_e}\right)^{1/2}$	Based on measured I_B using m_i as defined above, V_B= V_{screen} = net acceleration voltage
21.	Specific Impulse (sec)	$I_{sp} = \dfrac{T}{g_o \dot{m}_{ttl}}$	
22.	Mass Flow of Ions $\dot{m}_i$ (kg/sec)	$\dot{m}_i = \dfrac{I_B m_i}{q_e}$	Based on measured I_B using m_i as defined above

$$Q = \frac{I_i}{I_e} \frac{1}{n \, L} \tag{8.1}$$

where n is the neutral gas number density and L is the effective path length of the electrons through the neutral beam which impact ionize the neutrals. Conceptually Rapp's[24] experiment is the same as our discharge chamber that contains both Ar and C_{60}. Therefore, the respective ion currents can be estimated using Eq. [8.1] as

$$\frac{I_{iC60}}{I_{iAr}} = \frac{I_e(QnL)_{C60}}{I_e(QnL)_{Ar}} \approx \left(\frac{Q_{C60}}{Q_{Ar}}\right)\left(\frac{n_{C60}}{n_{Ar}}\right) \tag{8.2}$$

Within the discharge chamber but away from the electrodes and away from sheath region of the grids the electrical fields are low and the ions will drift at essentially thermal velocity. Therefore the ion current ratio from Eq. [8.2] can be also written as

$$\frac{I_{iC60}}{I_{iAr}} = \frac{(n_i u_i q_e A)_{C60}}{(n_i u_i q_e A)_{Ar}} = \frac{(n_i u_i)_{C60}}{(n_i u_i)_{Ar}} \tag{8.3}$$

where u_i is the thermal velocity of the respective ion $\left(\sim \sqrt{T/m_i}\right)$. Within the sheath the ions will acquire Bohm velocity which however, has the same dependence on m_i. Assuming the same temperature of both types of species and equating Eqs. [8.2] and [8.3] yields the ratio of the ion number densities

$$\frac{n_{iC60}}{n_{iAr}} = \left(\frac{n_{C60}}{n_{Ar}}\right)\left(\frac{Q_{C60}}{Q_{Ar}}\right)\left(\frac{m_{C60}}{m_{Ar}}\right)^{1/2} \tag{8.4}$$

where m_{C60} and m_{Ar} are weights of the C_{60} molecule and argon atom, respectively.

To estimate the neutral number densities n_{C60}/n_{Ar} we use perfect gas law $p = nkT$ and known mass flows $(\dot{m})$

$$n_n = \frac{p}{kT} = \frac{1}{kT} \frac{\dot{m}}{A} \sqrt{\frac{2\pi RT}{M_w}} \tag{8.5}$$

where p is the partial pressure of Ar or C_{60}, A is some flow area, M_w is molecular weight and k and R are Boltzman and universal gas constants, respectively. Again, assuming that the Ar and C_{60} neutrals are at the same temperature, the ratio of neutral number densities can be estimated from Eq. [8.3] as

$$\frac{n_{Ar}}{n_{C60}} \cong \frac{\dot{m}_{Ar}}{\dot{m}_{C60}} \left(\frac{M_{wC60}}{M_{wAr}}\right)^{1/2} \tag{8.6}$$

The ion currents in Eq. [8.3] can be viewed as the flux of charges toward the screen grid where they "feel" the applied electric field and get extracted. This flux can be estimated in terms of known quantities by combining Eqs. [8.2] and [8.6] as

BUSEK

$$\frac{I_{iAr}}{I_{iC60}} = \left(\frac{\dot{m}_{Ar}}{\dot{m}_{C60}}\right)\left(\frac{Q_{Ar}}{Q_{C60}}\right)\left(\frac{m_{C60}}{m_{Ar}}\right)^{1/2}$$ [8.7]

By combining Eqs. [8.4] and [8.6] one obtains the ion densities ratio

$$\frac{n_{iAr}}{n_{iC60}} = \left(\frac{\dot{m}_{Ar}}{\dot{m}_{C60}}\right)\left(\frac{Q_{Ar}}{Q_{C60}}\right)$$ [8.8]

Therefore, the ratio of the ion number densities is only dependent on the mass flow of the respective gases entering the discharge chamber and the respective ionization cross-sections. The flux of the charges toward the sheath grid which approximates the extractable beam currents are obtained by combining Eqs. [8.7] and [8.8]

$$\frac{I_{Arbeam}}{I_{C60beam}} \approx \left(\frac{n_{iAr}}{n_{iC60}}\right)\left(\frac{m_{C60}}{m_{Ar}}\right)^{1/2}$$ [8.9]

which depends only the ion densities and the respective weights.

To assess the value of ion density ratio and extractable beam currents, the ionization cross-sections of Ar and C_{60} were taken from Refs. 24 and 25 at electron energy of 38 eV (approximating discharge voltage) yielding

$$\frac{Q_{Ar}}{Q_{C60}} = \frac{2.33x10^{-16}cm^2}{53.5x10^{-16}cm^2} = 0.043$$

Thus, according to Eqs. [8.8] and [8.9] with typical mass flow ratio $\dot{m}_{Ar}/\dot{m}_{C60} < 1$, the argon ion density is negligible and the extractable argon beam is also small relative to the C_{60} beam.

This argument is further reinforced by considering the Penning ionization reaction and charge transfer discussed in Section 2.5 which indicates, that argon ion (Ar^+) is short lived within the C_{60} and C_{70} environment provided that Ar^+ mean free path for Ar^+/C_{60} collision is smaller than the characteristic dimension of the discharge chamber.

Based on the above discussion the criteria somewhat arbitrarily selected for the ion mass (m_i or $<m_i>$) value to be substituted in the equation of space charge current density limit, thrust and mass flow of ions (Eqs. [18], [20] and [22] in Table 8.1) is

for $\dfrac{\dot{m}_f}{\dot{m}_{Ar}} \geq 2.5$ then $m_i = \langle m_i \rangle$ of fullerenes given by Eq. 9 in Table 8.1

[8.10]

for $\dfrac{\dot{m}_f}{\dot{m}_{Ar}} < 2.5$ then $m_i = m_{iAr}$

BUSEK

8.3 Data Analysis

Data from 3 representative tests were analyzed. The first two tests we will discuss used argon fed hollow cathode while the last used heated tungsten filament cathode. Before presenting the analysis we describe using the Test #061796 results as an example how the raw data were processed.

The direct measurements given in Table 7.1 are shown graphically in Fig. 8.2. Parameters of interest obtained from the direct measurements are shown in Fig. 8.3. All variables in Figs. 8.2 and 8.3 are plotted against time (in minutes) at intervals when data were taken. This facilitates easy observation of the impact of the test engineers actions such as adjustments in discharge current or a grid voltage on performance parameters. All variables are defined in Table 8.1. Below we describe how the graphs in Fig. 8.3 were prepared which applies to all other tests to be presented later.

Constant Discharge Current Test (#061796)

The fullerene mass flow ($\dot{m}_f$ = mdotf) using Eqs. 1 through 8 in Table 8.1 is shown as Fig. 8.3a along with the cumulative fullerene mass obtained by integration of $\dot{m}_f$. The ratios of $\dot{m}_f / \dot{m}_{Ar}$ and $\dot{m}_i / \dot{m}_f$ is plotted in Fig. 8.3b. The first ratio is used as a criteria for calculating the appropriate value for the beam ion mass (see Eq. [8.10]) and the second ratio is equivalent to propellant utilization using the fullerene flow rates only. Figure 8.3c compares the measured beam current (I_B), which is the same as that shown in Fig. 8.3e, to the theoretical beam current (I_{BCL} calculated from the space charge current limit (Eqs. 18 and 19 in Table 8.1). Figure 8.3d shows the beam ion energy cost (ε_B) calculated from Eq. 14 in Table 8.1. Figure 8.3e shows the propellant utilization efficiency (η_u) and the electrical efficiency (η_e) calculated using Eqs. 14 and 16 in Table 8.1. Both equations used the measured beam current, discharge power and beam power and use calculated ion mass and total mass flow (Eqs. 9 and 11 in Table 8.1). Figure 8.3f shows thrust (T) and I_{sp} calculated using Eqs. 20 and 21 in Table 8.1 Note that the thrust is calculated using measured quantities and excludes the thrust contribution from flow of neutral species.

Having described how each graph was prepared let us now discuss the results. As seen in Fig. 8.2a the discharge current was held constant for the duration of the test as were the beam voltage (V_{beam} = voltage on the screen grid with respect to ground) and the accelerator voltage (V_{accel}) in Fig. 8.2c. The operator controlled parameters that were changed are the cathode Ar flow (Fig. 8.2b) and the vaporizer temperature (T_{vap}) in Fig. 8.2f. As seen from Fig. 8.2a the changes in the cathode flow (the only source of Ar) resulted in slight variation of the discharge voltage and large variations in the accelerator impingement current (I_{accel}) shown in Fig. 8.2e. The beam current slightly increases when the Ar cathode flow decreases at 67 minutes into the test and starts decreasing when significant amount of fullerenes flow into the discharge (time > 110 min). A decrease in I_B is expected reflecting the change over from Ar beam to the heavier mass fullerene beam. Figure 8.3a shows the fullerene flow rate (mdotf) and its integral giving the cumulative fullerene flow (mcummf) which indicates that 10 grams of fullerenes were vaporized. Since 10 gram wire initially loaded into the vaporizer the calculations agree well with the post test measurement which resulted in 9.86 grams evaporated with 0.14 grams unvaporized residue. Figure 8.3b shows the ratio of the fullerene to argon mass flow and the ratio of the mass flow of ions to masss flow of fullerenes The beam should already be composed mostly out of fullerenes when $\dot{m}_f$ (in Fig. 8.3a) reaches 0.4 mg/sec about 120 minutes into the test. At that point is

BUSEK
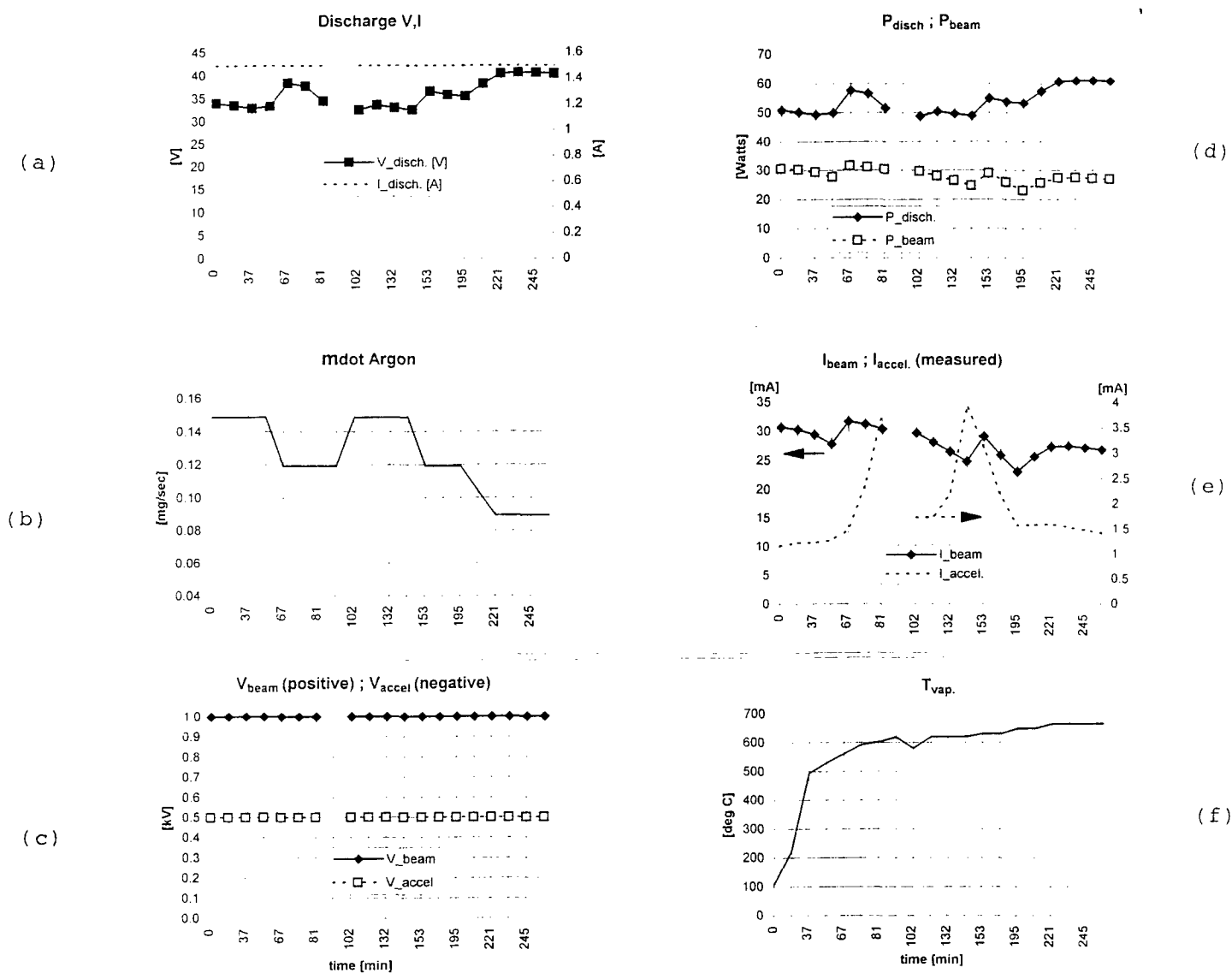
Fig. 8.2 Discharge Current, Voltage, Argon Mass Flow, Grid Potentials, Beam Current, Accelerator Grid Current and the Vaporizer Temperature were Measured and Plotted as a Function of Time into Test (in minutes) for Test ID #061796

63
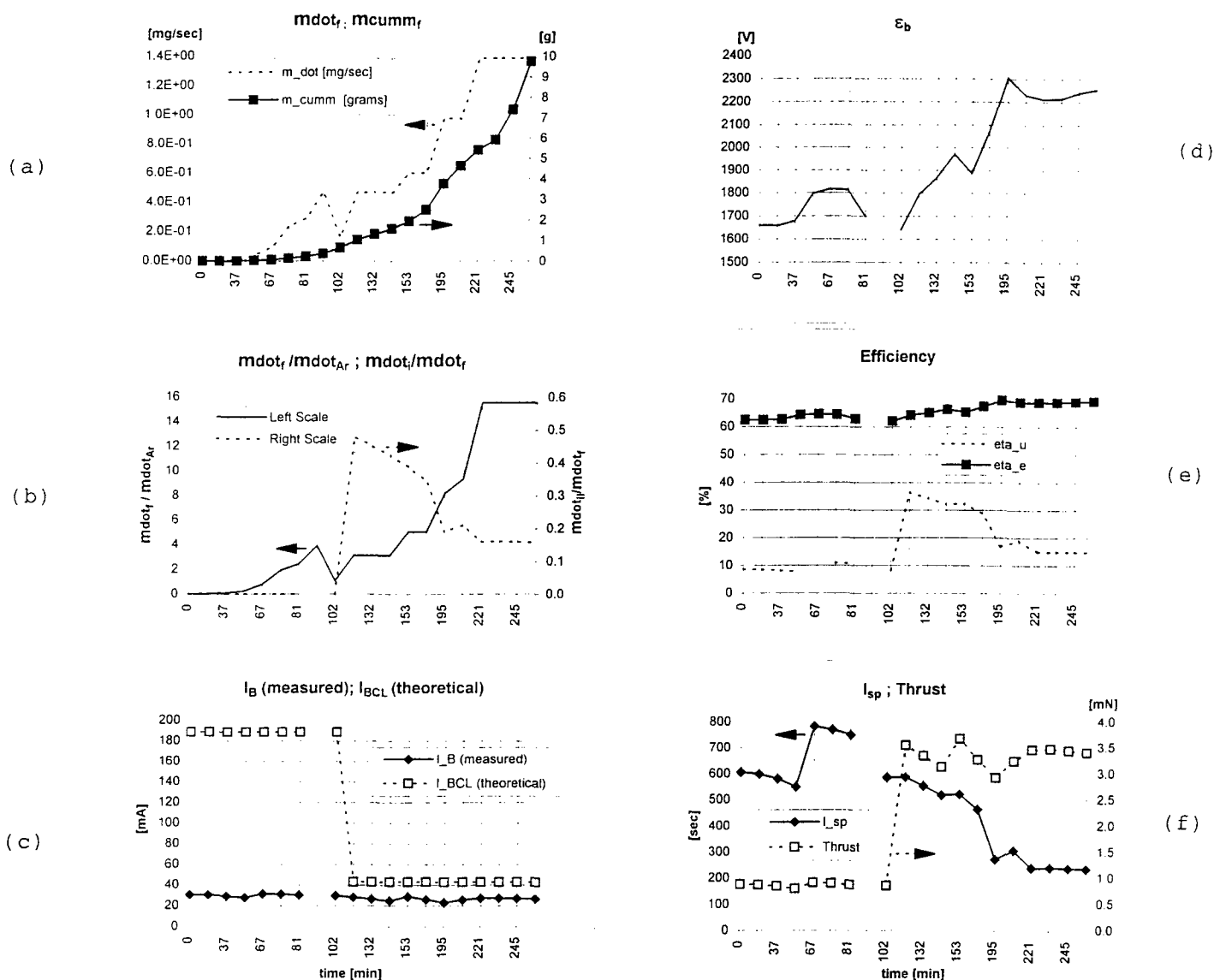
Fig. 8.3   Fullerene Mass Flow (mdotf), Cumulative Fullerene Mass Vaporized (mcummf), Ratio of Fullerene Mass Flow to Argon Mass Flow (mdotf/mdotAr), Ratio of Fullerene Ion Mass Flow to Fullerene Mass Flow (mdoti/mdotf), the as Measured Ion Beam Current (I_B), the Theoretical Space Charge Limited Beam Current (I_{BCL}), the Beam Ion Cost (ε_b), the Electrical (etae) and Propellant Utilization Efficiency (etau), and Finally the I_{sp} and Thrust are Plotted as a Function of Test Time in Minutes. The above parameters were calculated from the measured data in Fig. 8.2 using Equations in Table 8.1.

64

$\dot{m}_i / \dot{m}_f$ about 0.5 indicating that approximately half of the fullerene molecules are extracted as ion beam current.

Figure 8.3c compares the theoretical space charge limited beam current (I_{BCL}) to the measured current (I_B). The IBCL is calculated using argon ion mass until about 102 minutes into the test when according to Eq. [8.10] criteria the ion mass becomes the average mass of $C_{60} + C_{70}$ ions $<m_i>$ (Table 8.1 contains $<m_i>$ definition). Although this selection is supported by the analysis in Section 8.2 the transition from Ar beam to mostly fullerene beam is gradual and the value of I_{BCL} in Fig. 8.3c represents the theoretical limits. It is therefore seen that in the second half of the test when the fullerene mass flow is sufficiently high, the measured ion beam at 25 to 30 mA is reasonably close to the theoretical limit of about 42 mA. It should also be noted that 30 mA ion beam current exceeds that reported by Nakayama[11] by nearly a factor of 4.

Figure 8.3d shows the ion beam cost (ε_B) whose calculations also involves the two different values of ion mass (for argon and fullerenes) discussed in the preceding paragraph. As seen the value of ε_B in the second half of the test is unacceptably high ranging between 1700 to 2300 volts with relatively stable value of 2250 volts at the highest fullerene flow rate.

Figure 8.3e shows the electrical and the propellant utilization efficiencies. Even operating on pure Ar at the beginning of the test resulted in a low (~10%) utilization efficiency indicating high losses in the discharge chamber. The stable values at the highest fullerene flow rate toward the end of the test are 70% and 15% for the electrical and utilization efficiencies, respectively. While both values are not acceptable for space propulsion, the utilization efficiency exceeds that reported by Nakayama[11] by a factor of 2.

Figure 8.3f shows I_{sp} and thrust. As seen in Table 8.1, Eq. 20, the thrust is based on measured beam current and the ion mass which was selected according to the previously discussed criteria. The change in ion mass from Ar to fullerene ion is responsible for the observed step change in the thrust level from about 1 mN to 3.5 mN. These two values should be viewed as thrust limits while operating with Ar only and mostly fullerenes toward the end of the test. Both thrust and Isp are low even when operating on pure Ar at the beginning of the test indicating high losses in the discharge chamber along with small open fraction of our low cost grids.

Variable Discharge Current and Intergrid Voltage Test (#071696)

Figure 8.4 and 8.5 present the measured and calculated parameters, respectively for a representative test where the discharge current was varied from 1.5 to 0.7 Amps (Fig. 8.4a) and the beam voltage was varied between 1000 to 500 volts while the accelerator voltage was held at -500 volts (Fig. 8.4c). The data are presented in the same manner as for the previous test (Fig. 8.2 and 8.3) and all calculations were performed in an identical manner.

The fullerene mass flow presented in Fig. 8.5a was similar to the previous test (see Fig. 8.3a) and integrated into cumulative value of about 8.3 grams. Pre and post test weighing of fullerenes in the vaporizer indicated that 8.4 grams were vaporized giving good closure and reasonable confidence in the fullerene flow rate calculations. The beam current shown in Fig. 8.4e (in addition to the accelerator grid current) is a factor of 2 to 4 lower than the beam current in Fig. 8.2e. This is true even at the beginning of the test when operating on the cathode argon flow only, yet the discharge current and the grid voltages were the same during that interval (43 to 88 minutes into the test in Fig. 8.4a and 8.2a)

The reason for this difference is the significantly lower Ar flow (0.075 mg/sec versus 0.15 mg/sec in Fig. 8.2a) which also resulted in higher discharge voltage (54 volts in the present test
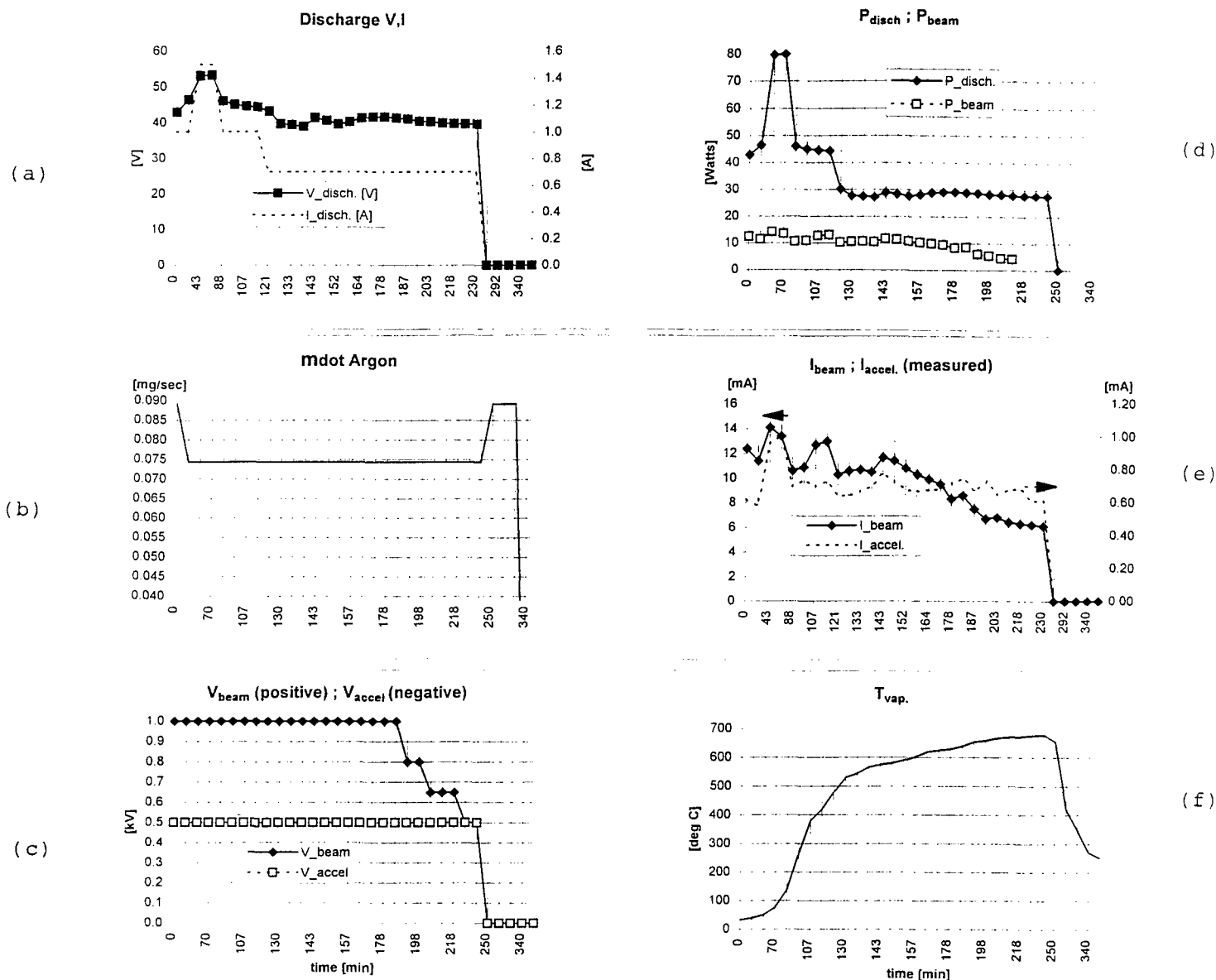
Fig. 8.4 Discharge Current, Voltage, Argon Mass Flow, Grid Potentials, Beam Current, Accelerator Grid Current and the Vaporizer Temperature were Measured and Plotted as a Function of Time into Test (in minutes) for Test ID #071696
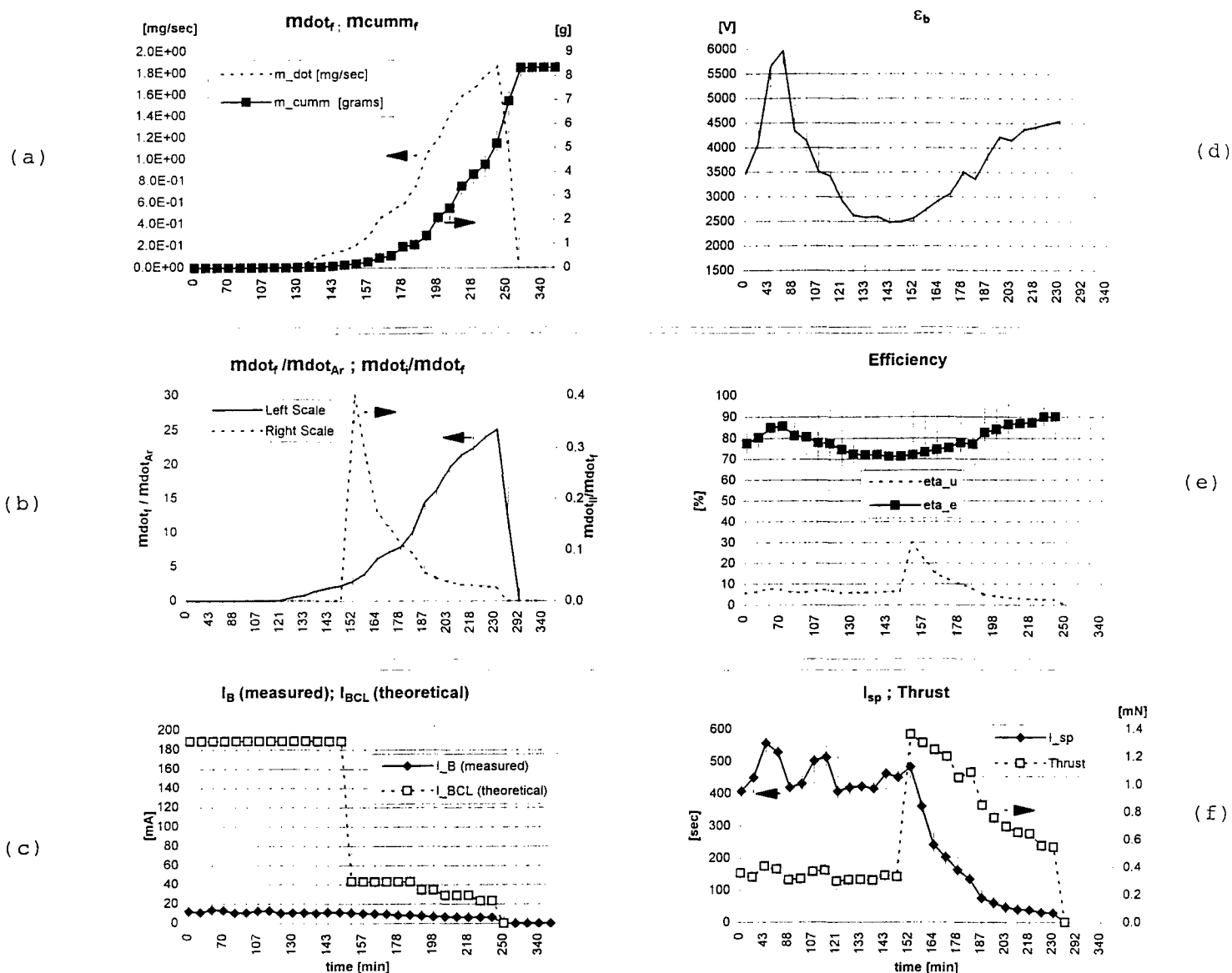
66

Fig. 8.5   Fullerene Mass Flow (mdotf), Cumulative Fullerene Mass Vaporized (mcummf), Ratio of Fullerene Mass Flow to Argon Mass Flow (mdotf/mdotAr), Ratio of Fullerene Ion Mass Flow to Fullerene Mass Flow (mdoti/mdotf), the as Measured Ion Beam Current (I_B), the Theoretical Space Charge Limited Beam Current (I_{BCL}), the Beam Ion Cost (ε_b), the Electrical (etae) and Propellant Utilization Efficiency (etau), and Finally the I_{sp} and Thrust are Plotted as a Function of Test Time in Minutes. The above parameters were calculated from the measured data in Fig. 8.4 using Equations in Table 8.1.

BUSEK

relative to 35 volts in Fig. 8.2a). At high fullerene flow rates toward the end of the test the discharge voltages were about the same for both tests even though the discharge currents were a factor of 3 different indicating that fullerenes dominated the discharge conditions. The beam current decreased with increasing fullerene flow rate, which is an expected behavior given the beam current dependence on the ion mass. The beam current (Fig. 8.4e) shows appropriate dependence to decreasing intergrid voltage but the accelerator impingement current stays relatively constant. The beam ion cost (Fig. 8.5d) the propellant utilization efficiency (Fig. 8.5e) and the thrust are a factor of 2 to 3 worse than in the previously discussed test indicating that the lower discharge current (0.7 Amps versus 1.5 Amps in previous test) produced insufficient ion density in the discharge chamber.

Test with Filament Cathode (#073196)

To explore the role of Ar in the discharge chamber and to compare our data with others[7,11] a filament cathode described in Section 4.3.1 was used in place of the argon operated hollow cathode. The resulting data are shown in Figs. 8.6 and 8.7.

As seen in Fig. 8.6a the discharge was started (after heating the filament cathode) on the background pressure in the tank which was approximately 9×10^{-6} torr. Because of the low pressure the discharge voltage reached nearly 180 volts. With the grid voltages already established the beam current was about 1.5 mA. When Ar was introduced into the discharge chamber (at about the same rate as in the previous test shown in Fig. 8.4b) the beam current rose to about 5.5 mA and the discharge voltage dropped to approximately 20 volts. Argon flow was turned off at approximately 130 minutes into the test and the beam current returned to nearly identical value as at the start of the test. Argon flow was then restarted while the fullerene vaporizer temperature (T_{vap} in Fig. 8.6f) was rising and starting to deliver appreciable fullerene flow into the discharge chamber (time into test > 170 min in Fig. 8.7a). At this point the beam current was decreasing essentially duplicating the beam current level and pattern observed with the hollow cathode in the previous test (see Fig. 8.4e at 143 min into the test). The significant difference however, is that the discharge current in the present filament cathode test was 1.5 Amps (Fig. 8.6a, 145 to 190 minutes interval) while in the previous test the same beam current was delivered at only 0.5 Amp discharge current. This indicates that even with Ar in the discharge chamber, the filament cathode is negatively impacting the fullerene ion production. This is further reinforced by comparing the beam currents delivered at the same discharge current of 0.5 Amps. In the present filament cathode test (Fig. 8.6a) this occurred at about 227 min into the test with a beam current of only about 2.5 mA (Fig. 8.6e) while at nearly the same conditions in the hollow cathode test the beam current was about 8 mA (Fig. 8.4e at 178 min). It required 2.5 Amps discharge current to produce 8 mA beam current with the filament cathode (Fig. 8.6a and 8.6e at 227 min).

The indisputable evidence that filament cathode discharge is negatively impacting the fullerene ion production came in post test observation of fullerene remnants in the discharge chamber. While there was always carbon film left on the walls of the chamber with hollow cathode tests (see Section 7.3), the amount of carbon residue after the filament cathode tests approached the amount evaporated which provides explanation for the low beam current.

8.4 Carbon Film Deposition Results

Several samples of residue from the discharge chamber and samples from films deposited on substrates using the energetic fullerene beam were sent to SRI International for analysis. The results are briefly discussed next.

The samples from the discharge chamber were collected from the discharge chamber walls following several tests with the hollow cathode. As described in Section 7.3 they were thin carbon
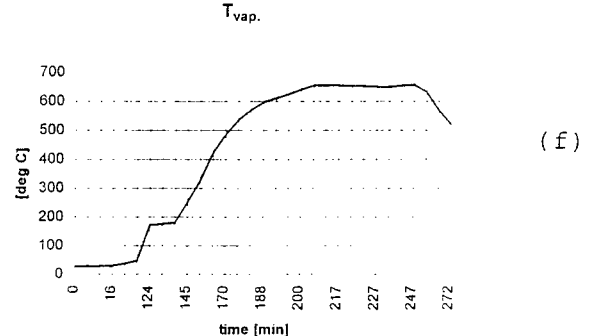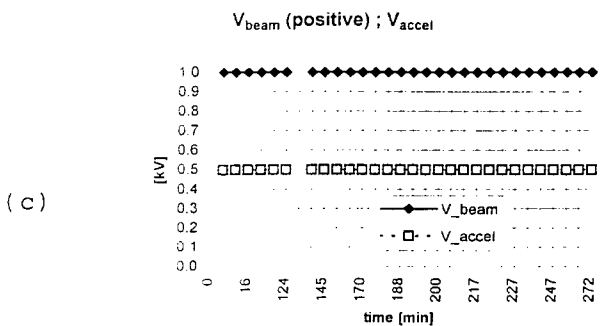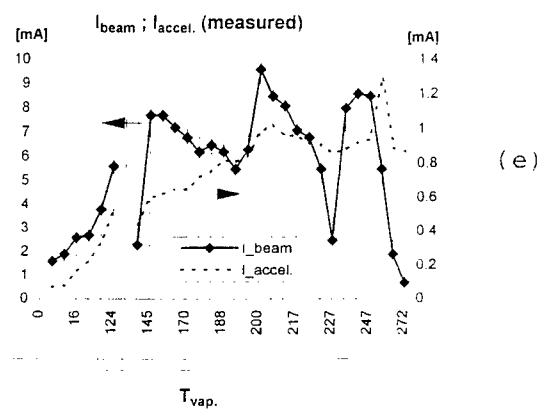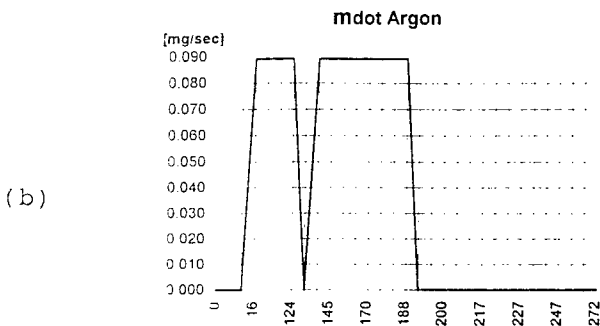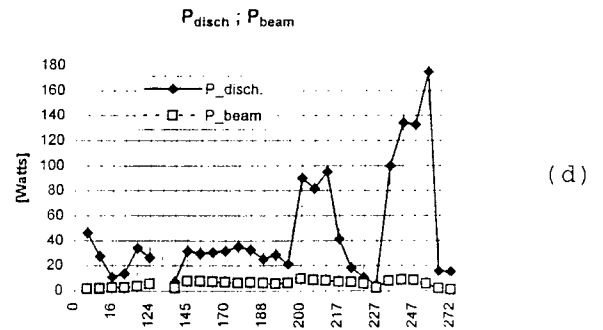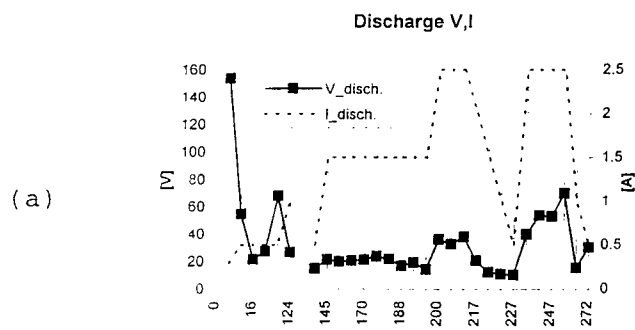
Fig. 8.6 Discharge Current, Voltage, Argon Mass Flow, Grid Potentials, Beam Current, Accelerator Grid Current and the Vaporizer Temperature were Measured and Plotted as a Function of Time into Test (in minutes) for Test ID #073196

69
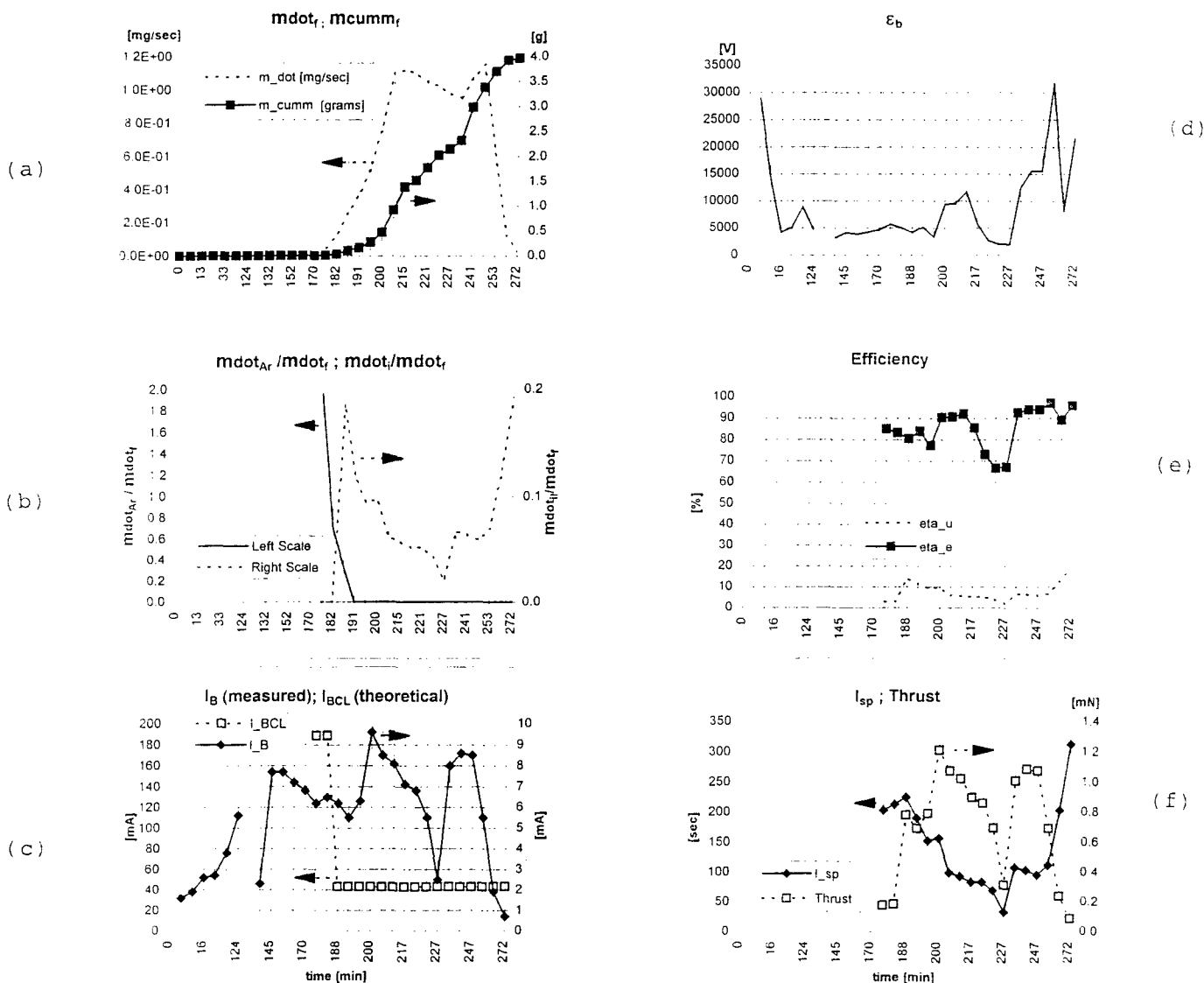
Fig. 8.7 Fullerene Mass Flow (mdotf), Cumulative Fullerene Mass Vaporized (mcummf), Ratio of Fullerene Mass Flow to Argon Mass Flow (mdotf/mdotAr), Ratio of Fullerene Ion Mass Flow to Fullerene Mass Flow (mdoti/mdotf), the as Measured Ion Beam Current (I_B), the Theoretical Space Charge Limited Beam Current (I_{BCL}), the Beam Ion Cost (ε_b), the Electrical (etae) and Propellant Utilization Efficiency (etau), and Finally the I_{sp} and Thrust are Plotted as a Function of Test Time in Minutes. The above parameters were calculated from the measured data in Fig. 8.6 using Equations in Table 8.1.

70

BUSEK

flakes with typical dimensions of 3 to 4 mm in length, 1 to 2 mm in width and 0.1 mm or less in thickness. These samples were examined using a variety of techniques including RAMAN, X-ray, SALI-MS and TEM. The mass spectrometry show only a very weak C_{60} signal and required a strong desorption laser power to see it. We can conclude from this that the C_{60} has been mostly destroyed.

The Raman measurements were done by Wolfgang Bacsa at IPE in Lausanne, Switzerland who has done a lot of Raman work on C_{60} samples. The spectrum Bacsa obtained on the sample in the range of 500 to 2000 cm^{-1} is shown in Fig. 8.8. There is no evidence for diamond like or sp^3 bonding however, the bands are broadened by disorder. Bacsa has not identified all these bands but he concludes that the peaks in the 1740 cm^{-1} are C-O bonds and the bands in the 1550-1620 region are graphene layers or fragments. The major C_{60} lines are either absent or very weak indicating that the C_{60} is indeed highly damaged. However, he concludes that the sample is not amorphous because it contains so many discrete bands which must be due to an abundance of molecular bound structures. Purely amorphous carbon would give much broader Raman spectra than that seen in this sample.

The X-ray diffraction (Fig. 8.9) also shows that the C_{60} structure is not crystalline C_{60}, however it does show some scattering intensity in the region of the 220 and 311 directions. This indicates that some ordering of the carbon atoms remains in the sample but it is nearly completely amorphous.

For TEM analysis the sample was dispersed by sonication in alcohol and mounted on fine mesh copper TEM grids. Only a few photos were taken but they clearly show some interesting structure including a few contorted fullerene like tubes that have grown in this sample. There also seem to be other particle-like structures that are not very well resolved. These might be clusters of damaged buckyballs but they might also be graphitic particles. There is insufficient resolution to see individual graphitic layers with this particular TEM. The growth of tubes is very surprising under these conditions but it is apparently a minor component of the material.

Temperature dependent resistivity measurements done on this sample are shown in Fig. 8.10. These measurements appear appropriate for disordered graphite however they are consistent with the results of Maiken and Taborek[26] for hard amorphous carbon film deposited using fullerene beam on a heated substrate.

The analysis of carbon films deposited on stainless steel and plastic (Kapton tape) substrates using energetic fullerene ion beams (~1000 eV) are not complete. The only diagnostic tests completed are the mass spectrum analysis which detected no fullerenes. Visually, the films appear consistent with diamond like carbon (DLC).

8.5 Discussion & Recommendations

The combination of hollow cathode (avoiding hot surfaces such as the filament cathode) and noble gas environment may be the most likely reason for the significantly better results with the hollow cathode than with the filament cathode. Filament cathode is likely to fragment fullerenes in two different ways — first is the obvious thermal fragmentation which occurs at 800°C and above and the second is negative fullerene creation by contact ionization where the electronegative fullerene removes an electron from a low work function surface. The negative ion is then trapped in the discharge chamber until it hits the walls, fragments and remains as a residue. Additionally it is possible that the presence of Ar in the discharge chamber provides energy distribution/equilibration path from highly excited fullerenes to neutrals thus reducing fullerene fragmentation.
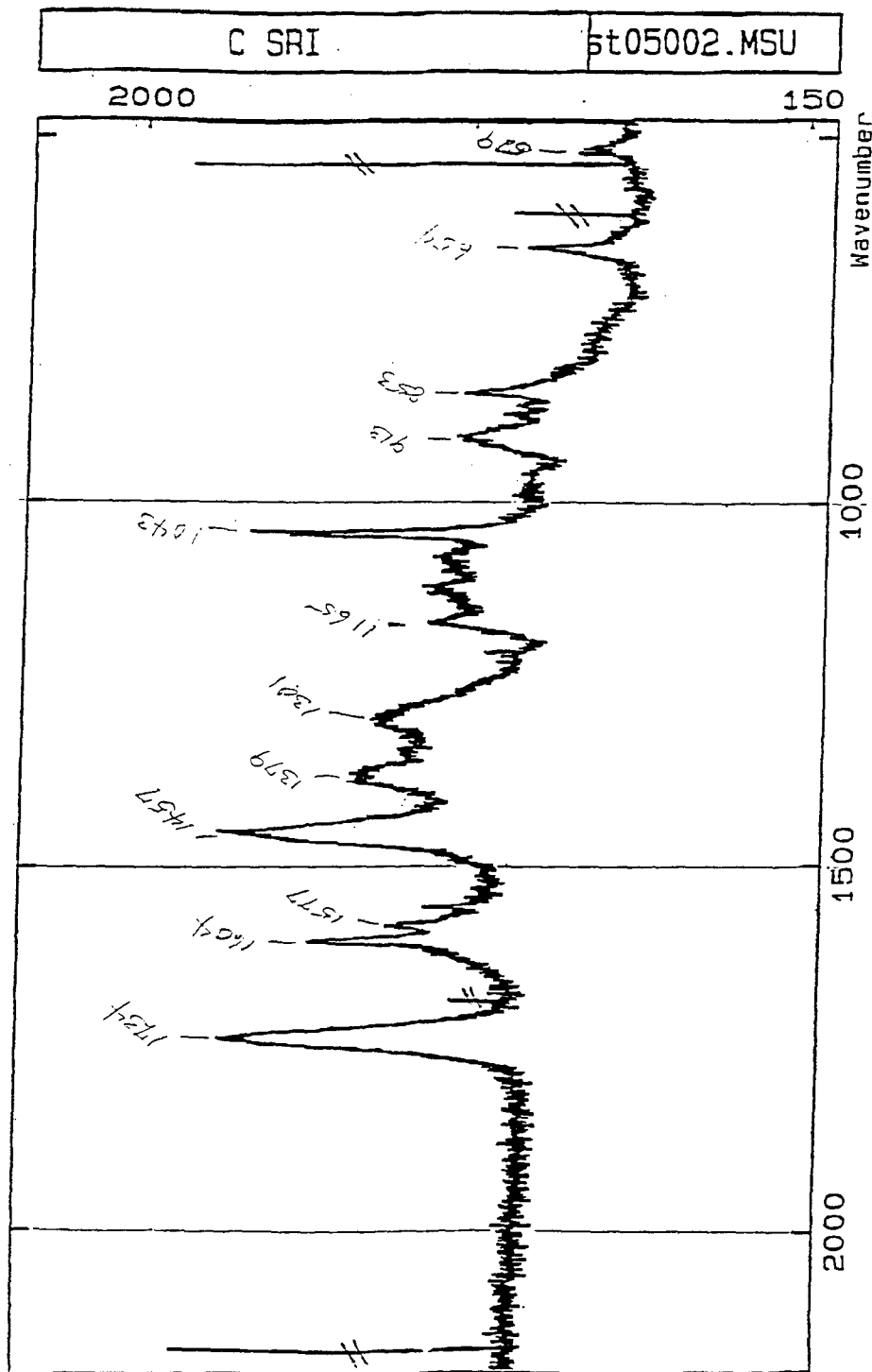
BUSEK

Fig. 8.8 Raman Spectrum of a Sample from Discharge Chamber that Shows Insufficient Broadening for Amorphous Carbon Structure

72

ID: Test 10/3/95 Collected from Discharge Chamber (45kV, 35mA)
File: 7154.MDI   Scan: 10-100/.05/ 2/#1801, Anode: CU

1> 44-0558: C60 - Carbon
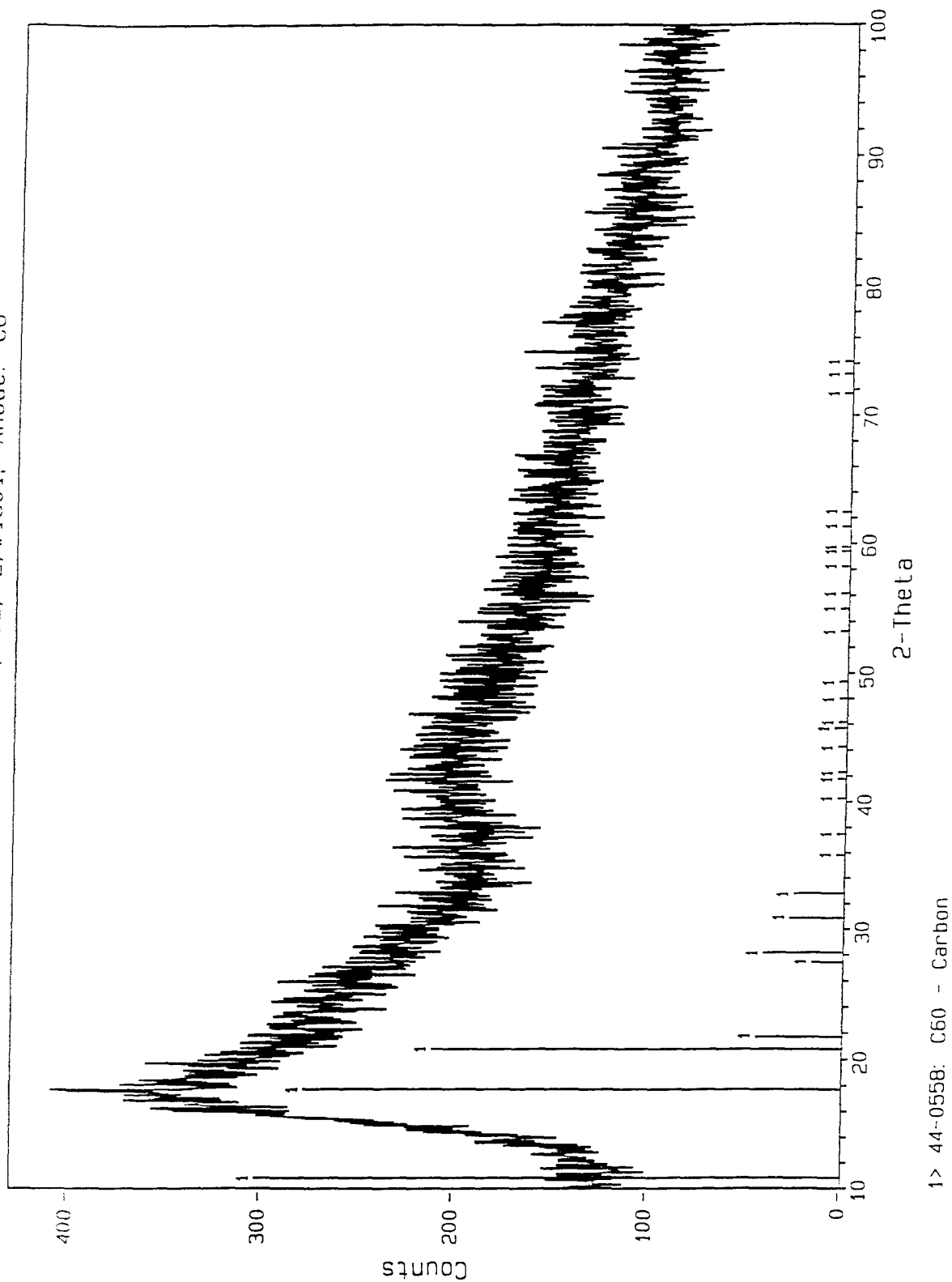
Fig. 8.9 X-ray Spectrum of a Sample from Discharge Chamber that Indicates Nearly Completely Amorphous Sample

73

1SilverC60.mac

1SilverC60.mac
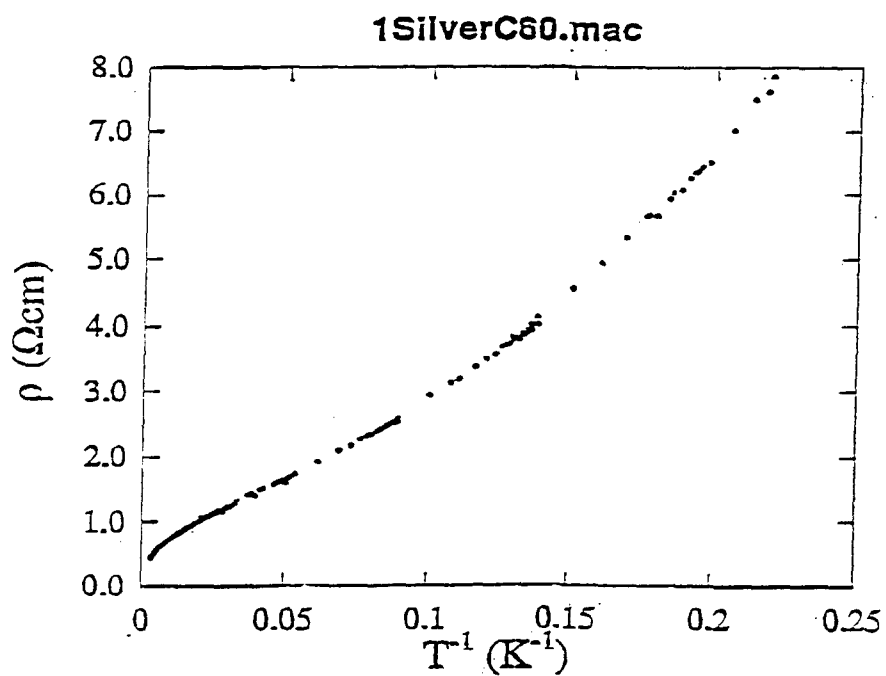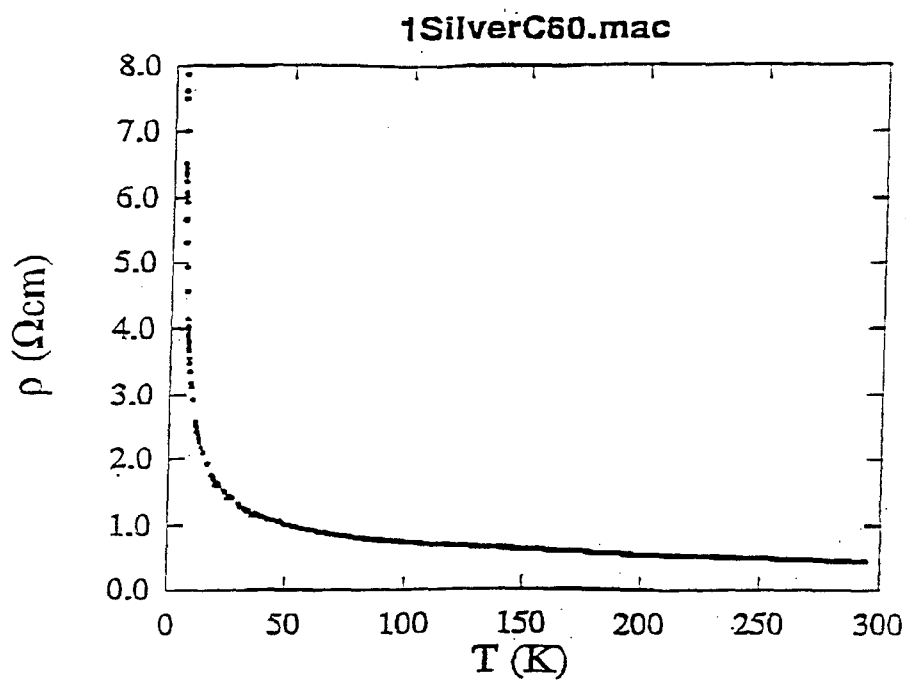
Fig. 8.10   Electrical Resistivity of a Sample from Discharge Chamber as a Function of Temperature

BUSEK

As was discussed in Section 1.2 the high carbon residue in the discharge chamber while operating with filament cathode was also reported by Anderson, et al[7] but not by Nakayama.[11] Our own experience from Phase I of the program, where we used filament cathode in quartz discharge chamber, is somewhat inconclusive because fragmented fullerenes were found only on the filament cathode and on the chamber walls nearest to the filament but most of the chamber walls were residue free.

Overall the performance of the thruster is disappointing even when operating with the hollow cathode. While the initially predicted thrust (see case 2 in Table 4.1) and beam current are within about a factor of 2 of the best measured values, the experimental beam ion cost is factof of 5 higher than predicted. Most importantly, despite the evidence that the beam was primarily fullerenes (based on presented data and based on the fact that deposited films were not fullerenes but hard carbon films which requires at least 100 eV impact) we have not conclusively demonstrated that the discharge and the beam operated on fullerenes in the presence of Ar. To resolve these issues and to bring the thruster to predicted performance we recommend the following future work:

1) Use mass spectrometer or ($\overline{E}x\overline{B}$ probe) to determine the beam composition (C_{60}^+, C_{60}^{++}, C_{70}^+, Ar^+, etc.). Such instrumentation is extremely expensive and not available to this limited budget program.

2) Upgrade the grid system to one that is dished to minimize screen and acceleration grid misalignment at operating temperature and increase the open area fraction. Grids with 1470 number of holes (see Table 4.2) as opposed to our low cost grids with 829 holes would significantly improve the thruster performance. The best alternative may be high open area carbon/carbon grids.

3) Improve electron and ion containment in the discharge chamber through shorter discharge chamber and better magnetic field utilization.

4) Perform detail study on the role of argon mixed with fullerene vapor in the discharge chamber. Other noble gases may be worthy of investigation. Neon, because of its smaller ionization cross-section (which should, according to Eq. [8.8] ensure that only fullerene ions are produced) and He because of its higher thermal conductivity. However, operating hollow cathode on He may be problematic

5) Develop a method for direct measurement of fullerene vapor pressure and hence mass flow. Capacitive pressure gauge made of quartz is a possibility. We carried out its initial development under a BMDO sponsored program.[27] The alternative way to measure mass flow is quartz microbalance which is however, very difficult to use in the hot environment adjacent to the vaporizer.

6) Develop high temperature low pressure valve to turn the fullerene flow on and off at will. This would greatly simplify testing.

7) Carry out experiments using pure C_{60} propellant (as opposed to C_{60}/C_{70} mix) to determine which species is more likely to fragment. Because C_{70} is not spherical it is reasonable to expect that it is more susceptible to fragmentation.

BUSEK

9.0 CONCLUSIONS

A novel 13 cm fullerene fueled, dc discharge ion thruster system consisting of propellant storage and vaporizer integrated with the thruster was designed, constructed and tested.

A fullerene vaporization study was carried out concurrently in a separate apparatus which resulted into initial propellant preparation specifications. The recommended steps include initial propellant drying at 600 K in vacuum for 10 hours, followed by sublimation and condensation of the fullerenes. Only the condensed material should then be used as the propellant. The propellant should be stored in dark containers under inert gas to avoid surface polymerization which precludes predictable vaporization.

Several types of tests were carried out with the thruster system using (1) hollow cathode in the discharge chamber that was operated on argon and (2) 2% thoriated tungsten filament cathode. The carbon residue inside the discharge chamber while operating with the argon fed hollow cathode was finite but orders of magnitude below that observed when operating with the filament cathode which resulted in discharge chamber carbon residue approaching the amount vaporized. This is attributed to (1) thermal fragmentation of fullerenes by the filament cathode, (2) possible negative fullerene ion formation and (3) due to unknown beneficial effects of argon when using hollow cathode.

Using the hollow cathode, beam currents of the order of 30 mA were reached at total intergrid voltage of 1.5 kV yielding thrust level in excess of 3 mN. Low utilization efficiency ranging between 8 to 20% yielded low I_{sp} of the order of a few hundred seconds. This performance was about a factor of 2 below that initially predicted but exceeded by about a factor of 2 the best data published by others. Improvements in discharge chamber design and the grid system are certain to elevate this performance. Exploratory experiments related to amorphous carbon film deposition on various substrates yielded positive results opening a possible terrestrial application for this thruster.

Continuation of this study toward promising and practical fullerene ion propulsion with possible dual (terrestrial) use is strongly recommended.

BUSEK

APPENDIX A

PARTICLE SIMULATION OF GRID EROSION
USING A MIXED PROPELLANT

ERC-R94-090

Particle Simulation of
Grid Erosion Using a Mixed Propellant

Subcontract No. 036-SUB3

Submitted to:

Busek Co. Inc.
19 Kearney Road
Needham, MA 02194

ERC

INCORPORATED

205 Research Park Drive
P.O. Box 417
Tullahoma, TN 37388
Tel: 615/455.9915
Fax: 615/454.2042

December 20, 1994

Particle Simulation of Grid Erosion Using a Mixed propellant

I . Introduction

The objective of this project was to model the ion thruster operated on a C-60 and Ar propellant mixture by using ERC's particle simulation plasma code. The particle simulation plasma code, which is based on the particle-in-cell (PIC) method coupled with the Monte Carlo technique for charge-exchange collisions, was developed by Peng of ERC and his coworkers (Ref. 1-3). It has been used for both two- and three-grid ion thruster simulations. A present, this simulation code can only treat single species. As a approximation, a two-dimension, two-grid and single species model was used to calculate the electric potential field and beam current with C-60 propellant due to its larger mass and higher mass flow ratio as compared to Ar (9:1 ratio). The impingement current and grid erosion of the accelerator grid were calculated using Ar since the cross section of the charge exchange collision between C-60 and C-60$^+$ is not known. In order to find the equivalent C-60 neutral impingement current to the accelerator grid and the accurate neutral density of Ar on each computational mesh point, simulations of the neutral flow from the discharge chamber were conducted by using our Direct Simulation Monte Carlo(DSMC) code for both C-60 and Ar gases, respectively. Detail simulation results are presented herein.

II. Simulation Results

1. Geometry

Simulations were performed with two-grid ion optics operated on C-60 and Argon propellant mixture. The grid pattern was chosen to be rectangular, and the diameter of the thruster is 130 mm. Three configurations were chosen for the ion optics simulations. For all three configurations, the accelerator grid diameter was 2 mm, the center-to-center distance between adjacent accelerator grid apertures was 3 mm, and the thickness of both the accelerator and screen grids was 0.5 mm. Two different screen grid diameters were used; 2 mm and 2.5 mm, respectively. Two different grid spacings were used; 1 mm and

0.75 mm, respectively. Different screen grid diameter and grid spacing results in different electric potential field around the grid region; therefore, it provides different ion optics systems. To optimize the ion optics system for a specific mission, more simulations are required.

All the geometry and input parameters are listed in the Table 1 and 2.

It is assumed that a neutral plasma exists at the upstream boundary of the computational domain, with an ion temperature 1000 K and an electron temperature of 1.5 eV. The background pressure of the vacuum chamber is assumed at 8×10^{-5} Torr and the propellant is mixed as ninety percent C-60 and ten percent Argon.

Table 1. Parameters

diameter of thruster	0.13 m
discharge voltage	30 V
ion temperature	1000 K
electron temperature	1.5 eV
tank pressure	8×10^{-5} Torr
propellant	90% C_{60}, 10% Ar

Table 2. Grid configurations

	case # 1 (mm)	case #2 (mm)	case #3 (mm)
diameter of accel. grid	2.0	2.0	2.0
diameter of screen grid	2.0	2.5	2.5
grid hole pitch	3.0	3.0	3.0
grid spacing	1.0	1.0	0.75
thickness of accel. grid	0.5	0.5	0.5
thickness of screen grid	0.5	0.5	0.5

2. Potential field simulation

Only C-60 was used in the ion optics simulation. The contribution of the Ar to the potential field was neglected. This assumption introduced some small errors in the electric field simulation because Ar is much lighter than C-60. Since the cross section of the charge exchange collision between C-60 and C-60$^+$ is not available and its effect on the potential field is assumed to be small, the contribution of the slow ion of C-60 to the potential field was neglected.

The ion optics were simulated by using a two-dimensional axisymmetric particle simulation code based on the particle-in-cell (PIC) method coupled with the Monte Carlo technique for charge-exchange collisions. In the simulations, ion particles were introduced into computation domain in the upstream region of the screen grid and then were extracted and accelerated through grid apertures to the downstream of the thruster by the electric potential field. The potential field was calculated by solving Poisson's equation at each computational mesh point. The calculated potential fields for three different grid configurations are shown in Figs.1-3 for intergrid potentials of 1500 V, 2000V, and 3000V, respectively. For all three cases, the accelerator grid potential was chosen at -500 V.

1500 V intergrid potential cases

Figs. 1a, b, and c show the calculated electric potential fields under three different geometry configurations. For comparisons, the same upstream plasma number density was used in these simulations. The calculated beam currents for these three grid configurations are shown in Table 3.

**Table 3. Comparisons of beam current for different configuration
at intergrid voltage 1500V (Va= -500V, Vs=1000V)**

	case #1	case #2	case #3
theoretical value (J_max)	173 mA	231 mA	282 mA
simulated value	106 mA	178 mA	196 mA
upstream plasma density	4.0×10^{17} $1/m^3$	4.0×10^{17} $1/m^3$	4.0×10^{17} $1/m^3$

In Table 3, the maximum theoretical current J_max is calculated by,

$$J_H = \left(\frac{\pi \varepsilon_0}{9} \right) \left(\frac{2q}{m} \right)^{1/2} V_T^{3/2} \left(\frac{d_s}{l_E} \right)^2$$

where V_T is the intergrid voltage and l_E is defined as

$$l_E = \left(l_G^2 + \frac{d_s^2}{4} \right)^{1/2}$$

where l_G is the grid spacing.

The simulated current is lower than J_max because the simulation code experienced a difficulty in simulating the beam current close to the theoretical maximum limit. The calculated perveance is about 77% of the theoretical maximum value for case 2. In order to simulate higher beam current, a relative high plasma density (4×10^{17} m^{-3}) was input into the upstream boundary. This high plasma density resulted in a concave potential along the upstream equal-potential contour of the screen grid with a cusp toward the grid region. The concave potential with the cusp will prevent extraction of the high beam current and will affect the half divergence angle of the ion beam. (In practice, the accelerator system may reach the maximum perveance condition without the type of difficulty the numerical simulation code experienced.)

In Table 3, the geometry 1 has the least perveance while geometry 3 has the most. This is indicated by the electric potential field around the upstream plasma sheath region. In Fig.1a (case 1), the potential concave is much deeper toward the screen grid because the upstream plasma density (4×10^{17} m^{-3}) is relatively high for case 1. Hence, the plasma boundary is pushed further toward the grids for case 1 than for cases 2 (Fig. 1b) and 3 (Fig. 1c), and the beam current extracted by case 1 is lower than case 2 and case 3. The ion beams are closer to the accelerator grid for configurations 2 and 3 than for configuration 1.

2000 V intergrid potential cases

Figs. 2a, b, c shows the equal electric potential contours and ion optics with a total voltage of 2000V. Again, an upstream plasma density, 6×10^{17} m^{-3}, was assumed. Because of the higher intergrid potential, higher beam currents can be achieved as compared to the previous ones. Among the three geometric configurations, similar trend is shown as in the 1500 V cases, that is configuration 1 extracted less beam current than did configuration 2 and 3. The concave potential also exists along the equal potential contour upstream of the screen grid with a cusp toward the grid region. The calculated beam currents for the different configurations at the intergrid voltage of 2000 V are shown in Table 4.

**Table 4. Comparisons of beam current for different configuration
at intergrid voltage 2000V (Va= -500V, Vs=1500V)**

	case #1	case #2	case #3
theoretical value (J_max)	265 mA	353 mA	431 mA
simulated value	147 mA	265 mA	296 mA
upstream plasma density	6.0×10^{17} 1/m^3	6.0×10^{17} 1/m^3	6.0×10^{17} 1/m^3

3000 V intergrid potential cases

Figs. 3a, b, and c show the equal electric potential contours and beam ions with a total voltage of 3000 V. Again, a plasma density of 1×10^{18} m^{-3} was used for these calculations. Higher total accelerating voltage can yield higher beam current. The calculated beam currents for the different configurations at the intergrid voltage of 3000 V are given in Table 5. The maximum beam current for the 3000V of the intergrid voltage at the same configuration is much higher than that for 1500V and 2000V of the intergrid voltages.

Table 5. Comparisons of beam current for different configuration at intergrid voltage 3000V (Va= -500V, Vs=2500V)

	case #1	case #2	case #3
theoretical value (J_max)	483 mA	644 mA	786 mA
simulated value	274 mA	471 mA	502 mA
upstream plasma density	1.0×10^{18} 1/m^3	1.0×10^{18} 1/m^3	1.0×10^{18} 1/m^3

From the ion optics point of view, the geometry of configuration 1 has poorer performance than that of configurations 2 or 3. Therefore, configuration 1 is not recommended (only from the better ion optics point of view). Between configurations 2 and 3, configuration 3 provides higher beam perveance while configuration 2 requires less of grid alignment. Since the vacuum chamber pressure is at about 8×10^{-5} Torr, configuration 3 might experience significant intragrid arcing because of its shorter grid spacing. Therefore, the geometry of configuration 2 with total intergrid voltage of 2000 V was selected for the grid erosion simulation. And, the calculated potential field of C-60 at the intergrid potential of 2000V for case 2 was saved for the further grid erosion simulation using Ar.

3. Neutral flow simulation

In order to find the equivalent neutral impingement current of the accelerator grid due to the atom C-60 and the accurate neutral density of Ar on each computational mesh point, the neutral flow lost from a discharge chamber was simulated by using Direct Simulation Monte Carlo (DSMC) type of code for both C-60 and Ar gases, respectively. In the calculations, the propellant was assumed to be a pure gas and escaped from the discharge chamber.

The equivalent neutral impingement currents of the accelerator grid (J_na) were calculated for C-60 in two grid configurations. The calculated results are shown in Table 6. The J_na for case 2 is higher than that for case 1 because the screen grid hole diameter in case 2 is larger than the accel grid hole diameter. Therefore, there are more neutral particles striking the accel grid. Since the energy of a neutral particle is much lower than the sputtering threshold, the higher equivalent neutral impingement current of the accelerator grid in case 2 will not cause much damage to the grid, Therefore, case 2 is more favorable than case 1 because of its better ion optics.

Table 6. Equivalent neutral impingement current of the accel. grid due to the
neutral loss from the discharge chamber

	case #1 (mA)	case #2 (mA)
J_na	21.2	48.2

The neutral density distribution of the argon on the computational mesh points was calculated for the grid configuration 2 and was used for the calculation of charge exchange collisions and the calculation of impingement current and erosion of the accelerator grid. Since the propellant utilization efficiency is 0.8 and only 10% of the propellant is the argon, the neutral density due to neutral loss from the discharge chamber is much less than the neutral density caused by the background pressure at 8×10^{-5} Torr.

Therefore, the grid erosion of the accelerator grid is mainly determined by the background pressure.

4. Grid erosion simulation

The grid erosion of the accelerator grid due to slow charge exchange ions was calculated for configuration 2 at an intergrid potential 2000V. Four charge exchange collisions can happen during the extraction and acceleration processes,

$$C\text{-}60^+ \text{ (fast)} + Ar \text{ (slow)} \text{ ---- } C\text{-}60 \text{ (fast)} + Ar^+ \text{ (slow)} ,$$
$$Ar^+ \text{ (fast)} + C\text{-}60 \text{ (slow)} \text{ --- } Ar \text{ (fast)} + C\text{-}60^+ \text{ (slow)},$$
$$C\text{-}60^+ \text{ (fast)} + C\text{-}60 \text{ (slow)} \text{ ---- } C\text{-}60 \text{ (fast)} + C\text{-}60^+ \text{ (slow)} ,$$
$$Ar^+ \text{ (fast)} + Ar \text{ (slow)} \text{ ---- } Ar \text{ (fast)} + Ar^+ \text{ (slow)}.$$
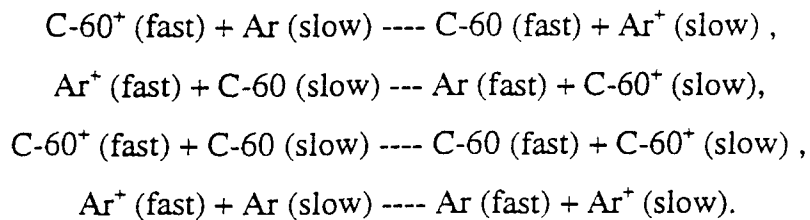
Since the first two collisions have much less collision cross sections than the last two and the charge exchange collision cross section for the third one is not available. Only the fourth one was considered in the simulation. This collision rate is determined by the number density of Ar and Ar^+ . Therefore, the simulation of the grid erosion was performed for argon at 10% of the total flow rate under the electric potential field from the previous simulation for C-60. All parameters used for the calculations are listed in Table 7. The calculated impingement current of the accelerator grid is 0.3 mA (Table 8). This is approximately 1.1% of beam current. The calculation was under an assumption that the downstream plasma density is 0.025% of the Ar density at the background pressure 8×10^{-6} Torr. The calculated mass loss of the molybdenum accelerator grid due to the erosion is 8.54×10^{-6} kg per 100 hours.

Table 7. Parameters for simulation of grid erosion

accel. grid hole dia.	2.0 mm
screen grid hole dia.	2.5 mm
grid hole pitch	3.0 mm
grid spacing	1.0 mm
thickness of accel. grid	0.5 mm
thickness of screen grid	0.5 mm
intergrid voltage	2000 V
diameter of thruster	0.13 m
propellant utilization	0.8
discharge voltage	30 V
ion temperature	1000 K
electron temperature	1.5 eV
tank pressure	8×10^{-6} Torr
propellant	Ar

Table 8. Simulated results for grid erosion by using parameters listed in the Table 7.

beam current	26.5 mA
accel. impingement current	0.3 mA
half divergence angle	7.5 °
erosion	8.54 mg/100hrs
perveance per hole	1.2×10^{-10} A/V$^{3/2}$

III. Conclusions

From the ion optics point of view, the geometries of configurations 2 and 3 are more favorable than that of configuration 1. Because of the high background pressure (8×10^{-5} Torr), configuration 3 with less intergrid spacing might experience intragrid arcing. Therefore, the configuration 2 was selected for further grid erosion study. The reason to chose an intergrid voltage with 2000 V is also the result of the high background pressure concern or intragrid arcing concern. The actual maximum total voltage without the

intragrid arcing under the background pressure at 8×10^{-5} can only be found out during the practical thruster operations.

Finally, more simulations are required to provide a better definition of optimum ion optics configuration for thrusters operated with C-60 and Ar mixture propellant.

References:

[1] Peng, X., Ruyten, W. M., and Keefer, D. '' Plasma Particle Simulation of Electrostatic Ion Thruster,'' *AIAA Journal of Propulsion and Power*, Vol. 6, No. 6, March/April 1992, pp. 361-366; formerly presented as AIAA paper 90-2647, July, 1990.

[2] Peng, X., Ruyten, W. M., Keefer, D. '' Particle Simulation of Grid Erosion in Ion Thruster with Hexagonally Symmetric Grids,'' submitted to *AIAA Journal of Propulsion and Power*, October, 1993.

[3] Zhang, Q., Peng, X., and Keefer, D. '' Particle simulation of Three-Grid Ion Optics,'' IEPC paper 93-178, 23rd AIAA International Electric Propulsion Conference, Seattle, Washington, September 13-16, 1993.

Configuration:	#1
Screen grid potential:	1000 V
Accel. grid potential:	-500 V
Upstream plasma density:	4.0×10^{17} m^{-3}
Beam current:	106 mA

potential contours (Volt)

	200
-200	400
-50	600
-1	800
0	1000
2	1010
5	1020
100	

Figure 1a. The potential contour and beam ions for the grid configuration 1 at the intergrid voltage 1500V.

Configuration: #2
Screen grid potential: 1000 V
Accel. grid potential: -500 V
Upstream plasma density: 4.0×10^{17} m^{-3}
Beam current: 178 mA

potential contours (Volt)

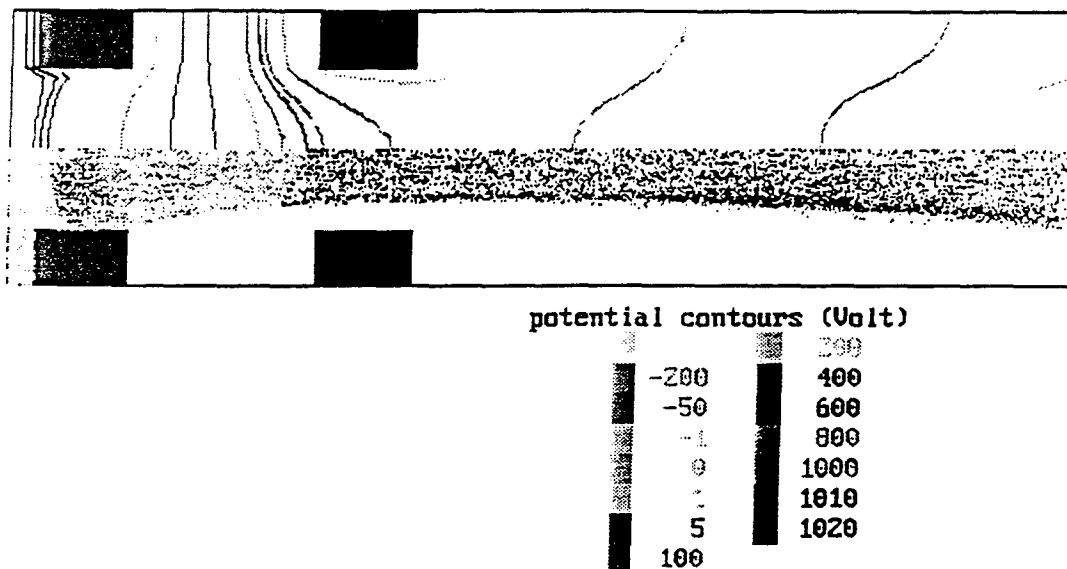|	
-400	200
-200	400
-50	600
-1	800
0	1000
1	1100
5	1200
100	

Figure 1b. The potential contour and beam ions for the grid configuration 2 at the intergrid voltage 1500V.

Configuration: #3
Screen grid potential: 1000 V
Accel. grid potential: -500 V
Upstream plasma density: 4.0×10^{17} m^{-3}
Beam current: 196 mA

potential contours (Volt)

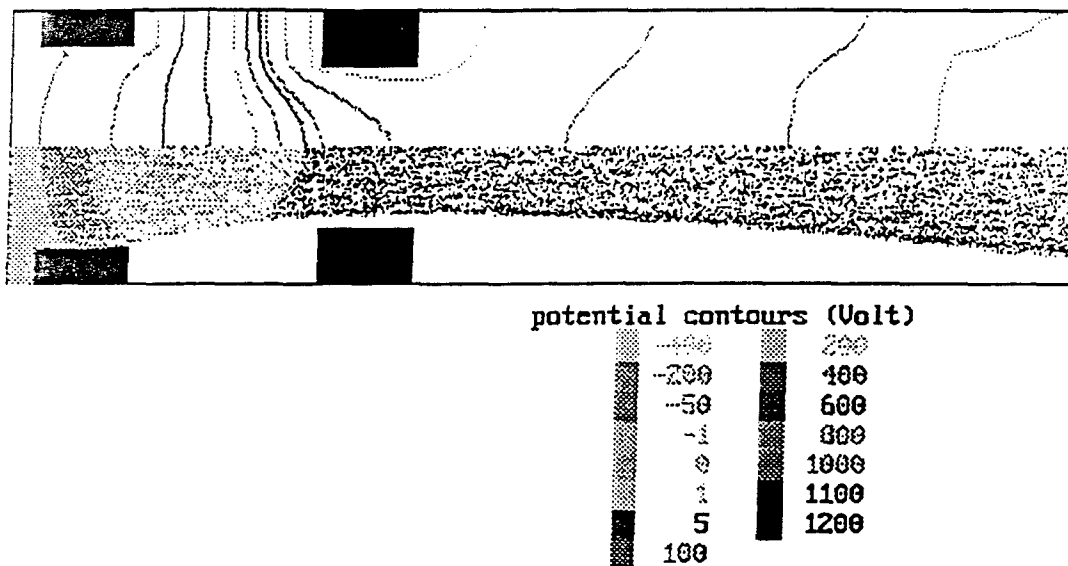|			
			200
	-200		400
	-50		600
	-1		800
	0		1000
	1		1010
	5		1020
	100		

Figure 1c. The potential contour and beam ions for the grid configuration 3 at the intergrid voltage 1500V.

Configuration: #1
Screen grid potential: 1500 V
Accel. grid potential: -500 V
Upstream plasma density: $6.0 \times 10^{17} \ m^{-3}$
Beam current: 147 mA

potential contours (Volt)

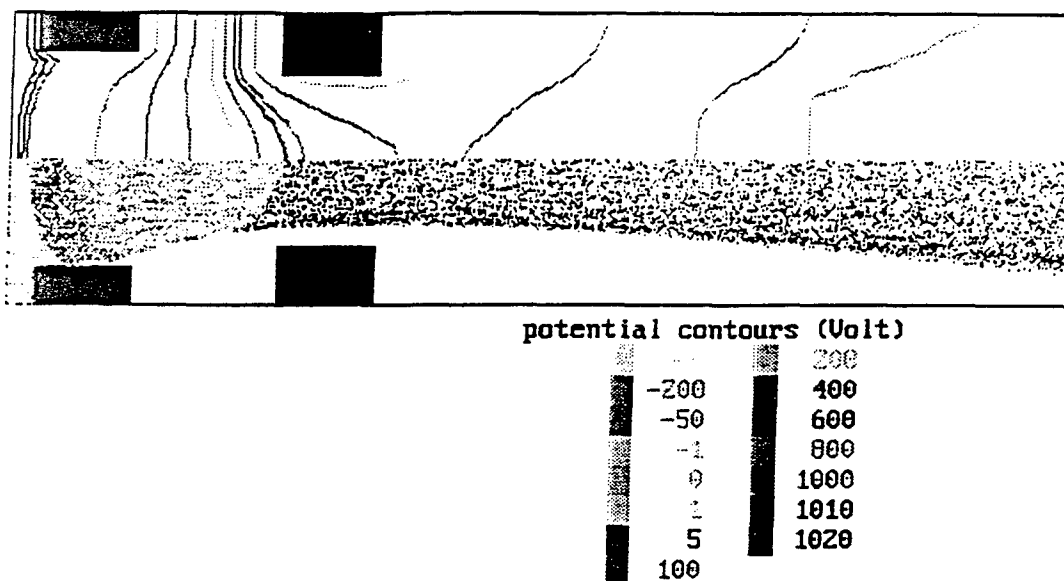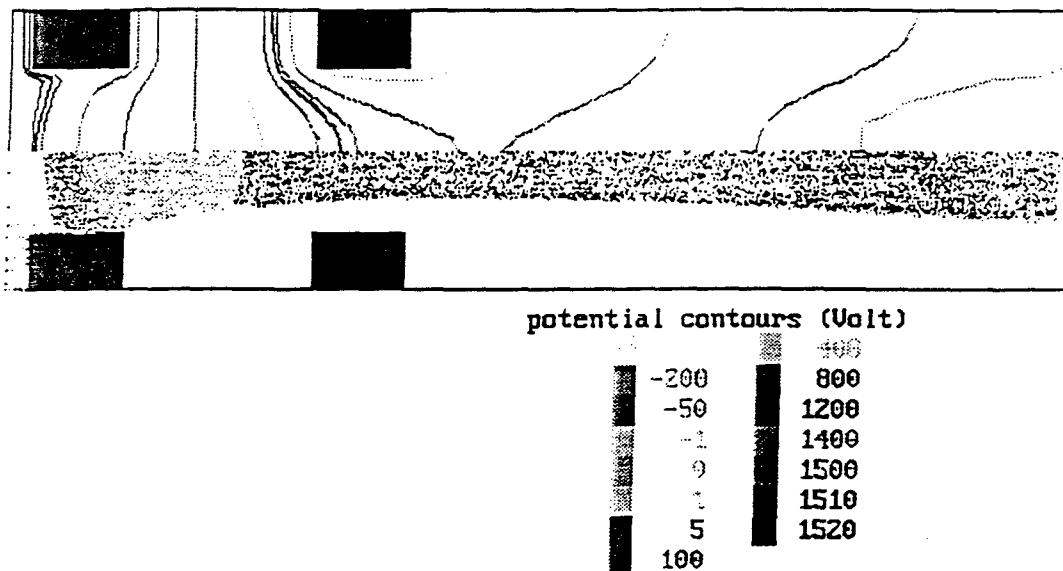|	
	400
-200	800
-50	1200
-1	1400
0	1500
1	1510
5	1520
100	

Figure 2a. The potential contour and beam ions for the grid configuration 1 at the intergrid voltage 2000V.

Configuration: #2
Screen grid potential: 1500 V
Accel. grid potential: -500 V
Upstream plasma density: 6.0×10^{17} m^{-3}
Beam current: 260 mA

potential contours (Volt)

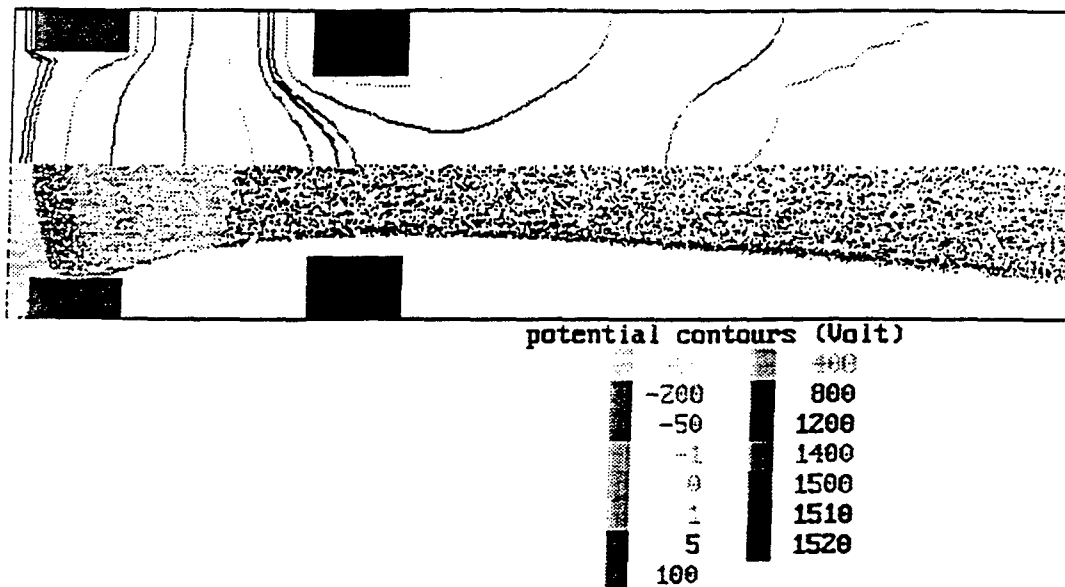|	
	400
-200	800
-50	1200
-1	1400
0	1500
1	1510
5	1520
100	

Figure 2b. The potential contour and beam ions for the grid configuration 2 at the intergrid voltage 2000V.

Configuration: #3
Screen grid potential: 1500 V
Accel. grid potential: -500 V
Upstream plasma density: 6.0×10^{17} m^{-3}
Beam current: 296 mA

potential contours (Volt)

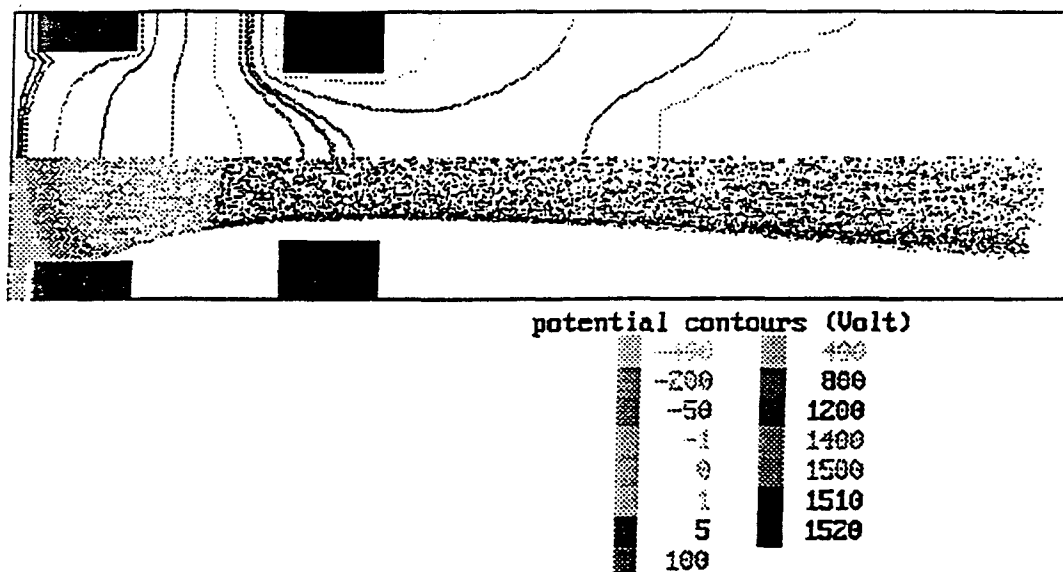|			
	-400		400
	-200		800
	-50		1200
	-1		1400
	0		1500
	1		1510
	5		1520
	100		

Figure 2c. The potential contour and beam ions for the grid configuration 3 at the intergrid voltage 2000V.

Configuration: #1
Screen grid potential: 2500 V
Accel. grid potential: -500 V
Upstream plasma density: 1.0×10^{18} m^{-3}
Beam current: 274 mA

potential contours (Volt)

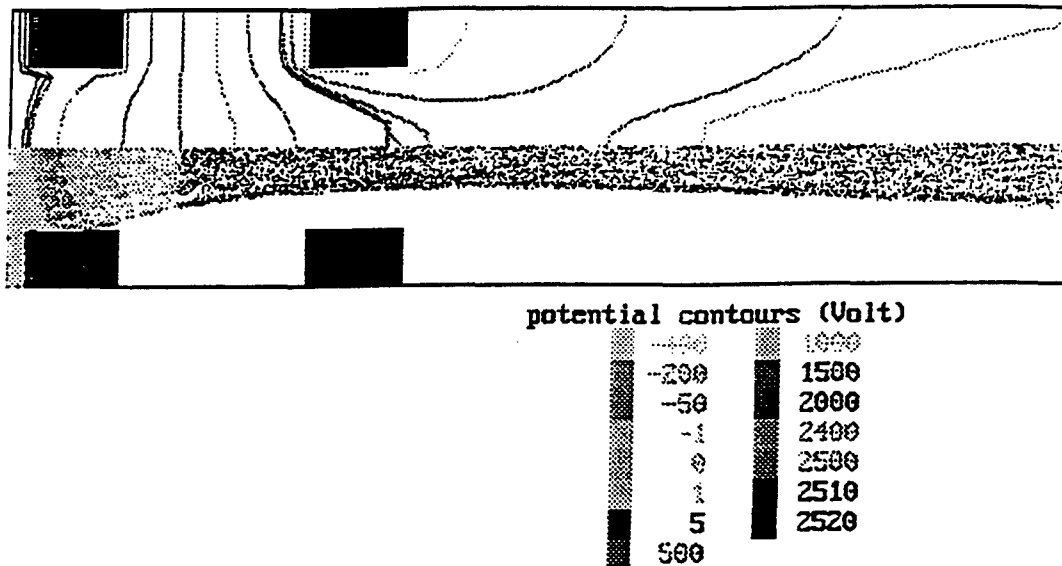|	
-400	1000
-200	1500
-50	2000
-1	2400
0	2500
1	2510
5	2520
500	

Figure 3a. The potential contour and beam ions for the grid configuration 1 at the intergrid voltage 3000V.

Configuration: #2
Screen grid potential: 2500 V
Accel. grid potential: -500 V
Upstream plasma density: 1.0×10^{18} m^{-3}
Beam current: 471 mA

potential contours (Volt)

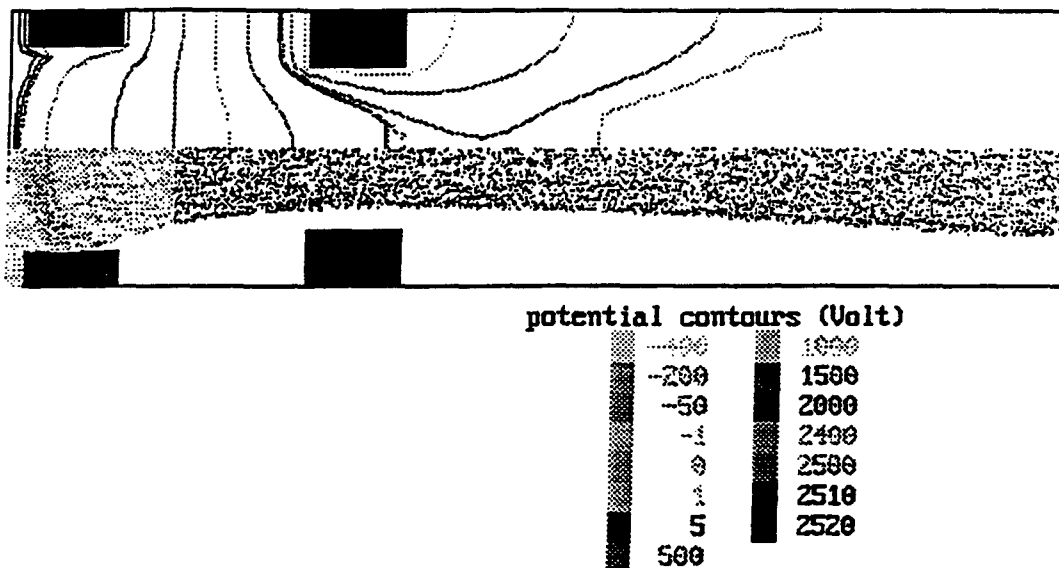|	
-400	1000
-200	1500
-50	2000
-1	2400
0	2500
1	2510
5	2520
500	

Figure 3b. The potential contour and beam ions for the grid configuration 2 at the intergrid voltage 3000V.

Configuration: #3
Screen grid potential: 2500 V
Accel. grid potential: -500 V
Upstream plasma density: 1.0×10^{18} m^{-3}
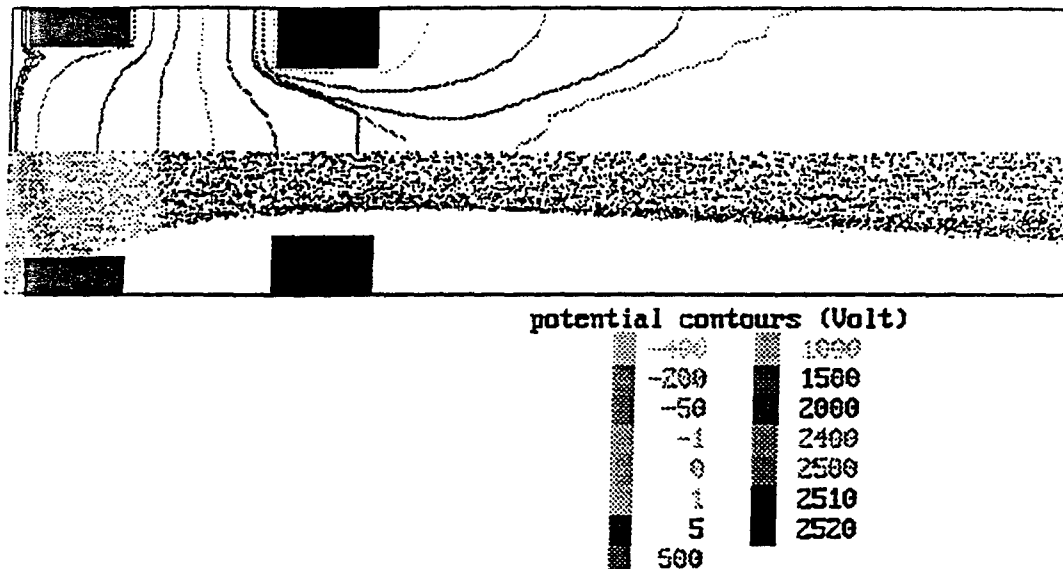Beam current: 502 mA

Figure 3c. The potential contour and beam ions for the grid configuration 3 at the intergrid voltage 3000V.

APPENDIX B

SPREAD SHEET ANALYSIS

SIZING AND PERFORMANCE ESTIMATES FOR THE FULLERENE ION THRUSTER

The equations for spread sheet analysis of the FIT engine are shown in Table B.1. The fullerene vapor temperature in the discharge chamber (Tn in Row #20) is manually iterated until the ratio in Row #45 becomes approximately 1. During experiments the discharge chamber temperature must be kept above Tn to avoid condensation. The proper vaporizer temperature (Tv in Row #59) is obtained by iteratively guessing its value until the ratio in Row #63 becomes approximately 1. This means that the required C_{60} mass flow calculated in Row #52 is delivered by the vaporizer (Row #62).

BUSEK

	A	B
4	CONSTANTS	
5	eps0(C2/Nm2) vac. permitivity	0.0000000000088544
6	go(m/sec2) gravity	9.81
7	qe(C) elementary charge	1.6021E-19
8	atomic unit mass amu (kg)	1.6604E-27
9	k(J/degK) Boltzman constant	1.38E-23
10		
11	INPUT/CASE NO	1
12	Dact.(m) grid active dia	0.13
13	ds(m) screen grid hole dia.	0.002
14	da(m) acc. grid hole dia.	0.002
15	p(m) grid hole pitch	0.003
16	lg(m) grid spacing	0.002
17	Vt(Volt) total inter. grid voltage	1000
18	Vn(volts) net voltage=mi*c^2/e	500
19	eatu(-) propellant utilization	0.8
20	Tn (k) guess at dis. cham. Tvapr-ITERATE	662
21	epsbi(volts) loss per beam ion	500
22	Vdis.(Volts) guess discharge voltage	30
23	etabase(-), base eff.	0.8
24	Mw(kg/kgmol) propellt mol. wt.	720
25	dstar vap(mm) vaporizer orifice dia.	5.8
26	Mwcathode(kg/kgmole) c. gas mole weight	39.9
27	fcn=(n of Ar)/(n of C60) cathode flow fract.	2.05
28	(vary fcn to get at most 3sccm cathode flow)	
29	OUTPUT - THRUSTER	
30	fo(-) open area fraction	=(3.14*B14^2)/(4*B15^2)
31	Aat(m2) surface area of grid	=3.14*B12^2/4
32	Aao(m2) open area of acc. grid	=B30*B31
33	N (-)numbr of holes	=4*B32/(3.14*B14^2)
34	mi(kg) mass of prop. ion	=B24*$B$8
35	ci(m/sec) ion exit speed	=SQRT(2*$B$7*B18/B34)
36	le(m) effective grid spacing	=(B16^2+0.25*B13^2)^0.5
37	J(A/m2) beam current density	=0.62854*$B$5*SQRT($B$7/B34)*B17^1.5/B36^2
38	Ibeam (A) beam current	=B37*B32
39	ni(1/m3) ion number density	=B37/($B$7*B35)
40	cn(m/sec) speed of neutrals	=SQRT(2*$B$9*B20/B34)
41	ni/nn(-)	=(B40/B35)*B19/(1-B19)
42	nn(1/m3) neutral number density	=B39/B41
43	ntot(1/m3) tot number density	=B42+B39
44	ntot(1/m3) based on Tdis. chamb. input	=(5368000000/$B$9)*(1/B20)*EXP(-38000/((8.314/4.186)*B20))
45	ntot(=R42)/ntot(=R43)iteterate to =1	=B43/B44
46	Tdis. cavity (degC) based ntot	=B20-273
47	p(N/m2) in dis. cavity based on ntot	=B43*$B$9*B20
48	p(Torr) in dis. cavity based on ntot	=0.007451*B47
49	F(N) thrust from eq.4	=B39*B34*B35^2*B32*(1-B40/B35+B40/(B35*B19))
50	F(grams)) thrust from eq.4	=B49*1000/9.81
51	mdot(kg/sec) mass flow eq.5	=B39*B34*B35*B32/B19
52	mdot(mg/sec) mass flow eq.5	=B51*1000000
53	Isp(sec) specific impls	=B49/(B51*9.81)
54	etat(-) thrust efficiency	=B23/(1+2*$B$7*B21/(B34*B35^2))
55	Pttl=F^2/(2*mdot*eta)	=B49^2/(2*B51*B54)
56	Pdis=Pttl-Pbeam=Pttl-Ibeam*Vnet	=B55-B38*B18
57	Idis.(amps)=Pdis/Vdis	=B56/B22
58	OUTPUT - VAPORIZER	
59	guess Tv(degC)	651
60	Pc60(mTorr)	=40000000000*EXP(-38000/((8.314/4.186)*(B59+273)))
61	Pc60(N/m2)	=B60/0.007451/1000
62	mdot c60 (mg/sec)	=1000000*B61*((3.14*(B25/1000)^2)/4)*SQRT(B24/(2*3.14*8314*(B59+273)))
63	mdot/mdot(from row#52)	=B62/B52
64	(iterate Tv to get Mdot/mdot=1)	
65	OUTPUT - cathode max flow	
66	Nc.gas(1/m3) cathode gas number densty	=B27*B43
67	cc(m/sec) thermal speed of cathode gas	=SQRT(2*$B$9*B20/(B26*$B$8))
68	mdot.cgas(mg/sec)	=1000000*B66*B26*$B$8*B67*B32
69	Vdot cgas(sccm) (keep at min.=about 2sccm)	=60*B68/(102000*B26/(8314*293))
70	mass fration (mdot_cgas/mdotC60)	=B68/B52

REFERENCES

1. H.W. Kroto, "C_{60}, Fullerenes, Giant Fullerenes, and Soot," Pure Appl. Chem., 62(3), 407-18 (1990).

2. S.D. Leifer and W. Saunders, "Electrostatic Propulsion Using C_{60} Molecules," IPEC-91-154, 22nd International Electrric Propulsion Conference, October 1992.

3. J.R. Anderson and D. Fitzgerald, "Experimental Investigation of Fullerene Propellant for Ion Propulsion," IEPC-93-033, 23rd International Electric Propulsion Conference, SEattle, September 1993.

4. S.D. Leifer, et al., "Developments in Fullerene Ion Propulsion Research," AIAA-94-3241, 30th Joint Propulsion Conference, Indianapolis, June 1994.

5. S.D. Leifer, et al., "Effect of the Thermal Stability and Reactivity of Fullerenes on Ion Engine Propellant Applications," AIAA 94-2467, 25th Plasmadynamics and Lasers Conference, Colorado Springs, June 1994.

6. J.R. Anderson, et al., "Design and Testing of a Fullerene RF Ion Engine," AIAA-95-2664, 31st Joint Propulsion Conference, San Diego, July 1995.

7. J. R. Anderson and D. Fitzgerald, "Fullerene Propellant Research for Electric Propulsion," AIAA 96-3211, 32nd Joint Propulsion Conference, Lake Buena Vista, July 1996.

8. H. Takegahara and Y. Nakayama, "C_{60} Molecule as a Propellant for Electric Propulsion," IEPC-93-032, 23rd International Electric Propulsion Conference, September 1993.

9. Y. Nakayama and H. Takegahara, "Fundamental Experiments of C60 Application to Ion Thruster," IEPC-95-88, 24th International Electric Propulsion Conference, September 1995.

10. H. Takegahara and Y. Nakayama, "C_{60} Feasibility Study on Application to Ion Thruster — Preliminary Experiments Using Electron Bombardment Thruster," AIAA 95-2665, 31st Joint Propulsion Conference, San Diego, July 1995.

11. Y. Nakayama, N. Endo and H. Takegahara, "Study on C_{60} Application to Ion Thruster — Evaluation of Ion Production," 32nd Joint Propulsion Conference, Lake Buena Vista July 1996.

12. E.R. Torres, "Prediction of the Performance of an Ion Thruster Using Buckminsterfullerene as the Propellant," Master of Science Thesis, MIT, February 1993.

13. V. Hruby, et al., "A High Thrust Density, C_{60} Cluster, Ioon Thruster," AIAA 94-2466, 25th Plasmadynamics and Lasers Conference, Colorado Springs, June 1994.

14. V. Hruby, et al., "Fullerene Fueled Electrostatic Thrusters — Feasibility and Initial Experiments," AIAA 94-3240, 30th Joint Propulsion Conference, Indianapolis, June 1994.

BUSEK

15. Busek Co. Inc., "A High Thrust Density, C_{60} Cluster, Ion Thruster," Final Report, Phase I SBIR, prepared for AFOSR, Contract No. F49620-92-C-0039, February 1993.

16. "Emission Properties of Materials," Translation of Russian-language book by V.S. Fomenko: Emissionnyye Svoystva Materialov, 1970, thrid revised and supplemented edition, signed to press 2 November 1970, Naukova Dumka Publishing House, Kiev, 146 pages, UDC 537.533.2.

17. X. Peng, W.M. Ruyten and D. Keefer, "Particle Simulation of Grid Erosion in Ion Thruster with Hexagonally Symmetric Grids," AIAA Journal of Propulsion and Power, October 1993.

18. D. Lorents, SRI International, Personal Communications, July 21, 1994.

19. J. Li, et al., "Photopolymerized Skins of C_{60} Crystals," Chemical Physics Letters 227 (1994) 572-578.

20. J.S. Sovey, "Improved Ion Containment Using a Ring-Cusp Ion Thruster," J. Spacecraft, Vol. 21, No. 5, 1983.

21. J.N. Matossian and J.R. Beattie, "Characteristics of Ring-Cusp Discharge Chambers," J. Propulsion, Vol. 7, No. 6, 1990.

22. D.C. Rovang and P.J. Wilbur, "Ion Extraction Capabilities of Two-Grid Accelerator Systems," J. Propulsion, Vol. 1, No. 3, 1985.

23. D.M. Gruen, et al., "Fullerenes as Precursors for Diamond Film Growth Without Hydrogen or Oxygen Additions," Appl. Phys. Lett. 64 (12), March 1994.

24. D. Rapp and P. Englander-Golden, "Total Cross Sections for Ionization and Attachment in Gases by Electron Impact," The Journal of Chemical Physics, 43 (5), September 1965.

25. M. Sai Baba, et al., "Appearance Potential and Electron Impact Ionsation Cross-Section of C_{60}," International Journal of Mass Spectrometry and Ion Processes, 114 (1992) R1-R8, Elsevier Science Publishers.

26. E.B. Maiken and P. Taborek, "IonBeam Deposition of Hard, Amorphous Carbon from a Fullerene Discharge," J. Appl. Phys. 78 (1), July 1995.

27. Busek Co. Inc., "A Fullerene Hall Thruster Development," Phase I Final Report, Contract No. NAS3-26712, prepared for Strategic Defense Initiative Organization, March 1993.

BUSEK